9-2009

Wrinkling, Folding, and Snapping Instabilities in Polymer Films

Douglas Peter Holmes
University of Massachusetts Amherst, dpholmes@gmail.com

WRINKLING, FOLDING, AND SNAPPING INSTABILITIES IN POLYMER FILMS

A Dissertation Presented

by

DOUGLAS PETER HOLMES

Submitted to the Graduate School of the
University of Massachusetts Amherst in partial fulfillment
of the requirements for the degree of

DOCTOR OF PHILOSOPHY

September 2009

Polymer Science & Engineering

WRINKLING, FOLDING, AND SNAPPING INSTABILITIES IN POLYMER FILMS

A Dissertation Presented

by

DOUGLAS PETER HOLMES

Approved as to style and content by:

Alfred J. Crosby, Chair

Thomas J. McCarthy, Member

Narayanan Menon, Member

Shaw Ling Hsu, Department Chair
Polymer Science & Engineering

To my wife.

ACKNOWLEDGEMENTS

First and foremost, I would like to thank my thesis advisor Professor Al Crosby for mentoring me throughout my graduate career. In the confusion of starting graduate school I found myself drawn to Al's strong character and love for science. Joining his group was the best decision I could have made for my graduate career. He has proved to be a brilliant and dedicated mentor throughout each stage of my graduate studies. I've learned so many valuable lessons about how to approach science experimentally and analytically; his mentorship has made me into the scientist I am today. Al has also been a model of how to balance work and family and I will always be grateful for that. I hope the completion of my doctoral studies with Al is just the beginning of a great friendship, both personally and scientifically.

I am also indebted to my thesis committee members, Professor Thomas McCarthy and Professor Narayanan Menon. During my first year classes, I remember looking forward to the days when Tom would break from the script to wax poetic on a seemingly unrelated, yet deeply scientific, topic. His presence on my committee has forced me to think about science in a variety of conventional and unconventional ways, and for that I am grateful. Menon was also an essential part of my graduate education. His approach to problem-solving is entirely different from mine - he focuses on the importance of fundamentals - and that stylistic contrast is quite possibly the best attribute you can ask for in a committee member. I have learned a great deal from both Tom and Menon over the years and I admire their devotion and enthusiasm as scientists.

I want to thank all of the Crosby group members I have worked with over the past five years for making my time here engaging and enjoyable. Specifically, I want to

thank Edwin Chan for shaping the way I experimented in lab and answering my many questions. I'm also grateful to the group for countless hours of practice-talk advice and rough drafts edited, specifically by Jong-Young Lee, Charles Rand, Jessica Zimberlin, Derek Breid, Chelsea Davis, Santanu Kundu, and Guillaume Miquela. Most recently, I want to thank Andrew Croll for allowing me to bounce ideas off him and work through derivations that would have previously left me stumped. I have been very fortunate to work with several great REU's and RET's over the years. Special thanks go to Michal Ursiny and Andrew Davis for being my hands in lab and helping to develop the crumpling and delamination folding projects. I also want to thank Sabra Dickson for reminding me how much impact one teacher can have on each student that sits in their classroom.

It is difficult to acknowledge all the people who made this possible without mention of my friends near and far who have helped me through these past five years. I spent two years living in a rural farmhouse with fellow graduate students and great friends, Scott Eastman and Ryan Murphy. Ryan was later the officiant at my wedding and the person who kept me grounded in science, music, sports, and life. Mark Hixon and Nathan Hobbs have long been a large part of my life outside the lab and I am lucky to have such loyal friends. There is no way to properly acknowledge my best friend, Dan Maynard, for the many late nights we spent playing music, and discussing science, politics, and philosophy. Dan is a true lifelong friend.

My family, both old and new, has provided me with all the love and support I could ever imagine, and for that I am forever indebted to them. I want to thank my parents, Douglas and Sharon, for making my family the part of my life I'm most proud of. As my dad has always said, "You can't learn that in a book." Thanks also to my brother Stephen, and my sister Melissa, who have always been there for me and always will be. Also, I want to thank my new family- David, Lorraine, Brendan,

and Kevin Gelardi - who have welcomed me into their family with open arms and endless support and encouragement.

Lastly, they say behind every great man is a great woman. I cannot claim to be the former, but my wife Meghan is certainly the latter. I can honestly say that I would not be writing this thesis had she not been by my side each step of the way. I have dedicated this thesis to her because I know she'll always be on my team.

The scientist does not study nature because it is useful;
he studies it because he delights in it, and he delights in it because it is beautiful.
If nature were not beautiful, it would not be worth knowing,
and if nature were not worth knowing, life would not be worth living.

-Jules Henri Poincaré

ABSTRACT

WRINKLING, FOLDING, AND SNAPPING INSTABILITIES IN POLYMER FILMS

SEPTEMBER 2009

DOUGLAS PETER HOLMES

B.Sc., UNIVERSITY OF NEW HAMPSHIRE

M.Sc., UNIVERSITY OF MASSACHUSETTS AMHERST

Ph.D., UNIVERSITY OF MASSACHUSETTS AMHERST

Directed by: Professor Alfred J. Crosby

This work focuses on understanding deformation mechanisms and responsiveness associated with the wrinkling, folding, and snapping of thin polymer films. We demonstrated the use of elastic instabilities in confined regimes, such as the crumpling and snapping of surface attached sheets. We gained fundatmental insight into a thin film's ability to localize strain. By taking advantage of geometric strain localization we were able to develop new strategies for responsive surfaces that will have a broad impact on adhesive, optical, and patterning applications.

Using the rapid closure of the Venus flytrap's leaflets as dictated by the onset of a snap instability as motivation, we created surfaces with patterned structures to transition through a snap instability at a prescribed stress state. This mechanism causes surface topography to change over large lateral length scales and very short timescales. Changes in the stress state can be related to triggers such as chemical

swelling, light-induced architecture transitions, mechanical pressure, or voltage. The primary advantages of the snap transition are that the magnitude of change, the rate of change, and the sensitivity to change can be dictated by a balance of materials properties and geometry. The patterned structures that exhibit these dynamics are elastomeric shells that geometrically localize strain and can snap between concave and convex curvatures. We have demonstrated the control of the microlens shell geometry and that the transition time follows scaling relationships presented for the Venus flytrap. Furthermore, the microlens arrays have been demonstrated as surfaces that can alter wettability.

Using a similar novel processing technique, microarrays of freestanding elastomeric plates were placed in equibiaxial compression to fabricate crumpled morphologies with strain localized regions that are difficult to attain through traditional patterning techniques. The microstructures that form can be initially described using classical plate buckling theory for circular plates under an applied compressive strain. Upon the application of increasing compressive strain, axisymmetric microstructures undergo a secondary bifurcation into highly curved, nonaxisymmetric structures. The inherent interplay between geometry and strain in these systems provides a mechanism for generating responsiveness in the structures. By swelling the elastomeric plates with a compatible solvent, we demonstrated the microstructures ability to reversibly switch between axisymmetric and nonaxisymmetric geometries.

To further explore the localization of strain in materials, we have fabricated sharply folded films of glassy, homogenous polymers directly on rigid substrates. The films were uniaxially compressed and buckle after delaminating from the substrate. As the applied strain is increased, we observed strain localization at the center of the delaminated features. We found that normally brittle, polystyrene films can accommodate excessive compressive strains without fracture by undergoing these strain localizing fold events. This technique provided a unique way to examine the curvature

and stability of folded features, but was not adequate for understanding the onset of folding.

By taking thin films, either glassy or elastomeric, and simply lifting them from the surface of water, we observed and quantified the wrinkle-to-fold transition in an axisymmetric geometry. The films initially wrinkle as they are lifted with a wavelength that is determined by the film thickness and material properties. The wrinkle-to-fold transition is analogous to the transition observed in uniaxially compressed films, but the axisymmetric geometry caused the fold to act as a disclination that increased the radial stress in the film, thereby decreasing the wavelength of the remaining wrinkles. Further straining the films caused the remaining wrinkles to collapse into a discrete number of folds that is independent of film thickness and material properties.

TABLE OF CONTENTS

LIST OF TABLES

Table **Page**

LIST OF FIGURES

Figure **Page**

CHAPTER 1

INTRODUCTION

1.1 Project Overview

Elastic instabilities are commonly exhibited throughout everyday life across a wide variety of material systems. Wrinkles may form on the skin of a fruit or a human. A can of soda will buckle under a compressive load. The Venus flytrap will snap its wings shut to capture its prey. These examples are among many that are ubiquitous in nature. In general, an elastic instability occurs when multiple equilibrium states exist for a system, causing the system to select the most energetically favorable state. An important consequence of this, in general, is that the selection of the most favorable equilibrium state occurs almost instantly once this bifurcation point is reached. In the case of the Venus flytrap, the rapid closure of the plant's leaves ($\Delta t \approx 100ms$) is caused by the slow storage of elastic energy followed by its rapid release [1]. Plants are not known for their ability to move quickly, yet the snap-buckling elastic instability was one way nature devised to enable rapid plant movements [2].

Elastic instabilities, such as the snapping of the Venus flytrap's leaves, provide ample inspiration and design criteria for rapid, responsive synthetic systems. A responsive surface is one that can dynamically change its properties or shape in response to a specific trigger, or stimulus. It is easy to imagine the vast impact such surfaces would have on the development of dynamic devices. Possible applications include switchable adhesives [3–6], optical switches [7, 8], drug delivery [9–11], and chemical sensing [12–14]. Traditional synthetic avenues for creating responsive systems include shape-memory materials that exhibit a predetermined response to environ-

mental changes, which may alter the material's shape or properties [15, 16]. These systems offer a unique advantage in a material's ability to macroscopically respond to a variety of external stimuli, but the response time is typically on the order of several minutes to several hours. Alternatively, material systems involving surface functionalization provide a reversible system focused on tuning the interface for specific applications [17, 18]. These systems are tunable and adaptable, but a notable drawback is their inability to change global surface properties over a fast time scale. A general overview on responsive systems found synthetically and in nature can be found in Appendix A.

The primary motivation for this thesis is using the lessons from nature, such as the Venus flytrap, to create responsive surfaces and structures that change over a large length scale and small time scale. We have prepared an array of microstructures that exhibit a snap-buckling elastic instability to rapid change concavity on a surface. Using a similar technique we fabricated crumpled elastomeric plates with strain localized regions that have inherent responsiveness in their microstructures. To further explore the localization of strain we fabricated sharply folded films onto rigid substrates. We finally studied the instability that causes a fold to develop by observing the wrinkle-to-fold transition in thin, draping films. This thesis will examine the impact of strain localization within thin films on responsive elastic instabilities such as wrinkling, folding, and snapping.

1.2 Background

Before proceeding, it is important to elaborate on three general concepts that will be discussed throughout this thesis. First, what is elastic stability? Second, what is snap-buckling? Finally, what is strain localization, and how does it apply to the structures we will discuss in this work?

1.2.1 Elastic Stability

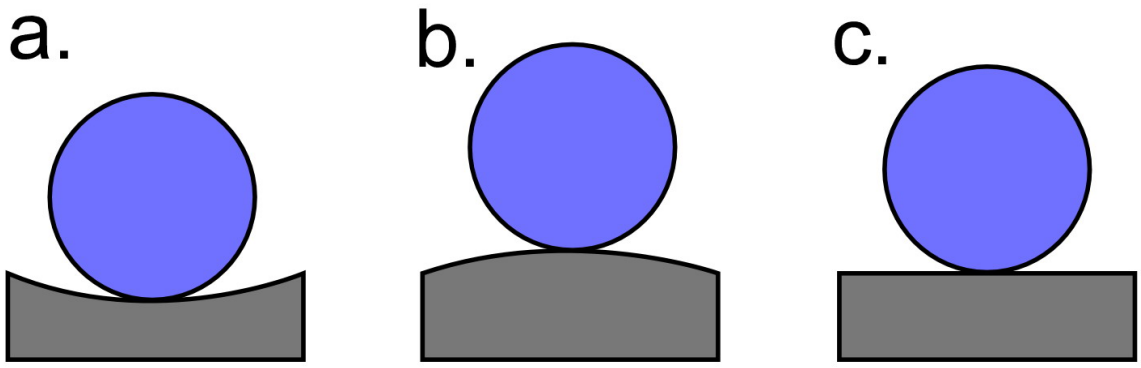

Figure 1.1: Equilibrium of a Rigid-Body System. A ball in three equilibrium positions: a. the ball resting on the concave surface is in a stable equilibrium because any lateral displacement will increase the energy of the system, b. the ball on the convex surface is unstable since a lateral displacement will lower the ball's center of gravity, thereby decreasing the system's potential energy, and c. the ball on the flat surface is in neutral equilibrium since lateral displacement will not impact the potential energy of the system.

The simplest way to address the question of stability is by considering the equilibrium configurations of rigid-body systems [19]. Let us consider the three equilibrium positions of ball shown in figure 1.1. It is clear from this illustration that the ball on the concave surface is in *stable equilibrium* (Figure 1.1a), the ball on the convex surface is in *unstable equilibrium* (Figure 1.1b), while the ball on the flat surface is in *neutral equilibrium* (Figure 1.1c). Physically, the equilibrium of each configuration can be determined by considering the energy of the system [19]. In the first case, any lateral displacement of the ball from its equilibrium position will raise its center of gravity. Such a displacement requires the addition of work, thereby increasing the potential energy of the system. For the ball resting on the convex surface, any displacement lowers the ball's center of gravity, causing a decrease in potential energy. Therefore, in a stable equilibrium the energy is at a minimum, while in an unstable equilibrium the energy is at a maximum. The ball resting on the flat surface is

in neutral equilibrium because lateral displacement has no impact on the system's potential energy.

In the case of beams or plates, a lateral deflection means an increase in the strain energy of the system, ΔU_B. In a similar manner, the load, P, will move through a small distance of the material and do work equal to ΔU_S. The beam or plate will remain stable and undeflected when:

$$\Delta U_B > \Delta U_S \tag{1.1}$$

and unstable when:

$$\Delta U_B < \Delta U_S \tag{1.2}$$

When a load, P, is applied to the top of the beam the bar becomes displaced by the small angle, α (Figure 1.2a). This displacement effectively lowers the load by the amount:

$$l(1 - \cos\alpha) \approx \frac{l\alpha}{2} \tag{1.3}$$

The decrease in the potential energy of the load is equivalent to the work done by P:

$$\Delta U_S = \frac{Pl\alpha^2}{2} \tag{1.4}$$

In a similar manner, the spring, with a spring constant β, must elongate by the amount αl to accommodate the load, thereby increasing the strain energy of the spring:

$$\Delta U_B = \frac{\beta(\alpha l)^2}{2} \tag{1.5}$$

From equations 1.1 and 1.2 we know that the beam will be stable when:

$$\frac{\beta(\alpha l)^2}{2} > \frac{Pl\alpha^2}{2} \tag{1.6}$$

and unstable when:

$$\frac{\beta(\alpha l)^2}{2} < \frac{Pl\alpha^2}{2} \tag{1.7}$$

Therefore, the critical load for when the equilibrium configuration changes from stable to unstable, as illustrated in figure 1.2b, occurs when [19]:

$$\Delta U_B = \Delta U_S \tag{1.8}$$

allowing us to calculate the critical load to buckle a beam:

$$P_c = \beta l \tag{1.9}$$

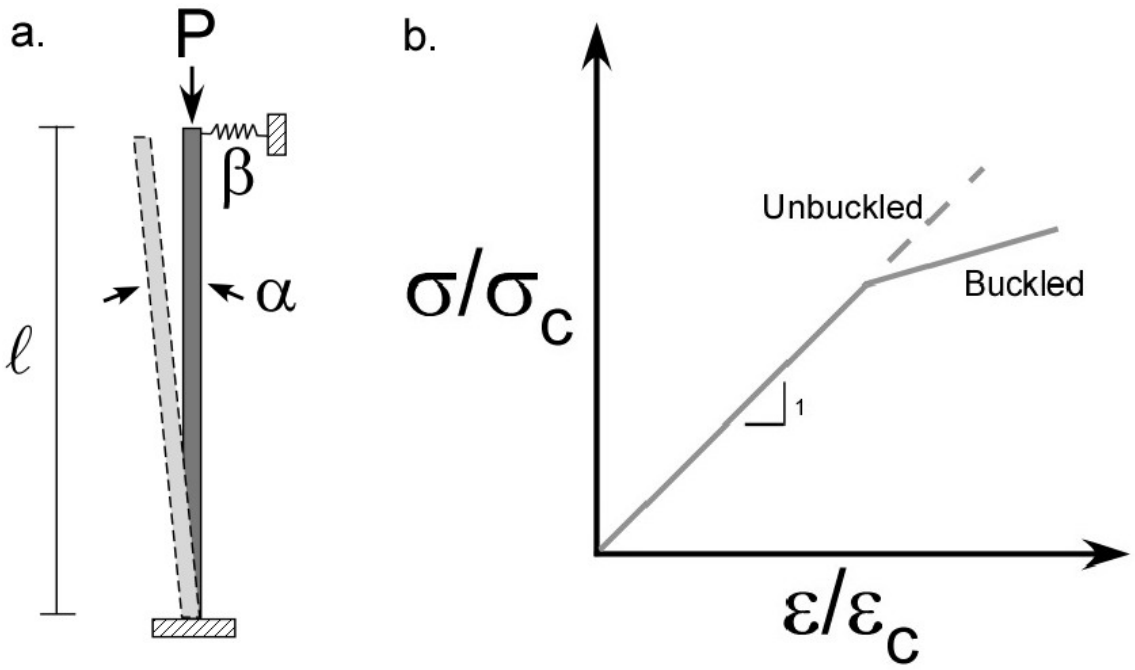

Figure 1.2: Euler Buckling Schematic. An illustration of the Euler buckling of beam under uniaxial loading along with the corresponding load vs. displacement curve for the buckled and unbuckled equilibrium states.

1.2.2 Stability of Nonlinear Shells

With a general understanding of elastic stability it is important to note that one of the most effective thin-walled structures in engineering is the geometrically nonlinear shell. The shell's ability to use lightweight design to create high-strength materials has led to its use in aerospace materials, chemical apparati, and building constructions [20]. The inherent nonlinear behavior of these shells under loading makes describing the deformation and stability of geometrically nonlinear shells very complex. Considering the shell to be a continuous system with an infinite number of degrees of freedom and two stable states allows stability loss to occur by snapping. Unlike the stability loss in a classical sense occuring by bifurcation (e.g. Euler Buckling) which is a loss of stability *in the small*, snap-buckling is a loss of stability *in the large* [20]. The distinction being in the case of snap-buckling the pre- and post-critical states are separated by a finite distance, while in Euler buckling the two states are infinitely close together. To understand the behavior of nonlinear shells we define the initial shape with a nondimensional, geometric parameter called the apex rise:

$$\bar{\xi} \equiv \frac{w}{h} \tag{1.10}$$

where w is the shell height at the center and h is the shell thickness. We can therefore describe the characteristic response curve for a shell with a clamped boundary loaded by a uniform pressure, q, for different initial shell geometries 1.3 [20]. Each load-displacement curve represents the equilibrium states of the cap at various loads, where ξ is displacement of the apex. From figure 1.3 it is clear that for a circular plate ($\bar{\xi} = 0$) there is only one state of equilibrium for each value of q. The equilibrium curves, or response curves, for spherical caps where $\bar{\xi} \geq 2$ are no longer monotonic and exhibit a maxima and minima. These shells therefore may exhibit a loss of stability via a snap-buckling process between two equilibrium states.

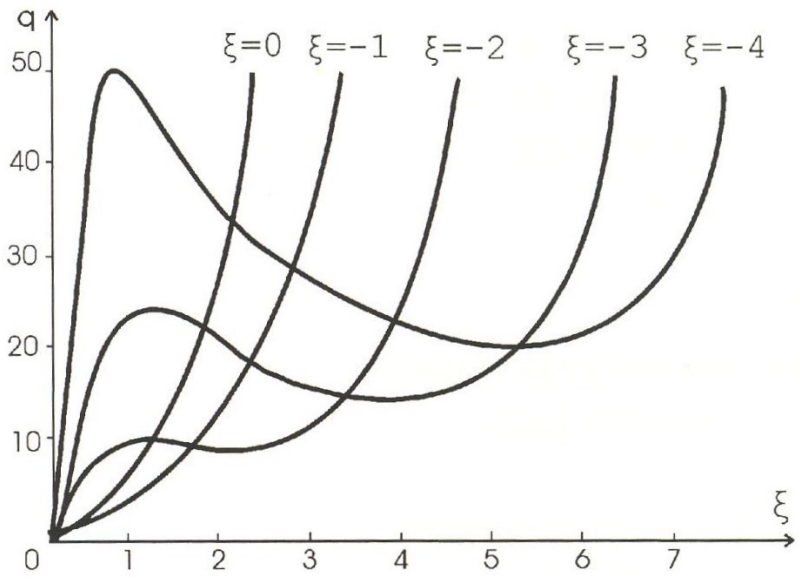

Figure 1.3: Characteristic Stability Curves for Nonlinear Shells. The axisymmetric response of a clamped spherical cap under uniform pressure q for different initial geometries that are described by the shell's height and thickness, $\bar{\xi} \equiv w/h$ (i.e. $\bar{\xi} = 0$ to $\bar{\xi} = 4$). There is only one state of equilibrium for values of $q > -2$, while two equilibrium states exist when $q \leq -2$. Figure reproduced from Shilkrut *et al.* [20].

The response curve for $\bar{\xi} = 2$ is given in figure 1.4. The transition from point A to point B is a snapping process due to the increasing load. Once in the second, stable equilibrium state, if the load is then decreased from point B to point C, the shell will snap-back (C to D) to its initial geometry. The load values at points A and C represent the upper and lower critical loads of the shell, respectively. This snapping phenomena cannot be fully understood from these equilibrium curves because it is a transient process which requires solving the corresponding nonlinear equations of motion to properly describe it. The most important conclusion regarding the characteristics of the nonlinear behavior of shells is the possibility of the existence of more than one equilibrium state for the same value of an external load [20]. While figures 1.3 and 1.4 illustrate only two distinct equilibrium states, the total number of states, n, increases for very deep spherical caps, such that [21]:

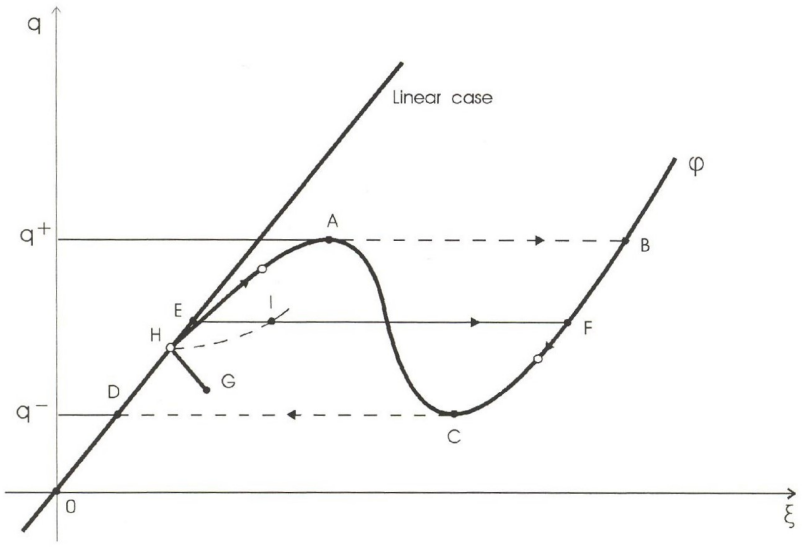

Figure 1.4: Nonlinear Shell Behavior. Various types of nonlinear behavior for a spherical cap under uniform pressure q. A shell loaded from the initial geometry at point D to point A will snap to point B at a critical load q^+. Similarly, decreasing the load from point B to point C will cause the shell to snap-back. Figure reproduced from Shilkrut *et al.* [20].

$$n \sim \left(\frac{q}{E}\right)^{1/2} \left(\frac{h}{R}\right)^{-3/2} \tag{1.11}$$

where E is the Young's elastic modulus, R is the radius of curvature, and A is depends on the form of the shell and on its Poisson's ratio ν.

1.2.3 Focusing & Localization

The concepts described in classical beam bending and buckling can be applied to a two-dimensional planar object. Imagine a thin sheet within a spherical container. Hydrostatically decreasing the volume of the spherical container will cause the sheet to deform, ultimately developing bends and sharp folds. These sharp structures are generally described as crumpling and represent a form of energy focusing [22]. The shrinking spherical container causes the initially smoothly distributed elastic energy of deformation to become more nonuniform and concentrated within strongly bent

regions. The thinner the initial sheet, the more pronounced the stress concentration and strongly bent regions become.

The spontaneous localization of energy impacts a wide array of physical problems. Considering the chaotic fluid motion commonly described as turbulence, it is understood that the kinetic energy injected uniformly into a fluid becomes progressively concentrated in regions of strong vorticity in space and strong intermittency in time [23]. Shock waves are caused by the focusing of strong vibrational excitations within a system [24]. Another common example is the strong mechanical response of solids under uniform perturbation causing a focused response leading to fracture [25]. The focusing and localization of energy that would normally distribute itself evenly in space is counterintuitive yet important to understand in order to utilize its benefits while minimizing its drawbacks.

In a general sense, systems with multiple stable symmetries may respond to a homogeneous energy input by spontaneously localizing this energy into small regions [26, 27]. The areas of localization have no characteristic length scale, and may increase in size or number as more energy is added to the system. If we consider the total strain energy per volume of a system to be:

$$\frac{U_V}{V} = \frac{\int_V \sigma d\varepsilon}{V} \tag{1.12}$$

then we can describe a localization event as one where the strain energy in a volumetric segment, V' is greater than the strain energy of the total system volume:

$$\frac{U_V}{V} \ll \frac{\int_{V'} \sigma d\varepsilon}{V'} \tag{1.13}$$

Focusing on the mechanical response of beams and plates, the Euler buckling instability described in the previous section provides information about the initial stages of a focused, crumpled structure, but does not describe focusing. Subsequent

work with the Föppl-von Karman equations cannot describe nonlinear coupling events that can lead to localized buckling events within a sheet. These regions of localized buckling describe a focusing of energy from the entire sheet into a small region and describe a form of stress focusing that represents a precursor to sharply focused events. The ability for a thin sheet or membrane to form stretching ridges and developable cones (d-cones) in response to confinement allows the formation of sharply focused features. The interaction of these structural elements, although presently still not well understood, interact to form crumpled sheets.

1.3 Thesis Organization

In Chapter 2, we will build on lessons from the closure of the Venus flytrap's leaves and the snap-through of a spherical shell to develop a simple, robust, biomimetic responsive surface. The surface will consist of an array of shell microstructures that can deform or change concavity in response to an external trigger. These microstructures exhibit a snap-buckling elastic instability that is similar to the mechanism for leaf closure of the Venus flytrap. Using the design principles from nature and shell mechanics, we will investigate and develop a surface of tunable microstructures that can rapidly snap between two topographies in response to external stimuli. The use of elastic instabilities to control surface properties creates a novel design paradigm for the generation of responsive surfaces.

In Chapter 3, we will focus on the localization of strain that occurs in the spherical microstructures introduced in Chapter 2. We will present a simple patterning method to generate a variety of tunable surface topographies that would be difficult to achieve using current fabrication techniques. We will use classical plate mechanics and shell theory to explain the formation, buckling, and post-buckling response of the microstructures. We will use strain to dictate the microstructure's shape which allows us to explore their ability to dynamically and reversibly change shape. This

surface patterning strategy will bring a greater understanding to the ability for a shell to localize strain, while also offering a novel approach for the fabrication of the next generation of surface patterns, especially in the context of responsive materials.

In Chapter 4, we will continue to explore the existence of strain localizations within polymer films. By simplifying the geometry away from circular plates under biaxial compression to films under uniaxial compression we will better understand the localization of strain. Our focus will be on the delamination and subsequent folding of ultrathin, brittle polymer films. We will present sharply folded nanostructures with widths on the order of nanometers and lengths on the order of millimeters. The folding of ultrathin films in confined geometries will provide insight into the material's properties, as well as insight into controlling the next generation of nanoscale feature morphology and structure.

In Chapter 5, we will build on our understanding from Chapter 4 on the localizations that can form within thin polymer films and focus on understanding the wrinkle-to-fold transition in films. The wrinkle-to-fold transition of films under axisymmetric conditions is commonly observed in nature from cell morphology to the ciliary body of the eye [28]. We will explore this transition by simply lifting a thin film from the surface of water. We will look to explain the formation of wrinkles with a characteristic wavelength, and explore the displacement at which these wrinkles collapse to folds. We will also illustrate how fold formation in an axisymmetric geometry impacts the stress on the remaining regions of the film. Understanding the linear and nonlinear behavior of thin films confined to soft or fluid substrates provides critical insight towards their use in biological and synthetic soft material enviroments.

CHAPTER 2

SNAPPING SURFACES

2.1 Introduction

The responsive mechanism of the Venus flytrap has captured the interest of scientists for centuries. Although a complete understanding of the mechanism controlling the Venus flytrap movement has yet to be determined, a recent publication by Forterre et al. [1] demonstrates the importance of geometry and material properties for this fast, stimuli-responsive movement. Specifically, the movement is attributed to a snap-through elastic instability whose sensitivity is dictated by the length scale, geometry, and materials properties of the features [2] (Figure 2.1a). In this chapter, we will focus on using lessons from the Venus flytrap to design a responsive surface (Figure 2.1b). This work will focus on four key questions. First, can we develop a simple fabrication technique to prepare surfaces with topographic features that rapidly change morphology? Second, can we predict and control the shape of the features? Third, how can we generate a snap-through instability in the structures that responds with a tunable time scale? Finally, can we demonstrate the structure's responsive ability for property control?

2.2 Experimental Approach

To fabricate the active surface structures, we use the Euler buckling of plates to generate a controlled array of microlens shells under equibiaxial compressive stress (Figure 2.2). First, we pattern cylindrical posts of photoresist onto a silicon wafer and micromold poly(dimethylsiloxane) (PDMS) (Sylgard 184^{TM}) elastomer onto it,

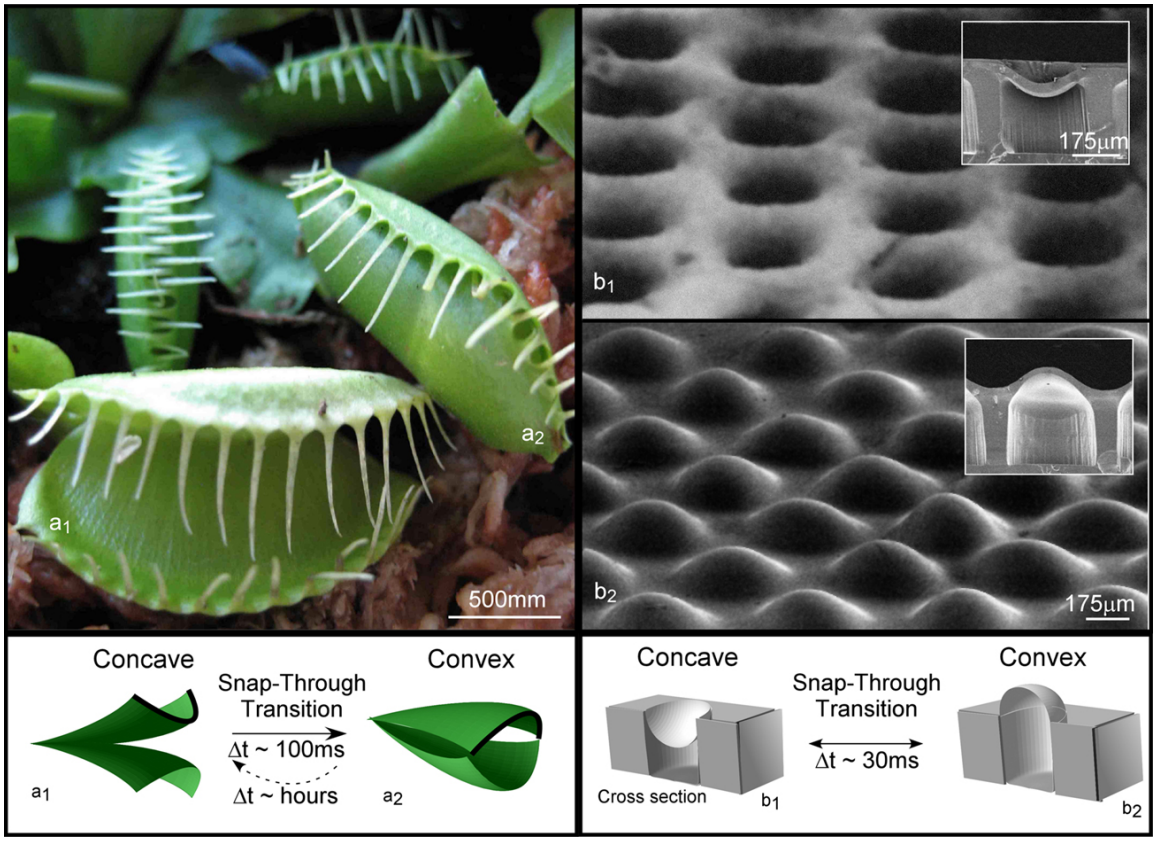

Figure 2.1: Venus Flytrap. Snap-through of the Venus flytrap leaves from concave (a_1) to convex (a_2) occurs through the onset of an elastic instability. Our responsive surface of concave (b_1) microlenses uses the same process to snap to a convex topography (b_2) in $\sim 30ms$.

creating an array of holes. This elastic, PDMS array of holes is then placed in equibiaxial strain through a simple inflation procedure. A thin film of crosslinked PDMS (typically $h = 15$ to $60\mu m$) coated with a thin ($h \sim 1\mu m$) layer of uncured PDMS is placed on the surface of the strained holes. The assembly is heated to crosslink the uncured PDMS and bond the film to the array of holes while under equibiaxial tension. Releasing the tension causes an equibiaxial compressive strain to develop in the thin PDMS coating. The associated compressive stresses cause the circular plate of PDMS on the surface of each hole to buckle, thus creating an array of convex

microlenses. This technique for microlens preparation is simple, robust, and should be scalable to much smaller length scales across a multitude of materials.

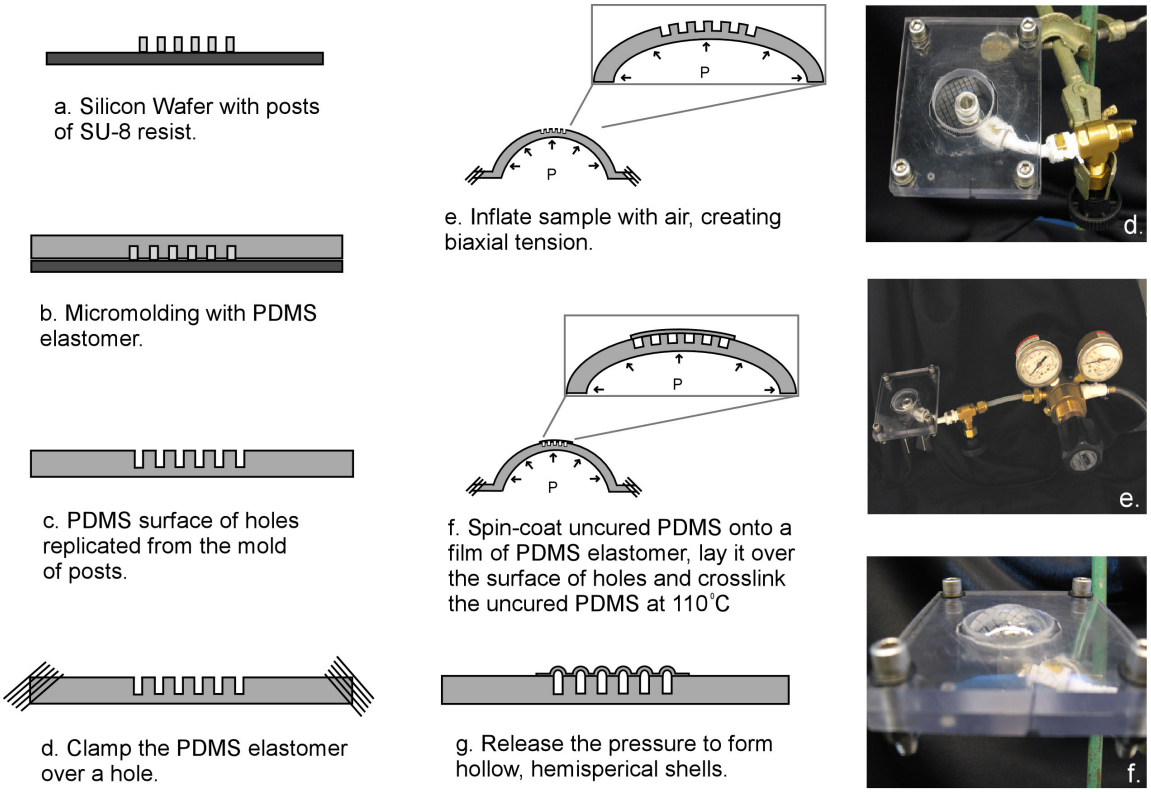

Figure 2.2: Fabrication Schematic. A schematic of the snapping surface preparation along with images of the biaxial inflator. An elastomeric thin film is bonded to a substrate with an array of circular holes that is under biaxial tension. Release of the biaxial tension causes the plates to buckle into spherical caps.

2.3 Results & Discussion

2.3.1 Shell Microstructure Geometry

As a first estimate, the curvature of the microlenses can be predicted by a conservation of surface area, where the cross-sectional area of the hole under equibiaxial tension should equal the surface area of the resultant spherical shell.

$$\pi a_i^2 = 2\pi R w \tag{2.1}$$

where a_i is the initial radius of the inflated hole, R is the shell radius of curvature, and w is the vertical displacement of the shell. While the critical stress that develops from the applied biaxial compression dictates the formation of lenses and is dependent on the film thickness and material properties, the critical strain for formation is independent of material properties and thickness. Accordingly, the geometry of the microlenses produced in our experiments was independent of film thickness for the limited range measured ($h = 15$ to $60\mu m$). Therefore, for a mechanically uncoupled shell, the ratio of the amplitude of the shell to the radius of the hole is proportional to the applied strain (Figure 2.3), where a is the unstrained radius of the hole, ε is the applied strain, and w is the shell's amplitude:

$$\frac{w}{a} = \sqrt{\varepsilon(2+\varepsilon)} \tag{2.2}$$

2.3.2 Shell Inversion

To direct the transition from convex to concave curvature, the stress in the shell structure must be controlled. As described in the continuum mechanics of shell structures, at a critical applied stress an elastic instability will occur [20], similar to Euler buckling of a beam. This critical stress is determined by the balance of geometric and mechanical properties [20]. As one example, individual shells can be snapped by applying a concentrated point force greater than or equal to $\sim 6mN$ to the shells (Figure 2.4). To initiate this snap-through, we brought a cylindrical probe (radius $= 85\mu m$) connected to a load cell and nanopositioner into contact with the apex of a single microlens. Applying a force below the critical force caused the shell to reversibly return to the convex geometry (black data). If the critical concentrated force is applied, the shells snap to the concave state and remain there upon removal of the

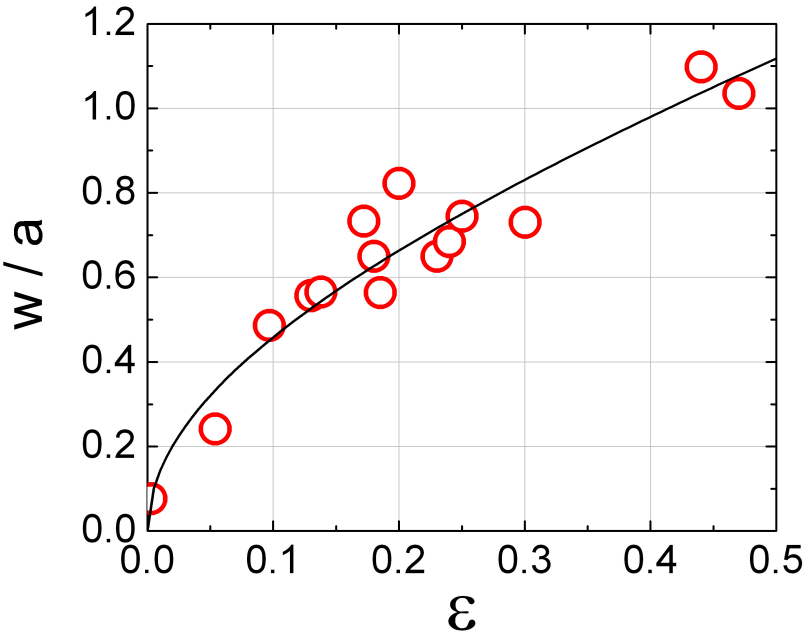

Figure 2.3: Aspect Ratio of Spherical Caps. A graph of w/a vs. ε from equation 2.2 illustrates the predictive control over the aspect ratio of the microstructures based on the conservation of surface area between a circular plate and a buckled shell.

probe (gray data). This change is indicated by the contact force, P, changing to zero at a displacement, $\delta = -150\mu m$.

Alternatively, if a trigger mechanism is used to develop the critical stress in all shells simultaneously, then the entire surface of shells will change curvature (Figure 2.1b). One way to achieve this switching of multiple lenses from convex to concave is by exposing the responsive surface to oxygen plasma treatment. The exposure of the surface to oxygen plasma leads to a conversion of the organo-silicon surface to silicon oxides [29]. This conversion process causes a volumetric decrease on the surface of the PDMS film, triggering the shells to snap from convex to concave to minimize the development of tensile stresses in the outer surface layer.

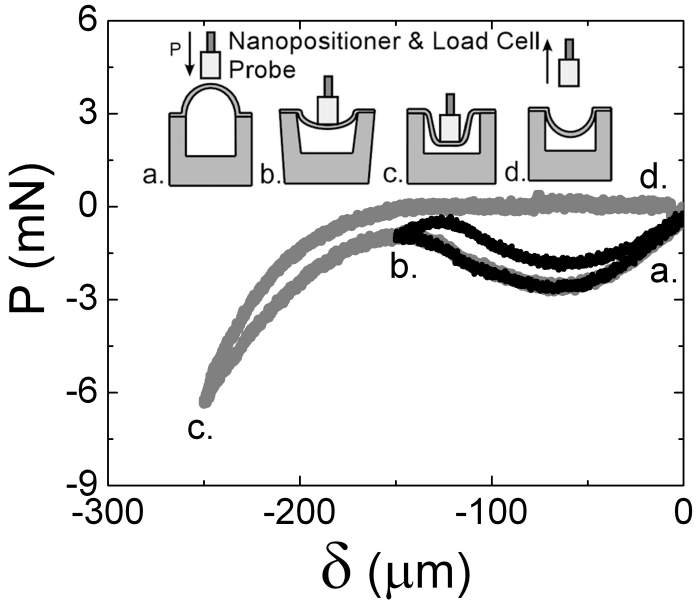

Figure 2.4: Shell Snap-Through via Concentrated Force. A schematic of using a concentrated point force to snap an individual shell, along with a force, P, versus displacement, δ, plot illustrating the critical force for snap-through. The light line represents a convex shell that transitions to a concave geometry upon concentrated loading. The dark line represents a shell that deforms nonlinearly but remains convex as the probe is reversed from the displacement $\delta = 150\mu m$.

2.3.3 Snap-Buckling

2.3.3.1 Stimuli Responsive Trigger

To snap the shells from concave to convex, a triggering mechanism that causes volumetric expansion can be used. We have demonstrated a simple mechanism by swelling our elastic network with an organic solvent to develop an osmotic stress, similar to the Venus flytrap. Hexane was introduced to our PDMS surface, swelling the crosslinked network (Figure 2.6a). The hexane can quickly diffuse through the thin silica layer on the surface ($\sim 10nm$) [29] created by exposure to oxygen-plasma. As the surface swells, it expands initially until a compressive stress is generated due to the lateral confinement from the edges of each hole (Figure 2.6b, where λ_{rr} describes the lateral extension of the hole). This compressive stress leads to a growth of higher buckling modes until a critical strain is reached. At this critical value, the shell

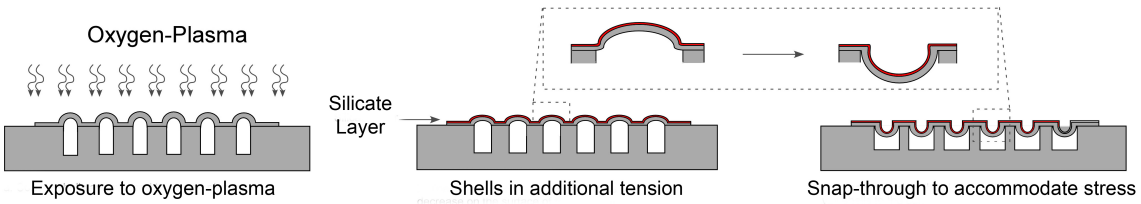

Figure 2.5: Shell Snap-Through via Oxygen Plasma. A schematic illustrating how the exposure of the surface to oxygen plasma places the outer surface of the shells in tension which causes them to change curvature, thereby alleviating the additional stress.

undergoes a snap-through transition to the more stable convex state, with a time-scale defined as τ_p. A complete description of the shell mechanics through this transition has not been accomplished yet and reference to developed analytical solutions is not possible due to the complex boundary conditions. Nonetheless, this transition in stress state can be associated with volumetric expansion in the buckled film, a mechanism that can be associated with a variety of other environmental changes (pH, light, temperature, etc.).

2.3.3.2 Poroelastic Time Scale

Similar to the snapping leaves of the Venus flytrap, an increase in osmotic stress in the elastic membrane of the concave microlenses causes strain to localize in the center of the shells followed by a snap-buckling instability. In the plant kingdom, two time scales are important for quantifying rapid movements. The physical limit for the motion of a self-actuated mechanical system is dictated by the speed that an elastic wave propagates through them, which scales as $\sqrt{E/\rho}$, where ρ is the material's density. Therefore, the inertial time for a membrane of thickness h scales as:

$$\tau_i \sim h\sqrt{\frac{\rho}{E}} \tag{2.3}$$

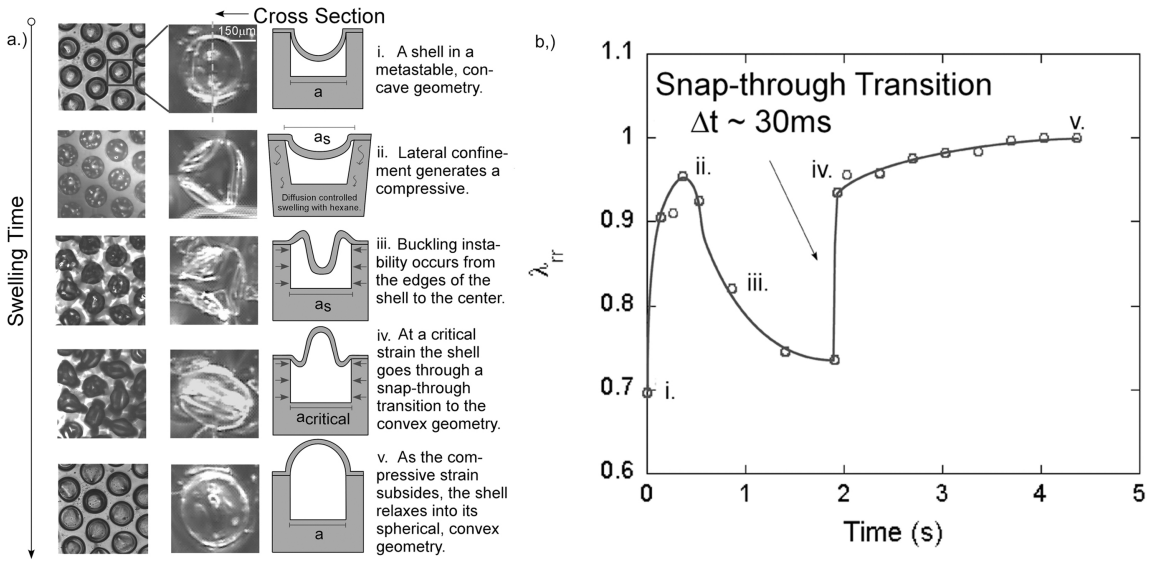

Figure 2.6: Shell Snap-Through via Osmotic Swelling. a. Images of the responsive surface snap-through process as well as a schematic illustrating the snap-through transition of a single shell from concave to convex. The triggering mechanism is the development of osmotic stress, similar to the triggering mechanism observed in the Venus flytrap. The development of osmotic stress in our system is due to the swelling of the PDMS network with hexane. b. A corresponding graph of the extension ratio of the hole plotted against time which illustrates the initial swelling, confinement induced compressive stress, and subsequent snap-through transition.

The second time scale is poroelastic time, τ_p, and it is limited by the time it takes to transport fluid through an membrane. To understand this time scale we consider the physics of water moving through a porous elastic material, such as plant tissue. Assuming the fluid and tissue to be incompressible, fluid flow across a tissue will expand the cells on one side and contract the cells on the other [2]. This movement creates a differential strain which can described by the continuity relation:

$$\varphi\nu = -(1-\varphi)\frac{\delta u}{\delta t} \sim -(1-\varphi)\frac{u}{\tau_p} \tag{2.4}$$

where u is the tissue displacement, ν is the fluid velocity field, and φ is the volume fraction of fluid. Since the fluid is Newtonian and the pore size is constant, we can assume the fluid velocity obeys Darcy's law [2, 30, 31], so that

$$\varphi v = q \tag{2.5}$$

where q is the velocity flux:

$$q = -\frac{\kappa}{\mu}\nabla P \tag{2.6}$$

with κ the hydraulic permeability, and μ the fluid's intrinsic viscosity. Therefore, considering the pressure gradient to be a pressure p acting over the membrane thickness h, equation 2.4 can be rearranged using equations 2.5 and 2.6 into:

$$\varphi\left(v - \frac{u}{\tau_p}\right) \sim \frac{\kappa p}{\mu h} \tag{2.7}$$

Since this fluid flow is related to the elastic stress of membrane, a force balance yields:

$$E\frac{u}{h} \sim \varphi p \tag{2.8}$$

Substituting this equation into equation 2.7 leads to:

$$\varphi\left(v - \frac{u}{\tau_p}\right) \sim \frac{\kappa E u}{\mu h^2 \varphi} \tag{2.9}$$

Finally, we can solve for the poroelastic time by using equations 2.4 and 2.9:

$$\tau_p \sim \frac{\mu h^2}{\kappa E} \tag{2.10}$$

Movements slower than this poroelastic time ($t > \tau_p$) are typically swelling events whose time scale is limited by fluid transport, while movements greater than or equal to this time ($t \leq \tau_p$) are rapid movements. In the case of elastic instabilities, such as snap-buckling, τ will be limited by τ_p. We can therefore use this critical time-scale to describe the snap-through of spherical shells via osmotic stress. Figure 2.7 illustrates a plot of τ_p versus film thickness. The solid line represents a fit of equation 2.10 using a measured value of Young's elastic modulus ($E = 4MPa$), and literature values for the permeation of hexane through PDMS ($\kappa/\mu \sim 10^{-14} m^2 Pa^{-1} s^{-1}$) [32].

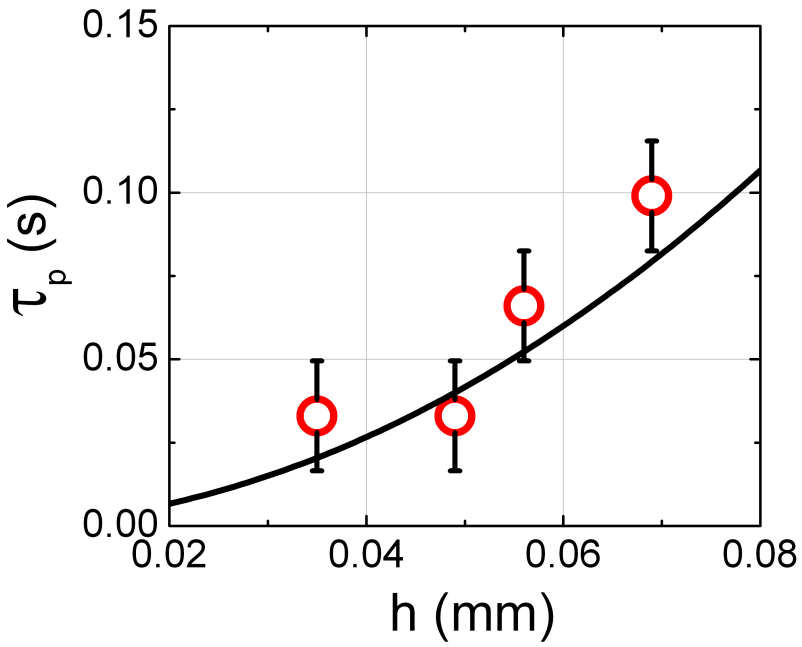

Figure 2.7: Snap-Through Time vs. Thickness. A plot of the critical snap-through time as a function of thickness. The solid line represents equation 2.10, with $E = 4MPa$, and $\kappa/\mu \sim 10^{-14} m^2 Pa^{-1} s^{-1}$.

2.3.3.3 Snap-Buckle versus Smooth Transition

Designing a surface that undergoes snap, not smooth, instability transitions is also linked to the balance of materials properties and geometry. Forterre et al. [1] showed that a dimensionless geometric parameter $\alpha \sim a^4/(R^2h^2)$ determines the nature of closure for the Venus flytrap leaves as either snapping or smooth closure [1], where R is the radius of curvature. They determined that $\alpha > 0.8$ was necessary for leaf snapping. Similarly, this transition in the context of classical shell mechanics, a dimensionless parameter $\xi = w/h$ can be used for spherical shell under fixed edge conditions. For this boundary constraint, ξ must exceed a value of 2. While neither parameter completely describes the boundary conditions of the microlenses presented here, they represent lower limits required for shell snap-through. Our shell geometry has values of α (19.0) and ξ (3.7) which greatly exceed the previously-mentioned critical values of both α and ξ.

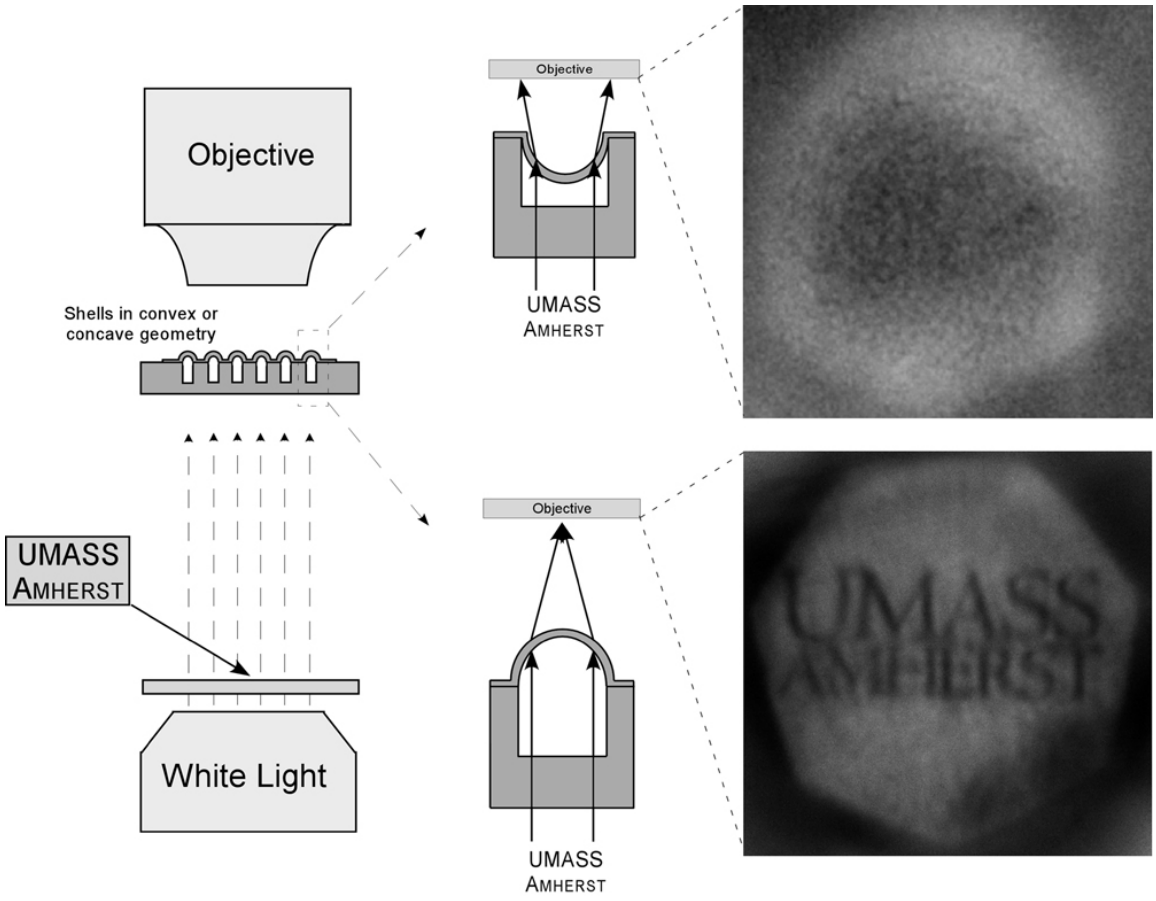

Figure 2.8: Optical Property Control. Demonstration of optical functionality of microlens shells and their ability to change focal properties upon triggering. In the arrangement illustrated schematically on the left, no image is projected onto the objective when the shell curvature is concave. Upon triggering, the shell transitions to convex and an image is focused at the focal point of the microscope objective.

2.3.4 Property Control

2.3.4.1 Optical Property Control

As an initial demonstration of a responsive property of these surfaces, we illustrate the utility of these surfaces as responsive microlens arrays for optical display applications. In a convex state, the assembled shell structures form a functional microlens array (Figure 2.8) with a focal point above the structure surface. Upon transitioning to a concave curvature, the focal point of the shell structures is changed to beneath the shell surface (Figure 2.8). These transitions can occur locally (single lenses) or

over the entire microlens array depending upon the spacing, material properties, and specific nature of the triggering mechanism.

2.3.4.2 Surface Wettability

Surface topography and surface chemistry determine the surface's wetting properties [33]. Therefore, a surface that can dynamically change its topography can alter the wetting of a liquid droplet. As an initial demonstration of the switchable wetting properties of these surfaces, we fabricated a surface of microlenses and measured its contact angle in the convex and concave surface topography, and compared that to a smooth PDMS sample (Figure 2.9). As indicated by the contact angle data, there is a notable difference between the contact angles measured in each state. By tuning the size and surface chemistry (via vapor deposition of a hydrophobic chemical layer, i.e. fluoropolymers) of the microstructures, the contact angle difference will increase significantly [33].

2.4 Summary

In this chapter, we used lessons from the Venus flytrap to design surfaces that dynamically modify their topography. We describe a simple, robust, biomimetic responsive surface based on an array of microlens shells that snap from one curvature (e.g. concave) to another curvature (e.g. convex) (Figure 2.1) when a critical stress develops in the shell structure.

This snap-transition is due to the onset of an elastic, snap-through instability similar to the capture mechanism of the Venus flytrap. The response rates can be over two orders of magnitude faster than the typical response of shape-memory polymers, and the sensitivity and rate of the response can be tuned with predictable geometric and/or material property changes. Based on materials choice, a wide variety of external stimuli can trigger this stress development, such as temperature, pH, solvent

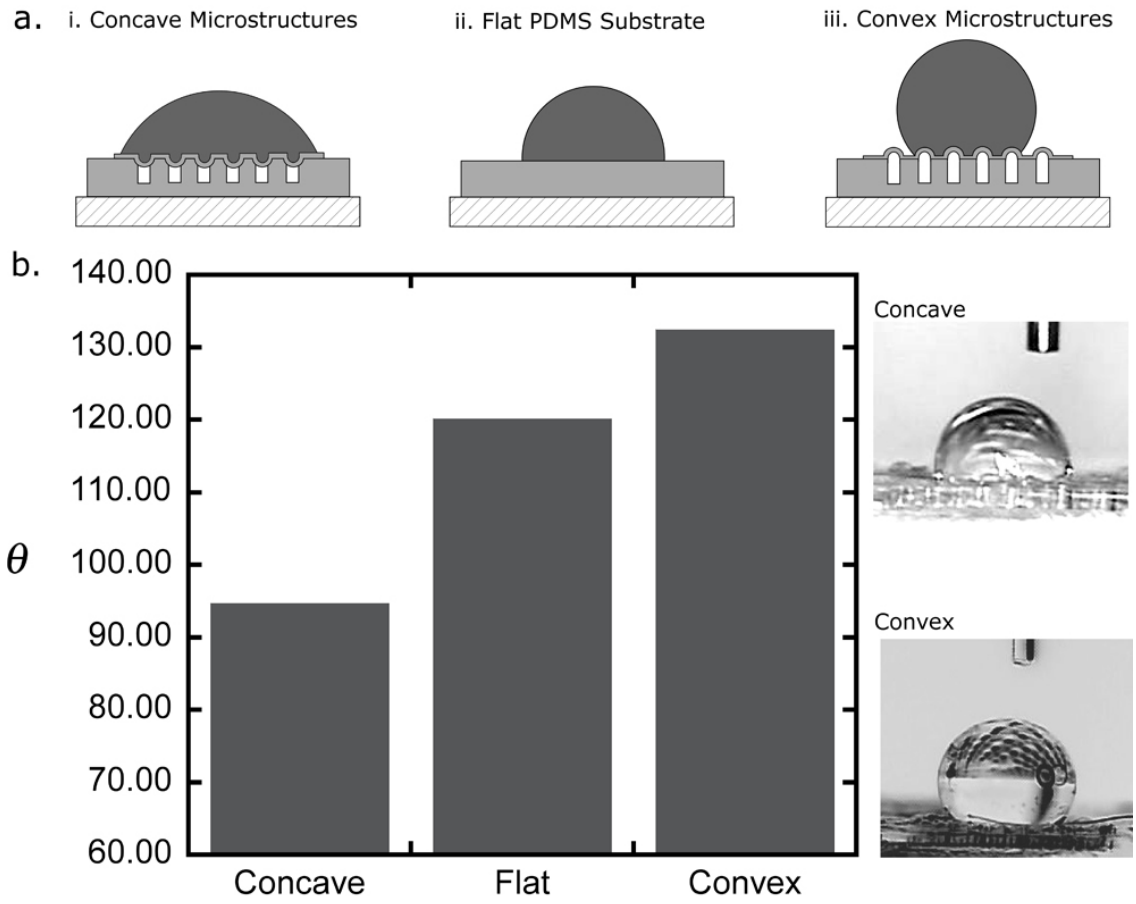

Figure 2.9: Surface Wettability. Demonstration of the wettability of microlens shells as a function of their concavity. The advancing contact angle of a water droplet on the PDMS surfaces was measured for *i*. concave, *ii*. flat, and *iii*. convex topographies. The initial results indicate a small but notable qualitative and quantitative difference in the wettability of the three surfaces.

swelling, magnetism, electric current, and light. This strategy has great potential for the design of responsive surfaces, which will impact a variety of applications including: release-on-command coatings [6] and adhesives [3–5], on-command frictional changes [34, 35], instant modification of optical properties at an interface [7, 8], rapid response drug delivery [9–11] , chemical sensing [12–14], and antimicrobial devices [29].

2.5 Open Questions

To date, very little work has been done to utilize the rapid, snap-buckling instability of shells for responsive surface design. This chapter introduces the wide range of possibilities for these systems. The snap-buckling instability discussed above largely focuses on osmotic stress for triggering responsiveness. This strategy allows us to use scaling predictions from Forterre *et al.* [1] to note that the snap-through time should scale as the thickness squared. This scaling provides an interesting design paradigm for designing rapid, responsive surfaces by simply scaling down the shell thickness. Similarly, scaling down the overall feature size should have a strong impact on the adhesion and wettability of the surfaces [3, 33]. Of greater interest will be the design of materials using different responsive triggers. While snap-buckling triggers such as temperature, pH, magnetism, electricity, and light have been proposed, much work needs to be done in developing these systems. Understanding how the material properties, geometry, and stimuli properties for each of these systems impacts the materials' responsiveness will be crucial for the next generation of responsive materials.

2.6 Acknowledgements

Funding for this work was provided by the Army Research Office Young Investigator Program. The authors thank Dr. Edwin P. Chan and Professor Kyriaki Kalaitzidou for insightful discussions, and acknowledge NSF-MRSEC Central Facilities for use of their SEM, as well as Professor Thomas McCarthy's group for use of their oxygen-plasma cleaner.

CHAPTER 3

CRUMPLED SURFACE STRUCTURES

3.1 Introduction

During the snap-through process described in Chapter 2, we observed a secondary bifurcation occurring in the shells that enable snap-buckling (Figure 2.6). We wanted to explore this shell buckling and understand its impact on material response. Buckling instabilities are widely studied and can impact the response of materials in a variety of ways [36–44]. Rather than focus on the bifurcation that shells undergo during the complicated snap-buckling process, we used the buckling of circular plates and spherical shells to produce structures and patterns that are difficult, if not impossible, to achieve with other methods. In this chapter we will focus on two important questions: 1.) How does the geometry of the microstructures formed in section 2.2 depend on the plates material properties, geometry, and applied force during preparation? and 2.) Can we take advantage of the inherent interplay between microstructure geometry and strain to create dynamic, responsive materials by reversibly changing the microstructure's morphology?

3.2 Experimental Approach

To fabricate the surface patterns, we use the biaxial compression of an array of circular plates (Figure 3.2) to generate microstructured surfaces. The fabrication method is based on work described in section 2.2. When the applied equibiaxial compressive stress exceeds a critical value, the plates buckle into a surface array of microstructures. The film thickness was varied from $9\mu m$ to $55\mu m$ and measured by

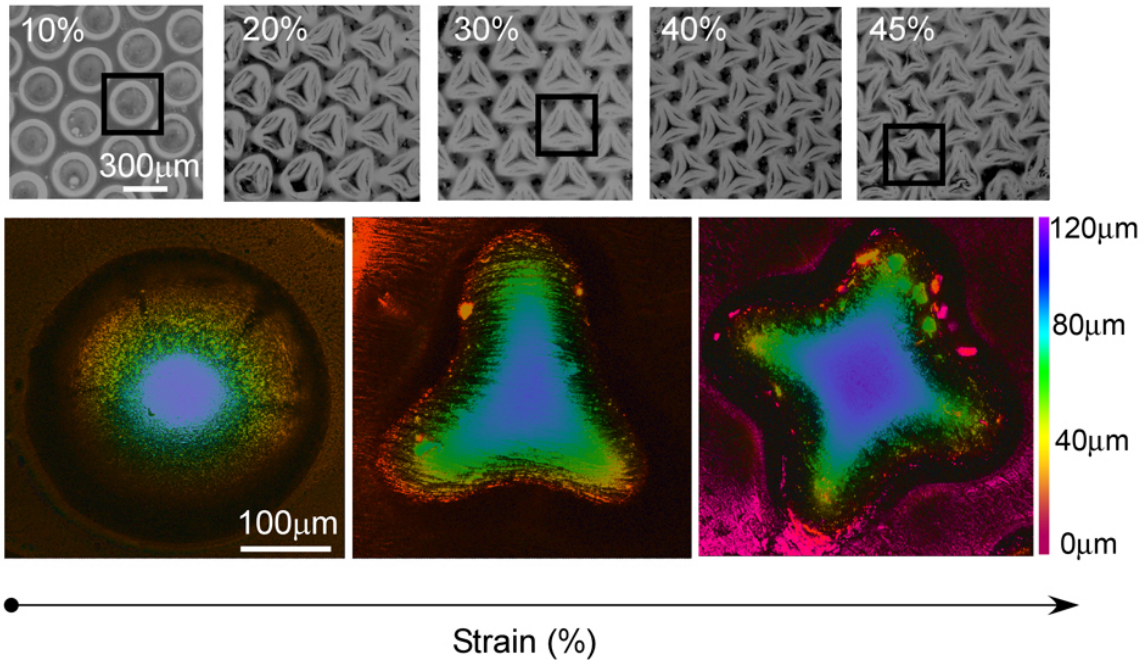

Figure 3.1: Confocal Images of Buckled Plates. Optical and confocal microscopy images of spherical and bifurcated shells. These shells were fabricated with the same plate thickness and radius. The nonaxisymmetric shells form at higher values of compressive equibixial strain.

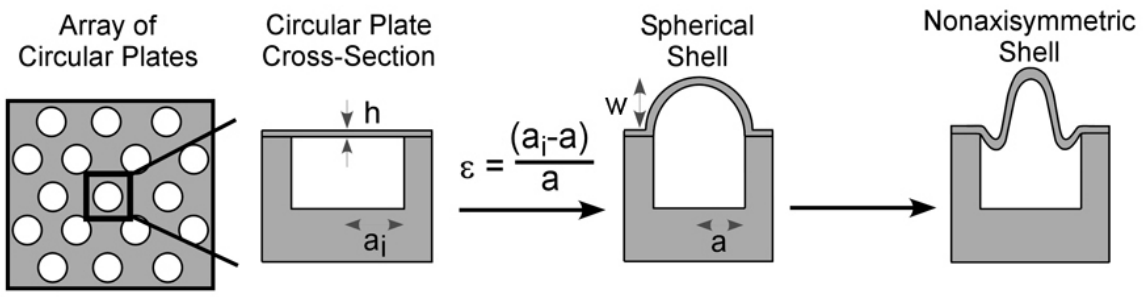

Figure 3.2: Schematic of Buckled Plates. A schematic illustrating an array of individual circular plates buckling from an applied compressive strain into axisymmetric microlenses followed by nonaxisymmetric shells at high strains.

stylus profilometry (Veeco Dektak 3 Stylus Profilometer). The microstructure height was measured by observing the contact of a glass probe controlled by a subnanometer precision inchworm actuator (Exfo Burleigh IW-812) with the shell surface via optical microscopy (Zeiss, Variotech). Geometry of the convex and concave shells was examined by scanning electron microscopy (JOEL 6320FXV FESEM, SEI mode, 10 kV, gold-coated) and confocal microscopy (Leica Confocal Optical Microscope). Swelling of the PDMS thin film was done by depositing a $10\mu L$ droplet of hexane (VWR) onto the surface of spherical microlenses. The swelling of the PDMS substrate was done in a bath of hexane and the substrate was swollen to equilibrium.

3.3 Elastic Instabilities

3.3.1 Buckling Behavior of a Circular Plate

Applying a compressive or tensile force to a confined thin plate can lead to either buckling [45], wrinkling [46–49], or crumpling [38, 39, 44, 50, 51]. For a thin plate, the equilibrium shape is determined by a balance of the elastic plates bending and stretching energy since the in-plane strain is minimal for a thin geometry. The stretching energy scales linearly with the plate thickness, h, while the bending energy scales as h^3, therefore as the plate thickness decreases, the stretching energy term dominates

and the plate bends significantly to reduce the in-plane strain [52]. As a result, the circular plates buckle under lateral compression and form equilibrium structures with high curvatures, due to the plates preference for bending. The specific topography, or shape, of the microstructures is determined by the initial geometry and material properties of each plate, and the applied biaxial strain.

3.3.1.1 Equilibrium Plate Equations

From an equilibrium balance of an elastic plate we can establish the plate's stresses and strains with respect to bending and stretching [45, 53–55]. The bending and stretching strains, ε^b and ε^s, in the radial, r, and transverse, θ, directions are given as:

$$\varepsilon_r^b = -z\frac{d^2w}{dr^2} \tag{3.1a}$$

$$\varepsilon_\theta^b = -\frac{z}{r}\left(\frac{dw}{dr}\right) \tag{3.1b}$$

$$\varepsilon_r^s = \frac{du}{dr} + \frac{1}{2}\left(\frac{dw}{dr}\right)^2 \tag{3.1c}$$

$$\varepsilon_\theta^s = \frac{u}{r} \tag{3.1d}$$

Where u and w are the radial and transverse displacements along the z axis, respectively. Similarly, the bending and stretching stresses, σ^b and σ^s, in the radial and theta directions are given as:

$$\sigma_r^b = -\frac{Ez}{1-\nu^2}\left(\frac{d^2w}{dr^2} + \frac{\nu}{r}\frac{dw}{dr}\right) \tag{3.2a}$$

$$\sigma_\theta^b = -\frac{Ez}{1-\nu^2}\left(\frac{1}{r}\frac{dw}{dr} + \nu\frac{d^2w}{dr^2}\right) \tag{3.2b}$$

$$\sigma_r^s = \frac{Ez}{1-\nu^2}\left(\frac{du}{dr} + \frac{1}{2}\left(\frac{dw}{dr}\right)^2 + \nu\frac{u}{r}\right) \tag{3.2c}$$

$$\sigma_\theta^s = \frac{Ez}{1-\nu^2}\left(\frac{u}{r} + \nu\frac{du}{dr} + \frac{\nu}{2}\left(\frac{dw}{dr}\right)^2\right) \tag{3.2d}$$

Where E is Young's elastic modulus and ν is Poisson's ratio. The bending moments, M, along the radial and transverse directions are:

$$M_r = \int_{-h/2}^{h/2} \sigma_r^b z \quad dz = -D\left[\frac{d^2w}{dr^2} + \frac{\nu}{r}\frac{dw}{dr}\right] \tag{3.3a}$$

$$M_\theta = \int_{-h/2}^{h/2} \sigma_\theta^b z \quad dz = -D\left[\frac{1}{r}\frac{dw}{dr} + \nu\frac{d^2w}{dr^2}\right] \tag{3.3b}$$

Where D is the plate stiffness,

$$D = \int_{-h/2}^{h/2} \frac{E}{1-\nu^2} z^2 dz = \frac{Eh^3}{12(1-\nu^2)} \tag{3.4}$$

For a plate in equilibrium, the internal stresses in every volume element must balance. Therefore the equations of equilibrium are [56]:

$$\frac{\partial \sigma_{ik}}{\partial x_k} = 0 \tag{3.5}$$

Since the plate is independent of the coordinate z, the equations of equilibrium in Cartesian coordinates reduce to:

$$\frac{\partial \sigma_{xx}}{\partial x} + \frac{\partial \sigma_{xy}}{\partial y} = 0 \tag{3.6a}$$

$$\frac{\partial \sigma_{yx}}{\partial x} + \frac{\partial \sigma_{yy}}{\partial y} = 0 \tag{3.6b}$$

By taking equations 3.6a and 3.6b in cylindrical coordinates we can solve for the equilibrium equation for radial forces acting upon an element of a plate:

$$\sigma_r^s + r\frac{d\sigma_r^s}{dr} - \sigma_\theta^s = 0 \tag{3.7}$$

Using the radial force equilibrium along with equation 3.3a, the radial moment equilibrium may subsequently be derived as:

$$M_r + r\frac{dM_r}{dr} - M_\theta + \sigma_r^s h\frac{dw}{dr}r = 0 \tag{3.8}$$

Using equations 3.2c, 3.3a, and 3.3b, and taking the derivative of M_r with respect to r to be $dM_r/dr = -D(d^3w/dr^3 - \nu/r^2 dw/dr + \nu/r d^2w/dr^2)$ we can solve for the equilibrium plate equation in terms of d^3w/dr^3:

$$\frac{d^3w}{dr^3} = -\frac{1}{r}\frac{d^2w}{dr} + \frac{1}{r^2}\frac{dw}{dr} + \frac{12}{h}\frac{dw}{dr}\left[\frac{du}{dr} + \frac{1}{2}\left(\frac{dw}{dr}\right)^2 + \nu\frac{u}{r}\right] \tag{3.9}$$

By defining $\alpha \equiv dw/dr$, $\mu^2 \equiv hp/D$, and $\sigma_r^s \equiv -p$ we can rearrange the equilibrium plate equation into:

$$r^2\frac{d^2\alpha}{dr^2} + r\frac{d\alpha}{dr} + (\mu^2 r^2 - 1)\alpha = 0 \tag{3.10}$$

This is recognized as Bessel's differential equation. The general solution of this equation is:

$$\alpha = A_1\mathcal{J}_1(r) + A_2\mathcal{Y}_1(r) \tag{3.11}$$

where $\mathcal{J}_1(r)$ and $\mathcal{Y}_1(r)$ are Bessel functions of the first and second kinds, respectively. To solve the equilibrium plate equation we need to define the boundary conditions of the plate. To satisfy the condition of symmetry in the plate we note that the angle, α, must be zero at the center of the plate. The function $\mathcal{Y}_1(r)$ becomes infinite as $r = 0$, which requires that $A_2 = 0$. Therefore, to satisfy this equation the first boundary condition must be:

$$\alpha_{r=a} = 0 \tag{3.12}$$

As a second boundary condition we must consider the condition at the edge of the plate. In this case the surface of the plate with respect to the original horizontal plane is proportional to the radial edge moment (equation 3.3a):

$$\frac{D\xi\alpha}{a} = -D\left(\frac{d\alpha}{dr} + \nu\frac{\alpha}{r}\right) \tag{3.13}$$

The restraint along this edge is described by ξ, where $\xi = 0$ for a simply supported edge and $\xi = \infty$ for a clamped edge. This leads to a general solution to equation 3.10 which can be used to solve for the critical buckling stress, $p = -\sigma$:

$$\sigma_c = \frac{kD}{a^2 h} \tag{3.14}$$

To convert this critical stress to a critical strain we can use the equibiaxial stress-strain relationship from continuum mechanics:

$$\sigma = E\left[\frac{\varepsilon + \nu\epsilon}{(1-\nu^2)}\right] \tag{3.15}$$

This relationship dictates that the critical equibiaxial strain to buckle a circular plate is:

$$\varepsilon_c = \frac{k^2}{12(\nu+1)}\left(\frac{h}{a}\right)^2 \tag{3.16}$$

Considering a simply supported edge, $\xi = 0$, within equation 3.13, the second boundary condition which describes the plate's edge is:

$$\left(\frac{d\alpha}{dr} + \nu\frac{\alpha}{r}\right) = 0 \tag{3.17}$$

Using the derivative formula $d\mathcal{J}_1/dr = \mathcal{J}_0 - \mathcal{J}_1/r$, where $\mathcal{J}_0$ is the Bessel function of zero order, we can express the boundary condition for a simply supported plate as:

$$k\mathcal{J}_0(k) - (1-\nu)\mathcal{J}_1(k) = 0 \tag{3.18}$$

By assuming that for PDMS the Poisson's ratio is $\nu \approx 0.49$ we can use the tables for Bessel functions of the zeroth and first order to find that $k = 2.16$ for the first

buckling mode of a simply supported circular plate under equibiaxial compression. This value is used in equation 3.16 to determine the strain required for the first mode of buckling for a circular plate. The resultant equation is plotted as the solid line in figure 3.3. The data presented below this line (open circles) did not buckle while data points above it (closed circles) exhibited buckling with an aspect ratio described by equation 2.2.

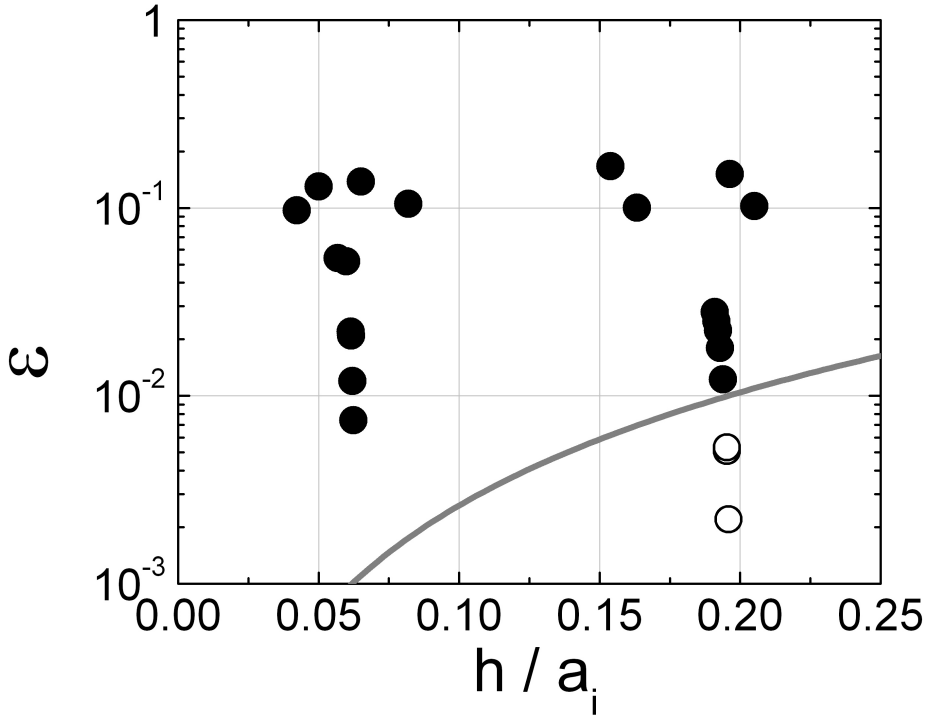

Figure 3.3: Buckling Phase Map. A phase map of ε vs. h/a_i demonstrating the buckling modes of a circular plate under compression. The solid line is from equation 3.16 where $k = 2.16$. Data presented in the region below this line (open circles) did not buckle under equibiaxial compression, while data above the line (closed circles) buckled into axisymmetric, spherical shells. Both results confirm the predictions made by classical plate theory.

3.4 Results & Discussion

3.4.1 Convex Shell Formation

Due to the boundary condition of asymmetric bonding at the plates' edge, and the change in volume in the encapsulated microwells, buckling always produces structures with a convex shape. During fabrication, the volume enclosed beneath the microstructures changes. Assuming ideal gases, the pressure change is given by $\Delta p = P_{atm}(V_i/V_f - 1)$, where Δp is the change in pressure, P_{atm} is the atmospheric pressure, and V_i and V_f are the initial and final volumes. If the structures form in a concave state, the volume of the encapsulated microwells decreases, leading to a pressure increase. This pressure increase always exceeds the pressure decrease associated with the convex structure formation, thus convex formation is preferential. Although the concavity of the structures is impacted by this pressure difference, the resultant shape is not significantly affected. For our microstructures, $\Delta p/E \sim 10^{-4}$ to 10^{-2}, making the effect of pressure change on the buckled plate geometry negligible for these materials. This relationship suggests that for softer materials or shallower hole depths, the pressure change may impact the resultant geometry.

3.4.2 Secondary Bifurcation

Once above the critical threshold for buckling a circular plate, applying additional compressive strain (as illustrated in figure 3.2) to an axisymmetric shell will cause it to undergo a secondary bifurcation. This leads to the formation of nonaxisymmetric shells that exhibit circumferential waves along the base of the shell (Figure 3.4). Some insight into the onset and shape of the nonaxisymmetric shells can be gained by considering the bifurcation of a spherical shell. At an applied ε, a spherical shell is created with an aspect ratio of w/a defined by equation 2.2. In this initial state, the base edge of the shell is resisting an applied bending moment related to a, ε, and E. As Shilkrut numerically demonstrated [20], for spherical shells of $w/h = 3$, the

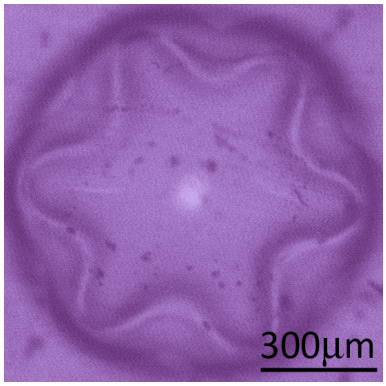

Figure 3.4: Nonaxisymmetric Shell. Optical micrograph of a nonaxisymmetric shell with circumferential waves along its base.

applied bending moment is resisted by a stable surface of constant curvature. For spherical shells with $w/h > 6$, the applied bending moment leads to the bifurcation and secondary buckling of the spherical shell, causing a break in asymmetry [20,37].

This bifurcation leads to local bending to minimize in-plane strain, causing waves in the circumferential direction, and effectively resists the applied bending moment. The shape of the bifurcated shell is related to the surface metric tensor determination of the Gaussian curvature, similar to discussions by Klein et al. for elastic sheets [52].

In figure 3.5, the phase diagram from figure 3.3 is now updated to illustrate the applied biaxial compressive strains that cause non-spherical geometries for circular plates with different h/a_i. Empirically, the transition between axisymmetric and nonaxisymmetric shells appears to occur above $\varepsilon \sim 15\%$. The data above this strain exhibits nonaxisymmetric geometries (solid triangles), while the data for circular plates in between the dashed and solid lines buckle and form axisymmetric spherical shells (solid circles).

Additionally, the geometry of our bifurcated shells is determined by the packing density and configuration of the patterned surface. In the case of hexagonally packed circular plates, the bifurcation of an individual spherical shell creates a microstructure with inflection points, creating a tri-fold symmetry (Figure 3.6a). This geometry

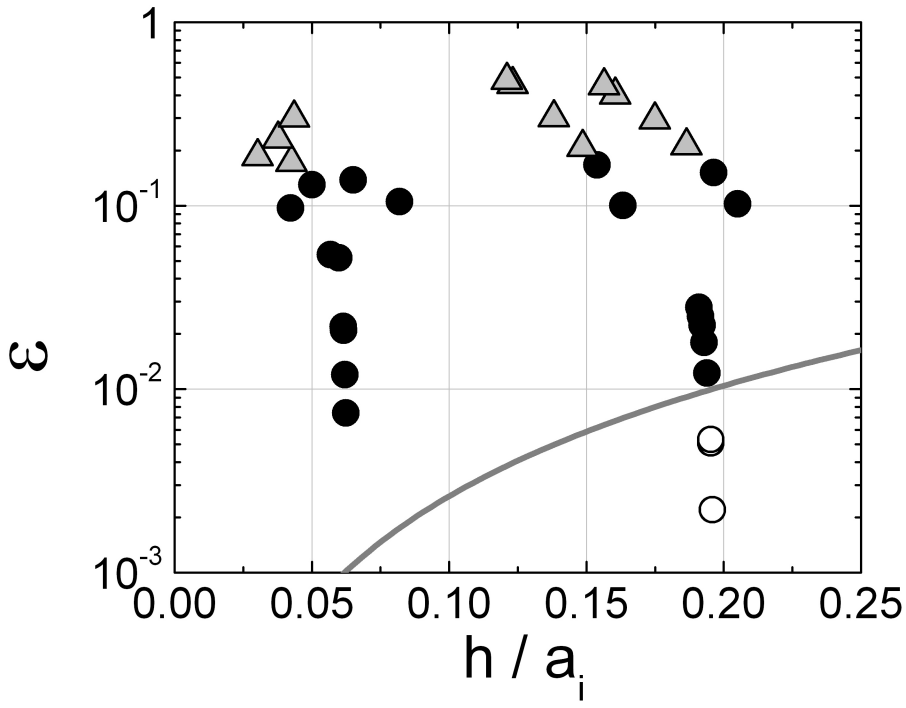

Figure 3.5: Buckling Phase Map with Bifurcated Shells. Building upon the phase map from figure 3.3 by adding data the spherical shells that bifurcate into nonaxisymmetric shells (closed triangles). This transition appears to occur at $\varepsilon \sim 15\%$.

influences the orientation of the shells nearest neighbors. The shells couple together and the stress concentration from each of the three buckle folds of a single shell direct the inflection points of its nearest neighbor (Figure 3.6b). The geometric coupling of these shells is also evident when the shells exhibit a four-fold symmetry. Again, the stress concentration from the folds of the shell directs the inflection points of its nearest neighbors. This suggests a method for controlling the long-range order of these patterned features using defects to template order.

3.4.3 Microstructure Responsiveness

By changing strain through environmental triggers, the relationship between shell geometry and strain defines a responsive surface of microstructures that can dynamically change their shape. Depending on the material properties of the patterned

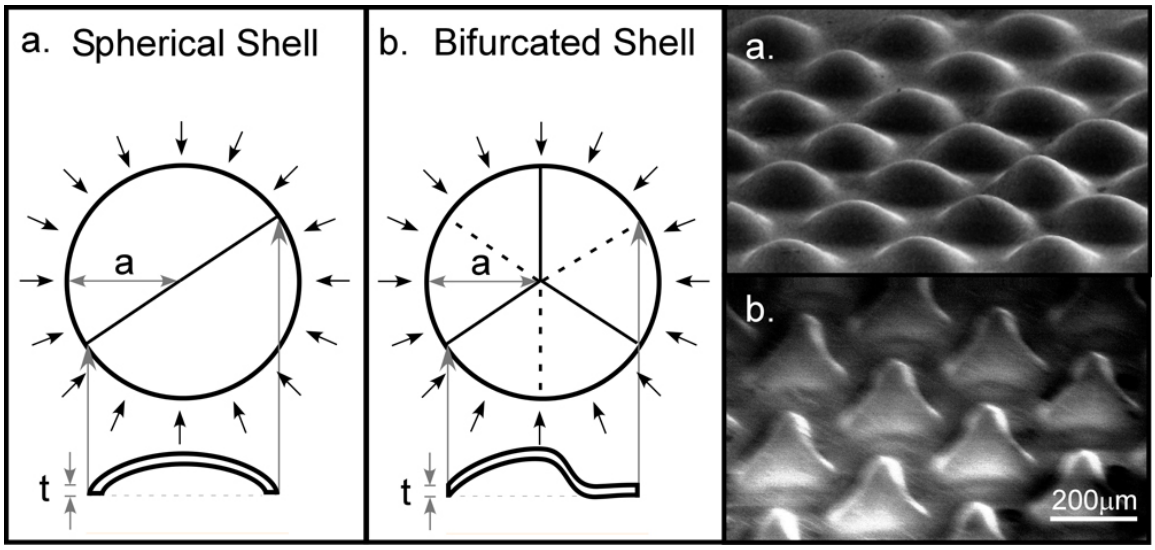

Figure 3.6: Buckling Schematic and SEM Images of Buckled Plates. Schematic illustrating various plate buckling possibilities, where a. illustrates a plate that buckles to form an axisymmetric, spherical shell, and b. shows spherical shells that have bifurcated and exhibit circumferential waves dictated by the packing density of the shells. SEM images of spherical and nonaxisymmetric shells are presented in a. and b.

surface, a variety of stimuli can be used to change the strain applied to the shell structures. As one example, we use swelling of the PDMS network with hexane to change the applied strain. When a hexane droplet is added to the surface of initially spherical shells (Figure 3.7a-ii), the thin film shell swells initially, but is laterally confined by the edges of the unswollen hole below it, to which it is bound. This lateral confinement increases the compressive strain along the edge of the shell, which from equation 6 increases the height of the shell when a remains constant. Since the change in film thickness is negligible, the shell transitions through a bifurcation point to form a stable, nonaxisymmetric geometry (Figure 3.7b-ii). Upon evaporation of the solvent, the shell returns to its initial, spherical geometry. The swelling time required to induce this change is on the order of seconds.

The reverse topographical change can occur by changing the diameter of the hole below an initially nonaxisymmetric shell structure. To demonstrate this change, we

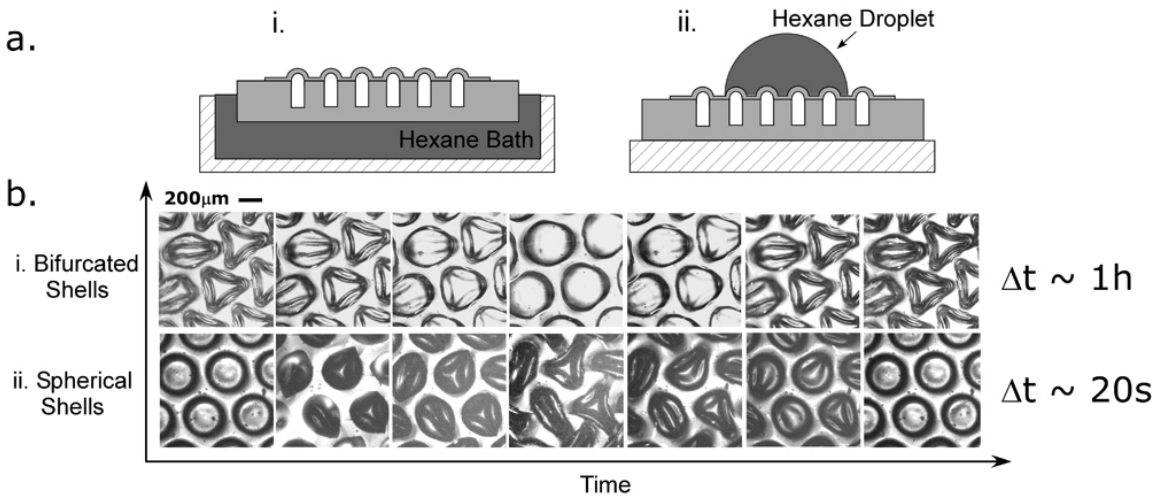

Figure 3.7: Reversible Crumpling. a. A schematic illustrating two (i and ii) manners of responsive behavior in the microstructures. b-i. The responsiveness of convex shells that are initially nonaxisymmetric and form spherical shells as the substrate swells with hexane. b-ii. Shells that are initially spherical bifurcate to form nonaxisymmetric geometries when the shells are swollen with hexane.

swelled the PDMS substrate below the thin film shell with hexane to increase the hole diameter (Figure 3.7a-i). This increase in a causes a decrease in the compressive biaxial strain along the edge of the shell, which in turn decreases the height of the shell to achieve an h/t value where an axisymmetric shell can resist the relieved bending moment in a stable manner (Figure 3.7b-i). Therefore, the initially nonaxisymmetric shell forms a spherical shell geometry. The timescale for this process is approximately an hour as the entire PDMS substrate needs to swell before the shell layer. This process allows the surface to return to its initial topography once the hexane evaporates.

3.5 Summary

In summary, we have presented a simple, scalable patterning method to generate a variety of controlled, tunable surface topographies that would be difficult, if not impossible, to achieve using current fabrication techniques. The geometry of these

microstructures can be understood using classical plate buckling and shell theory. The topography can be tuned by varying the plate's geometry, material properties, and applied biaxial strain. The resulting surface patterns can dynamically and reversibly change shape and aspect ratio by changing the strain applied to the shell structures. The shells change between a spherical, axisymmetric geometry and a bifurcated, non-axisymmetric shape with circumferential waves along the base of the structure. The spherical shells form above a critical strain predicted by classical plate theory, while the nonaxisymmetric shells appear to form above an applied strain greater than 15%. This surface patterning strategy brings a greater understanding to the ability for a shell to localize strain, while also offering a novel approach for the fabrication of the next generation of surface patterns, especially in the context of responsive materials.

3.6 Open Questions

A significant amount of experimental and theoretical work has surrounded the stability of plates and shells [19, 20, 45, 55, 57]. Much of this work has focused on large, single shells. The work in this chapter focused on the stability of an array of shells. Two important considerations are: 1.) the development of an analytical understanding for bifurcation of the axisymmetric shells, and 2.) the impact of the neighboring shells on the stability and responsiveness of the surface. Understanding and predicting when axisymmetric shells undergo bifurcation will allow better control for pattern formation and responsive surface design. The responsiveness of the shells, as described in section 3.4.3, suggests an interplay between the structures and their topography. The coupling between microstructures will impact both their geometry and responsiveness. The ability to understand and control this coupling will be important not only for the responsiveness described in this chapter, but for coordinating the snap-buckling of shells (Chapter 2).

3.7 Acknowledgements

We would like to thank NSF-REU Michal Ursiny for important experimental contributions to this work. Funding for this work was provided by the Army Research Young Investigator Program as well as the NSF-MRSEC REU Program. The authors acknowledge NSF-MRSEC Central Facilities for use of their SEM and Confocal Microscope.

CHAPTER 4

DELAMINATION FOLDING

4.1 Introduction

The pre vious two chapters discuss the strain localization in geometric snap-buckling and spherical shell bifurcations. To better understand the localization of strain within a film, we studied the delamination and folding of a uniaxially compressed, thin polymer film. Delamination has been studied extensively both experimentally [37,58–60] and theoretically [22,61–63], but relatively little work has focused on the deformation profile of delaminated regions for ultrathin polymer films. Specifically, we are interested in measuring the deformation process as the bending curvature of a delaminated glassy film approaches the length scale of an individual molecular coil in an amorphous glass (Figure 4.1). This research will allow us to probe the limits of strain localization, which also will uniquely control deformations in films consisting of a finite number of molecules through their thickness. Studying crumpling and folding in confined geometries not only provides insight into the material properties, but also provides new insight for controlling the morphology and structure of thin polymer films for advanced applications, such as patterning on sub-100nm length scales.

4.2 Beam Bending

The delamination and buckling of thin films is related to a general class of elastic instabilities. The use of materials in engineering structures ranging from bridges to airplanes makes the study of elastic instabilities of great importance. This subject has been studied extensively both theoretically and experimentally for many years,

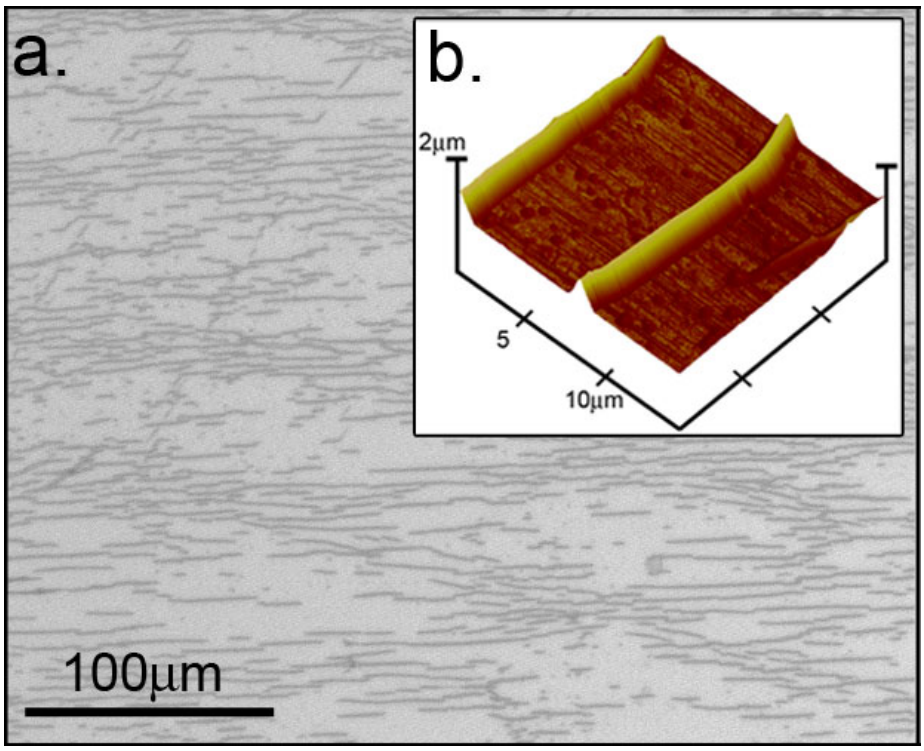

Figure 4.1: OM and AFM of folds. *a*. Optical micrographs of a folded polystyrene film on an elastomeric substrate ($h = 60$nm, $\varepsilon = 0.01$). *b*. AFM image of individual folds on the surface.

with the first problems regarding elastic instabilities being studied over 200 years ago by Leonard Euler [64]. In the theory of elasticity for elementary beam bending, it is known that stresses and deflections in beams are directly proportional to the applied loads [19]. Therefore, by knowing the initial configuration of the beam, it is possible to calculate all of the deflections, stresses, and moments acting upon the beam. The basic differential equations for beams can be derived by considering a beam subjected to an axial compressive force P and a distributed load q which varies along the x axis. From the equilibrium element illustrated by the inset of figure 4.2 we can write the balance of forces acting upon the beam:

$$-V + qdx + (V + dV) = 0 \tag{4.1}$$

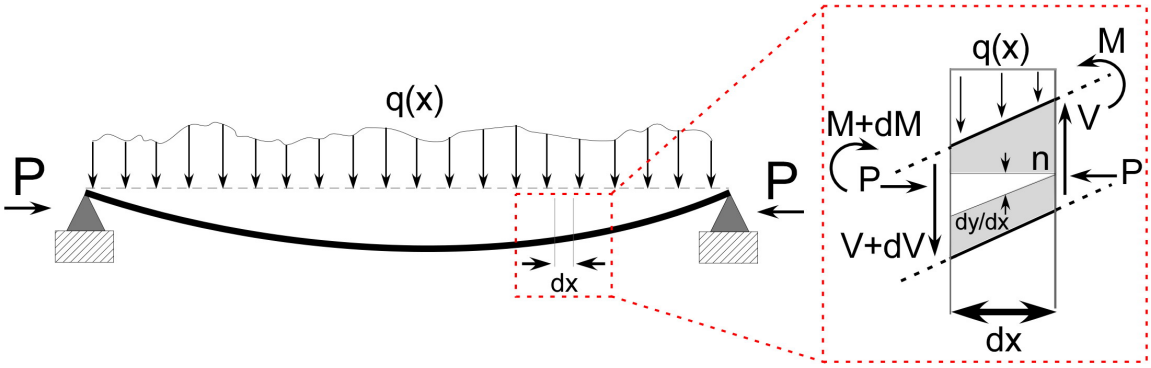

Figure 4.2: Beam Bending Under a Distributed Load. A beam bent under a distributed load $q(x)$ and an axial load P with the inset representing an differential element of the beam in equilibrium. From this equilibrium illustration we can derive equations 4.1 and 4.2.

where V is the shear force acting vertically on the element of the beam. If you then consider the moments acting around the point n while assuming a small deflection, the equilibrium equation becomes:

$$M + qdx\frac{dx}{2} + (V + dV)dx - (M + dM) + P\frac{dy}{dx}dx = 0 \tag{4.2}$$

By solving this equation for the shear force and neglecting higher order terms we see that:

$$V = \frac{dM}{dx} - P\frac{dy}{dx} \tag{4.3}$$

The equation for the curvature of the axis of the beam can be determined by considering EI to be the flexural rigidity of the bending beam, such that:

$$EI\frac{d^2y}{dx^2} = -M \tag{4.4}$$

Therefore, by combining equations 4.1, 4.2, and 4.3 we can determine the differential equations of a beam as:

$$EI\frac{d^3y}{dx^3} + P\frac{dy}{dx} = -V \tag{4.5a}$$

$$EI\frac{d^4y}{dx^4} + P\frac{d^2y}{dx^2} = q \tag{4.5b}$$

4.2.1 Euler Buckling

In section 1.2.1 we discussed Euler buckling using an energy balance approach [19]. Here we approach the same problem using the equilibrium equations for a beam to consider its stability under an axial load P that deforms with a displacement δ [64] (Figure 1.2). The initial deformation scales linearly with a constant stiffness, described by the slope ($K = \Delta P/\Delta\delta$). A further increase in loading causes the beam to reach a bifurcation point, where the beam can either continue deforming axially or undergo a buckling instability. While both represent equilibrium states, the buckling instability is energetically favorable, allowing an elastic instability to occur [19].

Using equation 4.4, which describes the deflection of a beam, we can solve for the beam's critical buckling load. When the beam is in a slightly deflected position, the bending moment at any cross section of the beam is:

$$M = -P(\delta - y) \tag{4.6}$$

Therefore, the equilibrium plate equation becomes:

$$EI\frac{d^2y}{dx^2} = P(\delta - y) \tag{4.7}$$

Under the boundaries where the upper end of the beam is free and the lower end is fixed, the buckling will occur in the plane of minimum flexural rigidity. We will define a buckling constant, k, as:

$$k^2 = \frac{P}{EI} \tag{4.8}$$

Using k^2 we can rewrite equation 4.7 as:

$$\frac{d^2y}{dx^2} + k^2y = k^2\delta \tag{4.9}$$

The general solution of this equation is:

$$y = A\cos kx + B\sin kx + \delta \tag{4.10}$$

where A and B are constants of integration. By applying the boundary condition of a fixed edge:

$$y_{x=0} = \frac{dy}{dx} = 0 \tag{4.11}$$

then equation 4.10 becomes:

$$y = \delta(1 - \cos kx) \tag{4.12}$$

The second boundary condition requires the upper end of the beam to be free, such that:

$$y_{x=l} = \delta \tag{4.13}$$

This boundary condition is satisfied if:

$$\delta\cos kl = 0 \tag{4.14}$$

Since equation 4.14 requires that either $\delta = 0$ or $\cos kl = 0$ and $\delta = 0$ implies that the beam does not buckle, $\cos kl = 0$ dictates that:

$$kl = (2n - 1)\frac{\pi}{2} \tag{4.15}$$

where n is an integer that allows this equation to determine values of k at which a buckled shape can exist, and since $n = 1$ represents the smallest value of kl, equation 4.15 becomes:

$$kl = l\sqrt{\frac{P}{EI}} = \frac{\pi}{2} \tag{4.16}$$

Since the value of P in equation 4.16 represents the smallest critical load for buckling, we can solve for P_c:

$$P_c = \frac{\pi^2 EI}{4l^2} \tag{4.17}$$

This classical understanding of how a beam responds under an applied load can be used to explore the loading of a thin film bound to a substrate.

4.3 Experimental Approach

The deformed polymer films can be prepared either directly onto a silicon wafer or onto an elastomeric substrate treated with ultraviolet light in the presence of ozone. The result is a polymer film with numerous delaminated deformations on the surface (Figure 4.1). The substrate is placed in uniaxial tension and a polystyrene (PS) thin film ($M_W \sim 400,000 g/mol$), prepared via flow-coating ($h = 5nm$ to $h = 100nm$), is brought into contact with the substrate. Upon release of the uniaxial strain the thin film delaminates and buckles (Figure 4.3). The film delamination that occurs at localized regions is dictated by the balance of mechanical strain energy and adhesion strength of the polystyrene and the substrate. The film thickness was measured by ellipsometry and the delaminated features were examined via optical microscopy and atomic force microscopy (AFM).

4.4 Results & Discussion

We can treat the film delamination and subsequent buckling as if it were a clamped plate under uniaxial compression. In this regard, the buckled film should take on a geometry as dictated by the general solution to the equilibrium plate equation (Equation 4.10). Applying the clamped boundary conditions to the film, the shape of the delaminated features becomes:

$$\frac{w}{w_{max}} = \frac{1}{2}\left(1 + \cos\frac{\pi x}{a}\right) \tag{4.18}$$

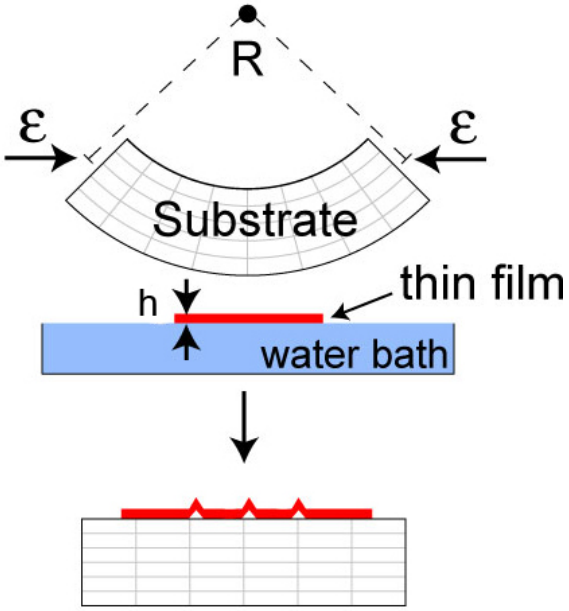

Figure 4.3: Delamination Folding Schematic. A schematic of the fabrication of the folded thin polymer film by placing a substrate in tension and picking up a floating polymer film. Upon release of the tension in the substrate the uniaxial compressive strain causes the polymer film to delaminate and buckled perpendicular to the applied strain.

Cross sections of delaminated features were measured with AFM and are plotted in figure 4.4. These representative cross sections are from $25nm$ films compressed at strains of $\varepsilon \sim 10^{-4}$ and $\varepsilon \sim 10^{-3}$ and are fit with equation 4.18 without any additional fitting parameters.

4.4.1 Strain Localization

Figure 4.6 provides a plot of the feature radius of curvature at the apex of the feature, R, over its film thickness, h, as a function of macroscopically applied strain, ε (Open circles). The result shows two distinct regions in the buckling process for the thin polymer films. As the compressive strain is applied to the polymer film, the initially delaminated region deforms and buckles out of plane, forming a bent region with a constant curvature ($\varepsilon < 0.001$). Further applied strain causes the bent region

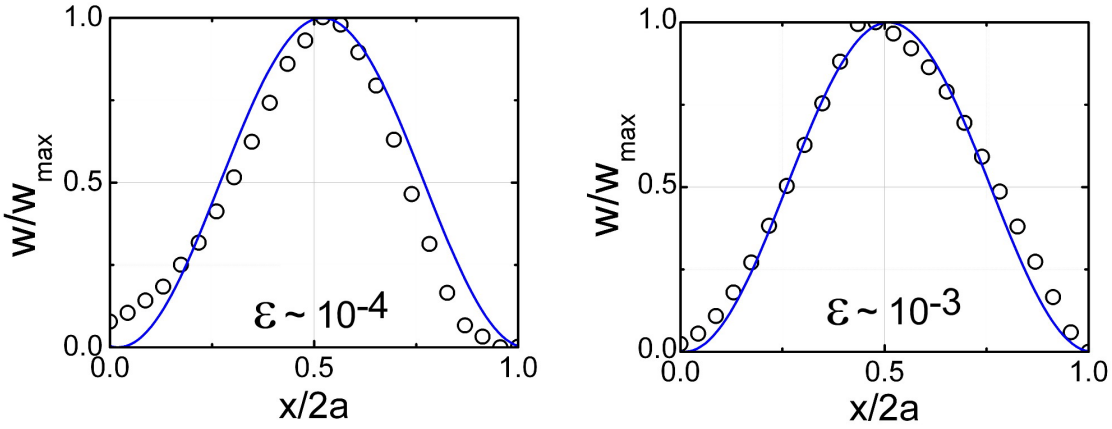

Figure 4.4: Normalized Buckled Height & Width of Delaminated Features. Two representative AFM cross sections of delaminated features fit with the cosine function from equation 4.18 without additional fitting parameters, as predicted by Euler buckling described. Both cross sections are from films of $h = 25nm$.

to localize strain at the midpoint of the feature until a minimum R/h is reached. Beyond this minimum sharpness ratio, additional strain increases the applied energy release rate of the material and causes further delamination to occur 4.5 ($\varepsilon > 0.001$). At low strains, R/h is initially very large and the buckled film has a smooth curvature. A crosssection of the sample's AFM image is presented in figure 4.7a, plotted with the normalized height, h, and curvature, κ. Since the curvature of the bent deformation remains roughly constant across its buckle width, strain is not initially localized along

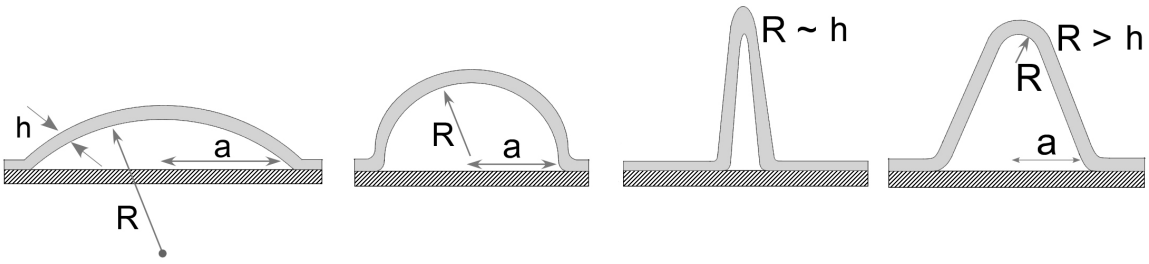

Figure 4.5: Bend to Fold to Delamination Schematic. A schematic illustrating the impact of applied strain on the initial delamination and buckling of a film, followed by strain localizing towards its center until a minimum R/h is reached. Beyond this point, additional strain causes the folded film to delaminate from the substrate.

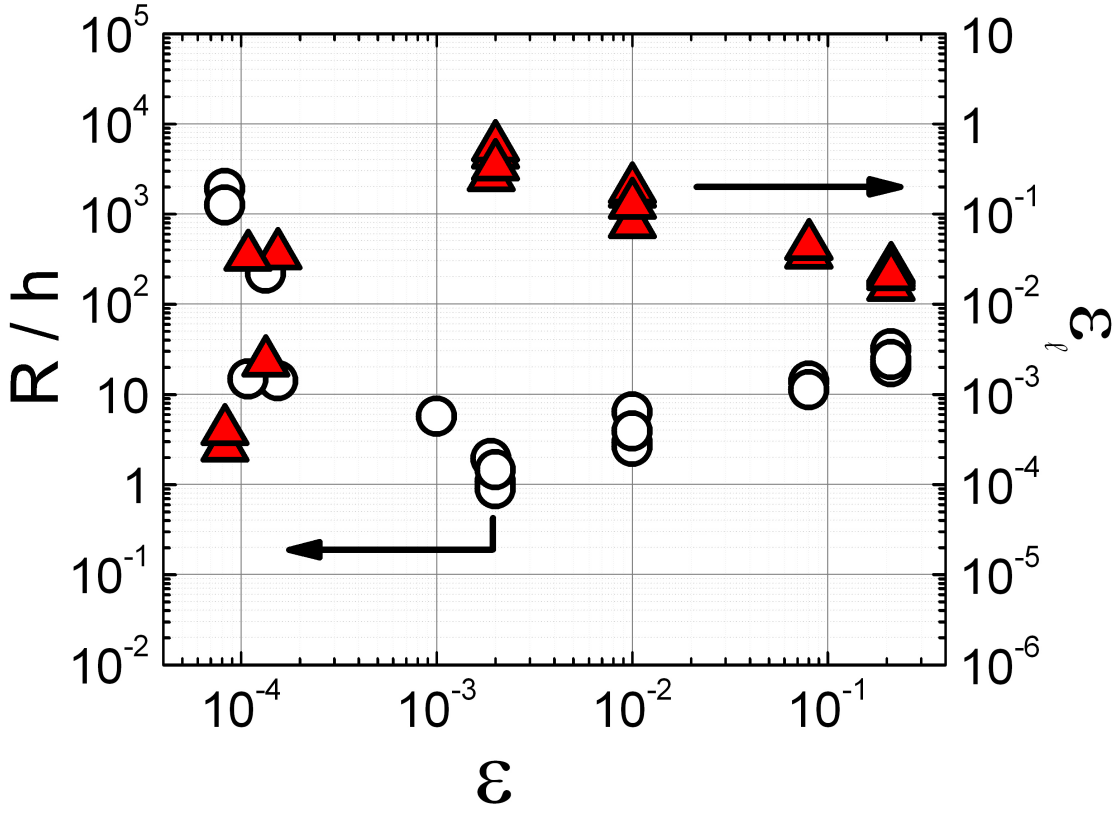

Figure 4.6: Radius of Curvature vs. Strain. A plot of the feature radius of curvature measured at the apex normalized by the film thickness, R/h, against applied strain (open circles). The strain localized at the center of the buckled, described by $\varepsilon_l = 2h/R$, is plotted as a function of macroscopic strain (closed triangles). Two regions of feature formation appear: strain localization (low strains up until a minimum $R/h \sim 1$), and delamination.

the buckle. The first region of figure 4.6 ($\varepsilon < 0.001$) illustrates the localization of applied macroscopic strain within the deformed structure. As strain continues to localize at the apex of the deformed region, eventually the film forms a sharp fold (Figure 4.7b). In the crossection of this deformation, the curvature is insignificant along the cantilever length, but increases sharply at the apex of the fold, where strain has been localized into a sharp ridge.

The ability for a film to localize applied strain increases structural stability and allows for rapid geometric movements via elastic instabilities [1, 31, 42]. It has been

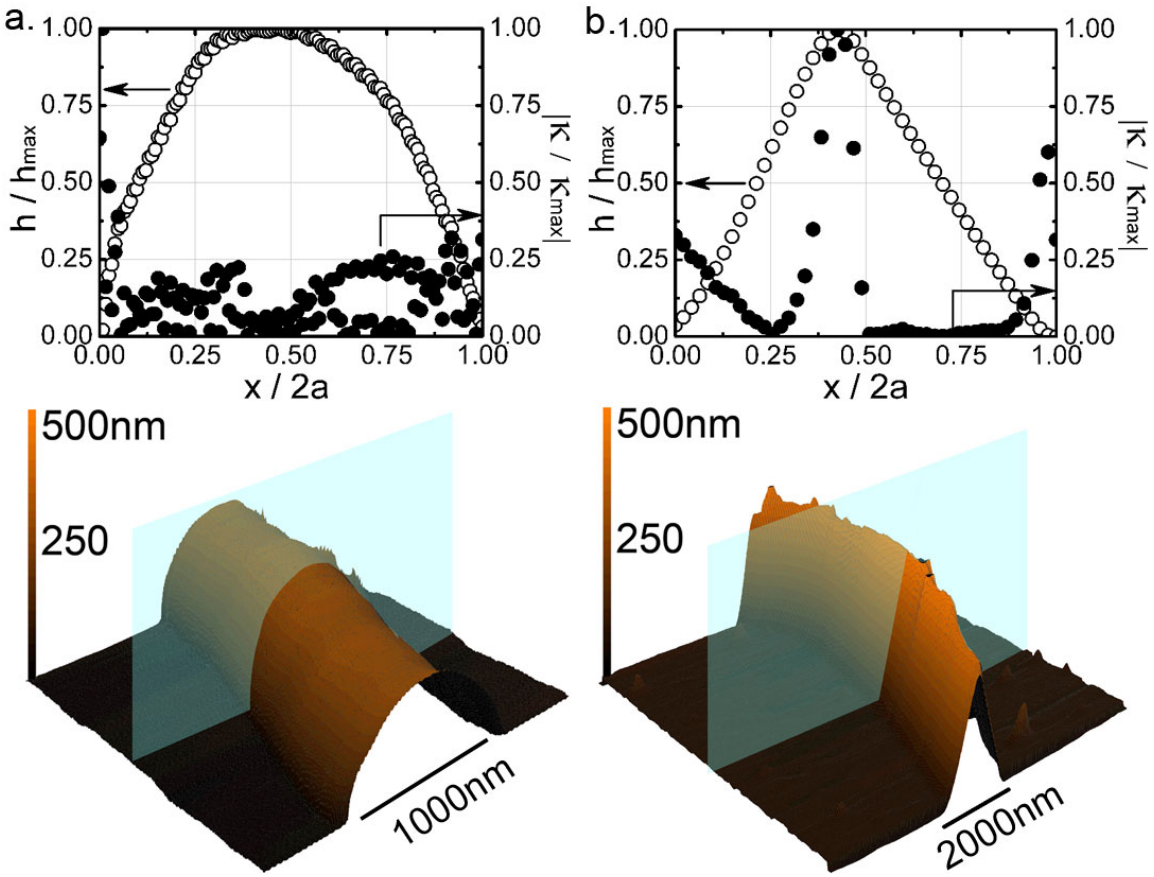

Figure 4.7: Bent and Folded PS Films. *a*. An AFM image of a bent polymer film with a crossection graph showing the normalized height and curvature across the buckle width. *b*. An AFM image of a folded polymer film with a crossection graph showing the normalized height and curvature across the buckle width.

previously demonstrated that thick, elastic films ($h \sim 10^{-6}m$) will geometrically localize compressive strains greater than the critical buckling strain to the center of the film. To describe the localization of strain within the bent polystyrene film we must compare the strain along the ridge of the deformed film to the strain that was macroscopically applied to the entire polymer sheet. The localized bending strain of a deformed structure can be described as:

$$\varepsilon_l \sim z\frac{\delta^2 w}{\delta x^2} \tag{4.19}$$

where z is the displacement from the midplane of the structure, and h is the vertical displacement (Figure 4.8). From this, we note that the strain at the outer edge of the feature is given as:

$$\varepsilon_l \sim \frac{h}{2R} \tag{4.20}$$

The measured values of strain localized at the apex of the delaminated features, ε_l,

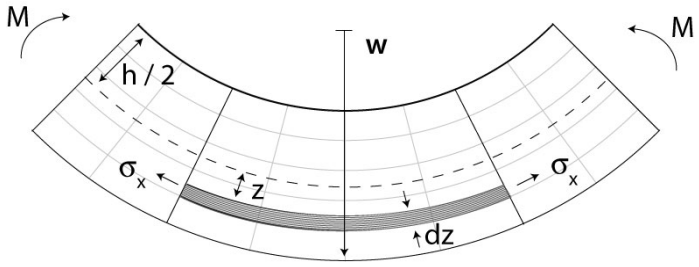

Figure 4.8: Radius of Curvature Schematic. A schematic of a beam of thickness h bent to a displacement w, depicting the curvature $\kappa = -\delta^2 w/\delta x^2$.

are plotted as a function of applied strain as closed triangles in figure 4.6. The apex of the PS films accommodate strains upwards of 50%, far exceeding typical polystyrene failure strains, which are generally less than 2% in tension or compression [65] and less than 1% in bending [66].

4.4.2 Thickness Dependence

One of the important considerations for the delaminated structures was the impact of film thickness on feature curvature. We were able to attain radii of curvature on the order of $10nm$, which is on the order with the radius of gyration for a polystyrene homopolymer. Due to potential AFM tip convolution, these radii values represent an upper limit for the curvature of the buckled films. However, the feature shape has no dependence on film thickness within the regime we studied (Figure 4.9), and could be the result of the unannealed polymer films having a residual stress from preparation.

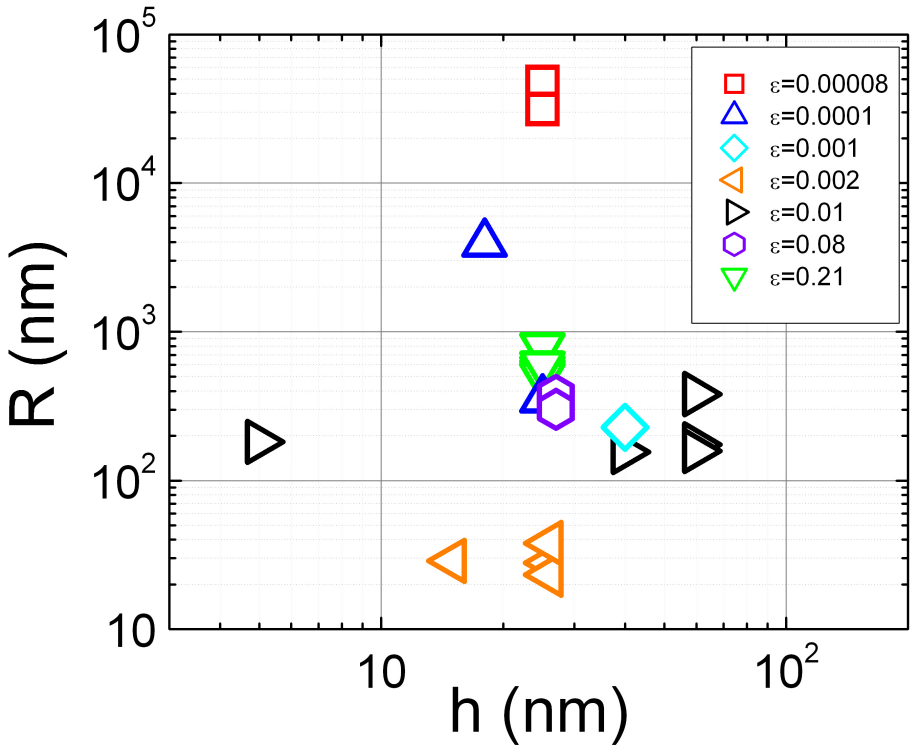

Figure 4.9: Thickness Dependence. A plot illustrating the independence of feature radius of curvature, R, on film thickness, h. This suggests that the curvature of the features is dicated more by the applied strain.

4.4.3 Delamination

Film delamination plays an important role at two different parts during the formation of these structures. Once the film is placed onto the strained substrate (Figure 4.3), initial delaminations form due to defects in the film and substrate [67]. The smallest debonded size of a film that will result in buckle formation in a film with a residual compressive stress, σ_m, is [67]:

$$a_m = \frac{\pi h}{2}\sqrt{\frac{\bar{E}}{3\sigma_m}} \tag{4.21}$$

An AFM of the edge of a delaminated feature from a sample prepared at low strains ($\varepsilon \approx 10^{-4}$) is given in figure 4.10. The impact of these edges on the curvature of

delaminated features is not known, therefore all measurements were made far from the feature's edges.

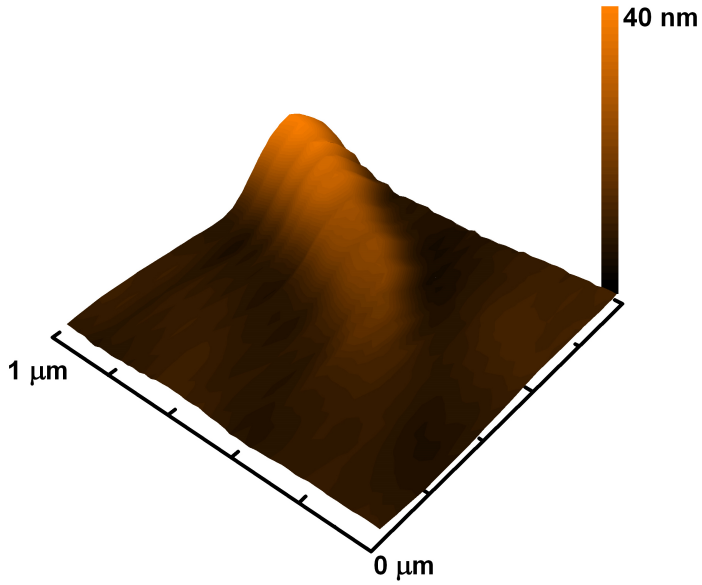

Figure 4.10: AFM of the Beginning of a Fold. An AFM image at the start of a film delaminating from a substrate.

The second region from the plot of R/h vs ε ($\varepsilon > 0.001$) describes the delamination of the strain localized feature (Figure 4.6). The sharpness of the folded features appears to reach a minimum at $R/h \sim 1$, beyond this point the radius of curvature of the delaminated features begins to increase, most likely due the limitations of the experiment than the material properties of the film. At this point the energetic cost for bending becomes greater than the energy to delaminate at the edges. Once this minimum radius of curvature is reached, additional macroscopically applied strain is not alleviated via buckling, and therefore increases the applied energy release rate between the film and the substrate, $G(a)$,. For any material system, the delamination resistance of the interface is chacterized by a fracture energy $\Gamma(\psi)$ per unit area, which depends on the phase angle ψ of the stress state acting at the edge of the delamination front [67]. Once the applied energy release rate is greater than or equal to the fracture resistance of the surface the delamination front will advance. This delamination can

be observed experimentally by measuring the buckle width, a, as a function of applied strain, ε, once $R/h \sim 1$. Figure 4.11 illustrates the increase in a for greater applied strains.

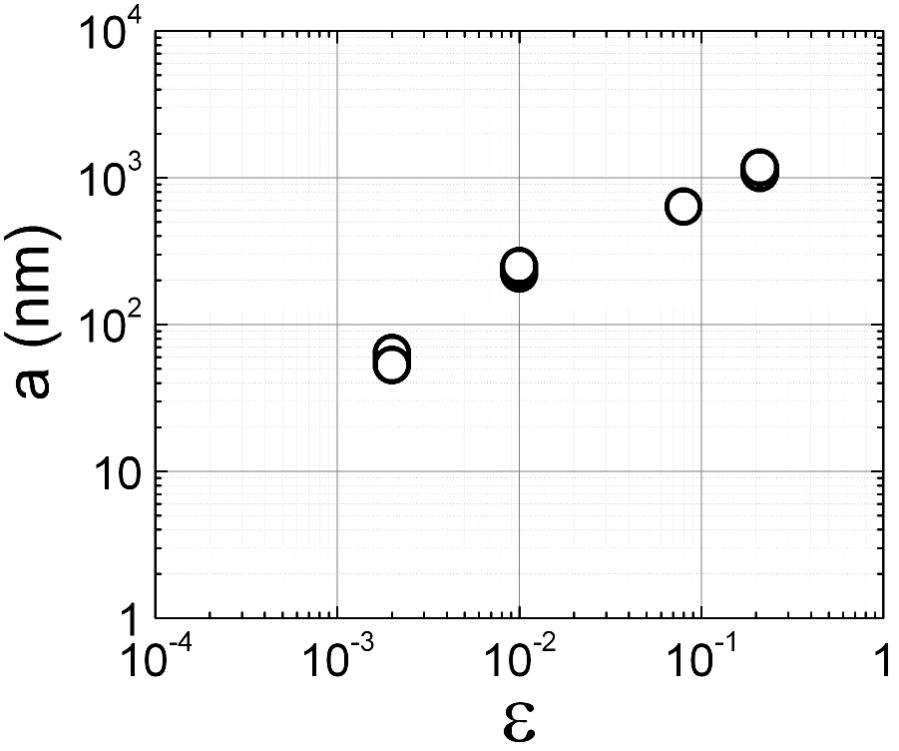

Figure 4.11: Buckle Width vs. Film Thickness. The second region of figure 4.6 is described by film delamination, this graph illustrates the increase in buckle width, a, for increasing applied strain, ε

4.4.3.1 High-Strain Deformations

While most of the work discussed in this chapter focused on low uniaxial strains to generate delamination and folding, the application of high uniaxial strain ($\varepsilon \approx 0.25$) caused the formation of delaminations on multiple length scales. From AFM analysis, delaminations with a consistent wavelength appear perpendicular to the applied uniaxial compressive strain (Figure 4.12-upper inset). Secondary delaminations are also observed forming with a random orientation and a large buckle width, $a \approx 1\mu m$

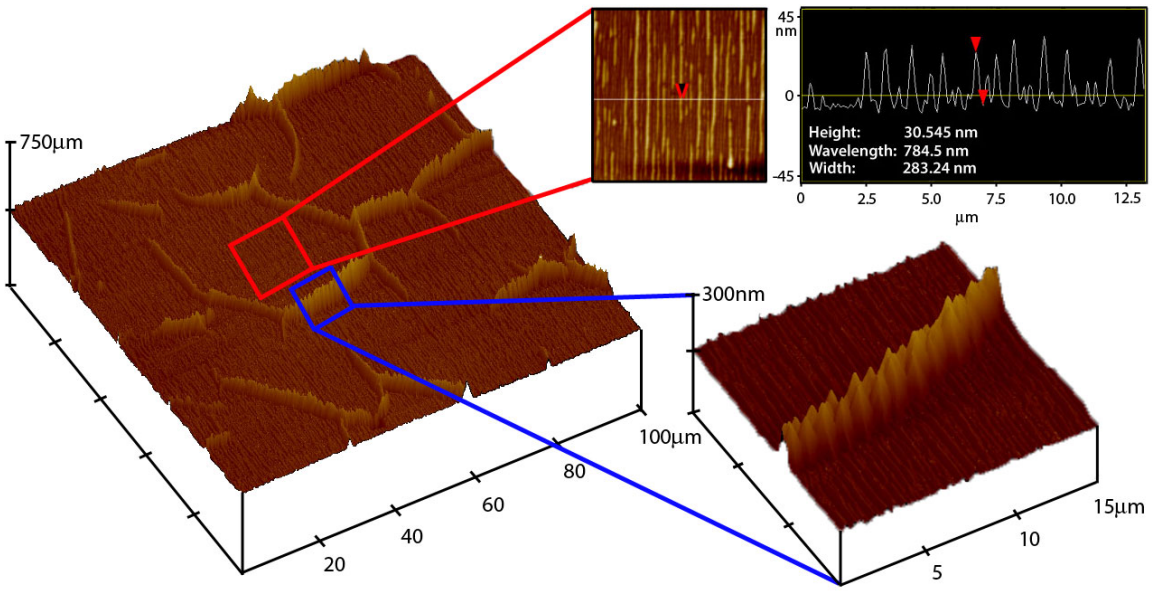

Figure 4.12: High-Strain Deformations. An AFM image of a highly strained ($\varepsilon \approx 0.25$) PS film exhibiting delaminated regions of two distinct length scales, highlighted in the figure insets.

(Figure 4.12-lower inset). These randomly oriented features are most likely caused by the additional transverse strain due to a Poisson's contraction.

4.5 Summary

The sharpness ratio of the features achieved on the polystyrene films (figure 4.7b) is near unity for adequately high uniaxial compressive strains. The film thickness of the polystyrene films presented in this chapter are on the order of the material length scale, with $\gamma/E \sim 10^{-10}$, leading to the fabrication of sharply folded nanostructures. While the width of these structures vary from tens to hundreds of nanometers, their lengths are typically several hundred microns to many millimeters. In this chapter, we present scaling relationships to predict the sharpness of deformed features, ranging from macroscopic to nanoscopic. The folding of ultrathin films in confined geometries will provide insight to the material's properties, as well as insight into controlling the next generation of nanoscale feature morphology and structure.

4.6 Open Questions

The work in this chapter focused on the film properties and geometry after buckling. Many interesting questions remain regarding the polymer chain configurations in the buckled regions of films with thicknesses on the order of the polymer's radius of gyration. This will require careful annealing and characterization, but will provide insight into how these films accommodate such high strains at their apex. It will also be important to quantify and control the film delamination. Controlling the initial delaminations will be crucial for nanoscale pattering, while understanding the balance between energy release rate and interfacial strength will be important for determing feature stability and ultimate failure. Developing an understanding of how homopolymer films delaminate and buckle will naturally lead to the study of more complex films, including block copolymer films and films with embedded nanoparticles. How these complex films accommodate strain both macroscopically and on the polymer chain length scale will have a broad impact fundamentally and in designing advanced materials.

4.7 Acknowledgements

We thank Andrew Davis who was the NSF-REU who assisted in performing experiments and characterization of the thin films. We also acknowledge NSF-MRSEC Central Facilities for use of the SEM.

CHAPTER 5

DRAPING FILMS: A WRINKLE TO FOLD TRANSITION

5.1 Introduction

The wrinkling of soft films commonly exhibits itself in nature in examples ranging from draping fabrics to wrinkled skin. This phenomenon occurs because elastic films bend more easily than they stretch, allowing them to buckle out of plane into wrinkles under applied strain [46]. While wrinkles are smooth undulations that distribute strain evenly, folds are sharp strain localizations of applied strain. The terminology of wrinkles and folds are often used interchangeably, but their differences have a profound impact on properties of the deformed media. For a crumpled sheet of paper, a network of folds, not wrinkles, develops and focuses energy in a manner that significantly increases the stiffness of the deformed material [22]. In biology, the process of folding is critical to morphogenesis, defining such features as the neural folds in early embryonic development. Wrinkling and folding have garnered much interest recently in patterning [47, 68, 69], functional materials [70, 71], draping [72], crumpling [38, 41, 73] and snapping [1, 42], but a fundamental understanding of the relation between the two structures is lacking.

In a recent paper, Pocivavsek and Cerda [44] demonstrated the transition from wrinkling to folding under simple uniaxial compression. This demonstration provides great insight, but boundary conditions and geometry can strongly affect the observed mechanism in the context of an elastic instability. In this chapter, we examine the wrinkle to fold transition under axisymmetric conditions, which are commonly found in nature, from cell morphology to the ciliary body of the eye. We will study the

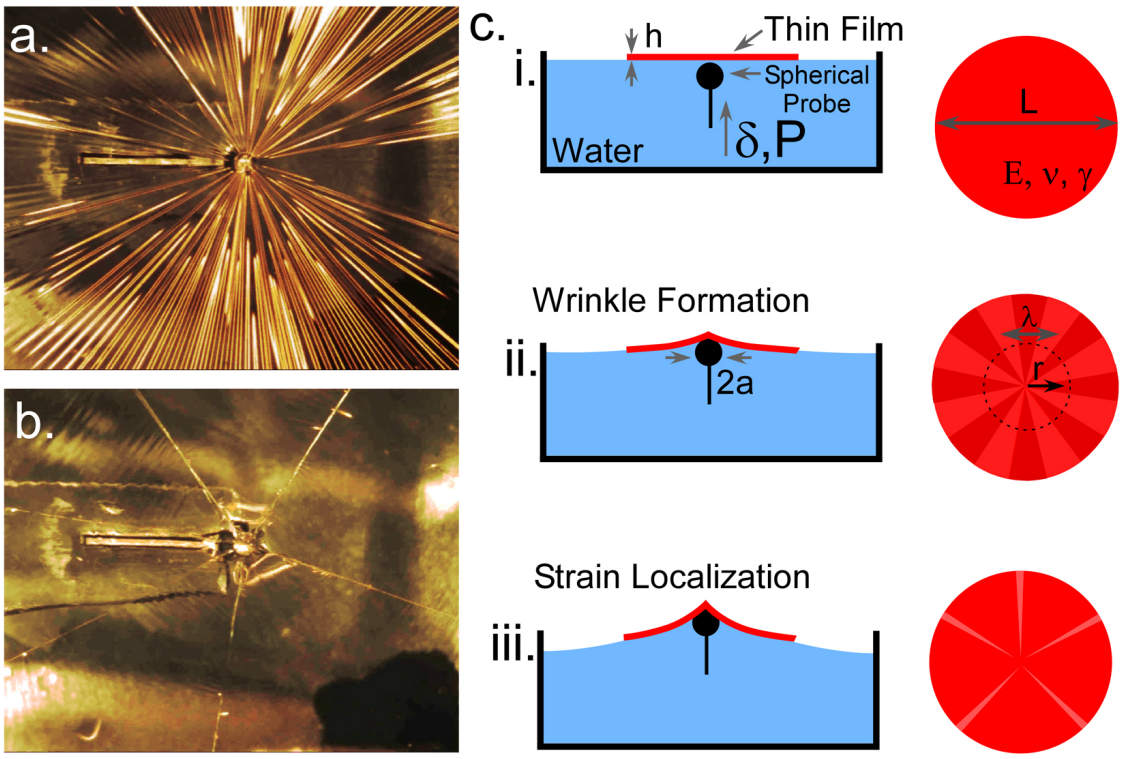

Figure 5.1: Draping Film Schematic. *a*. Wrinkles on a thin film floating on water being lifted by a spherical probe. *b*. As the veritical displacement of the probe increases the wrinkles strain localize into sharp folds. *c*. A schematic of the experimental setup where *i*. depicts the axisymmetric thin film floating on water, *ii*. as the spherical probe displaces in the z-direction wrinkles form on the surface, *iii*. and above a critical displacement the wrinkles collapse into folds.

wavelength and wavenumber of the wrinkles that initially form, and we will demonstrate that while folds localize strain and lead to a global minimization of energy, the redistribution of stresses can alter nearby morphologies.

5.2 Wrinkling

When a strain, ε, is applied to a thin elastic sheet of thickness h with a Young's modulus E and Poisson's ratio ν, the sheet remains flat while $\varepsilon < \varepsilon_c$, a critical strain. An increase in strain above ε_c causes the sheet to buckle and bend out of plane into wrinkles. The wavelength and amplitude are determined by the energy cost for

bending, U_B, and stretching, U_S. In the uniaxial sheet of length, L, and width, W, the total energy can be described as:

$$\mathscr{U} = U_B + U_S \tag{5.1}$$

where the bending and stretching energies are given as:

$$U_B = \frac{1}{2}\int_A D\left(\frac{\partial^2 w}{\partial y^2}\right)^2 dA \tag{5.2a}$$

$$U_S = \frac{1}{2}\int_A T(x)\left(\frac{\partial^2 w}{\partial x^2}\right)^2 dA \tag{5.2b}$$

where w is the out-of-plane displacement, and $T(x)$ is the tension along the x direction [46]. The stretching energy is analogous to the energy in an elastic foundation supporting a thin sheet [56]:

$$U_F = \frac{1}{2}\int_A K w^2 dA \tag{5.3}$$

where K represents the resistance to stretching. Therefore, the stretching resistance to the sheet is determined by comparing equations 5.2b and 5.3, which yields $K \sim T/L^2$ [46]. By assuming a smooth sinusoidal deformation in the thin sheet we note that the energetic cost in bending is high for wrinkles with short wavelengths. The total energy also increases with long wavelengths from the strain required to stretch the sheet longitudinally [46]. From the assumption of the wrinkle's sinusoidal geometry, the bending and stretching energies will scale as [44]:

$$U_B \sim DL\left(\frac{A}{\lambda^2}\right)^2 \tag{5.4a}$$

$$U_S \sim KLA^2 \tag{5.4b}$$

where A and λ are the wrinkle amplitude and wavelength, respectively. A balance of these two energies leads to a wrinkle wavelength which scales as [44, 46]:

$$\lambda \sim \left(\frac{D}{K}\right)^{1/4} \tag{5.5}$$

5.3 Experimental Approach

To quantify this wrinkle-to-fold transition in terms of both force and displacement, we use the simple act of lifting an elastic sheet from the surface of water (Figure 5.1a&b). The strain imposed by the point of contact and the underlying substrate causes the film to drape and wrinkle radially once above a critical strain. As the film continues to be lifted above the initial horizon of the water, the stress in the sheet focuses and the wrinkles collapse into discrete folds. For these experiments, a thin polymer film, either polydimethylsiloxane (PDMS) (Sylgard 184^{TM}) or polystyrene (PS) (Aldrich), is prepared via spin-coating a polymer solution onto a clean silicon wafer. A film of radius L is floated off the wafer onto the surface of water. A nanopositioner is used to lift a spherical probe of radius a into contact with the center of the film while a load cell records the force, P, of deforming the film (Figure 5.1c).

5.4 Results & Discussion

A typical response of the number of wrinkles, N, as a function of vertical probe displacement is given in figure 5.2. There are several notable regimes in this plot. At very low displacements, no wrinkling is observed (Figure 5.2a - $\delta < 500\mu m$), followed by the formation of wrinkles with a constant wavelength (Figure 5.2b - $500\mu m < \delta < 1300\mu m$). At this point, a wrinkle-to-fold transition occurs (Figure 5.2c). The onset of the initial fold causes the wavenumber of the remaining wrinkles to increase as a function of displacement (Figure 5.2d - $1300\mu m < \delta < 2500\mu m$). The wavenumber

begins to significantly decrease as additional folds form on the film (Figure 5.2d-f - $2500\mu m < \delta < 3000\mu m$), followed by the final fold formation (Figure 5.2g). To understand these regimes we will focus on the axisymmetric wrinkle wavelength, the wrinkle-to-fold transition, the impact of folding on the remaining wrinkle wavelength, and the final number of folds to form on the film.

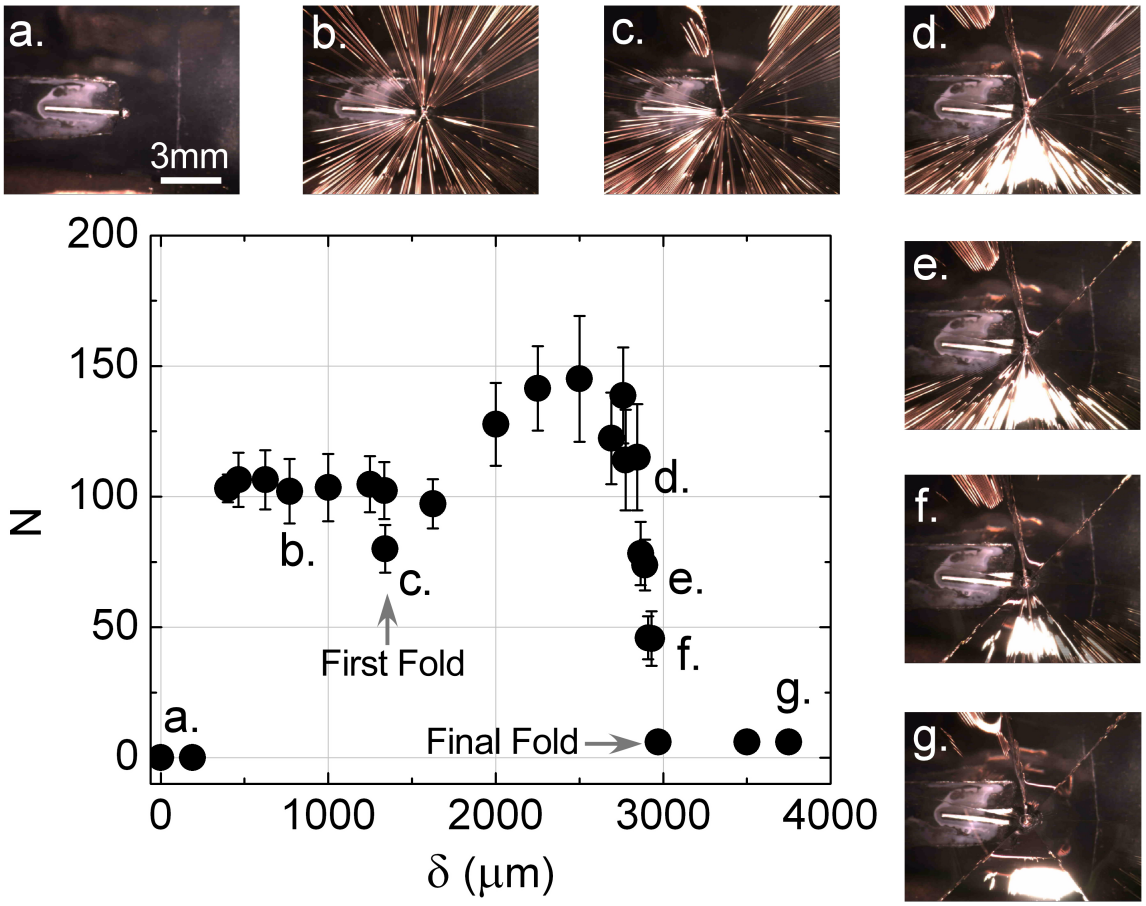

Figure 5.2: Wavenumber vs Displacement. A typical plot of the wavenumber, N, versus displacement, δ, along with optical microscopy images of wrinkles for a film thickness of $h = 112nm$. This graph illustrates several regions: at low displacements no wrinkling is observed, followed by the formation of wrinkles with a consistent wavenumber. The formation of a fold causes the wrinkle wavenumber to increase before the remaining wrinkles collapse into a finite number of folds.

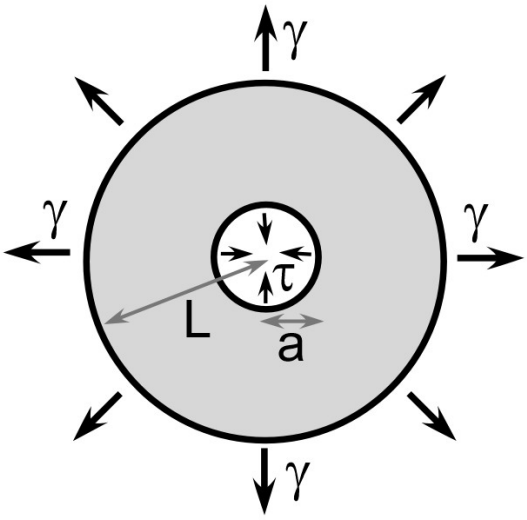

Figure 5.3: Airy's Stress Function - Biaxial. A schematic of two opposing stresses coming from the biaxial strain imposed by the spherical probe, τ, and the surface tension, γ.

5.4.1 Axisymmetric Wrinkling

In the previous section we presented the wrinkle wavelength scaling under unixial stress conditions. In an axisymmetric geometry, the effective substrate stiffness scales as the radial stress in the film, such that [39, 48, 74],:

$$\lambda \sim \left(\frac{D}{\sigma_{rr}}\right)^{1/4} \tag{5.6}$$

where σ_{rr} is the biaxial stress that develops in the thin film upon lifting. Similarly, a stress in the azimuthal direction develops, given as $\sigma_{\theta\theta}$. To determine these stresses we will consider the Airy's stress function for stresses acting biaxially upon the inner and outer perimeter of a disc (Figure 5.3). From table 5.1 we know that the stress function will be:

$$\mho = Br^2 + C\log r \tag{5.7}$$

The stress acting in the radial direction is the second derivative of $\mho$ with respect to r:

$$\sigma_{rr} = \frac{\partial^2 \mho}{\partial r^2} = 2B + \frac{C}{r^2} \tag{5.8}$$

Table 5.1: Airy's Stress Function Boundary Conditions

Airy's Stress Function						
$\mho$	σ_{rr}	$\sigma_{r\theta}$	$\sigma_{\theta\theta}$	$2\mu u_r$	$2\mu u_\theta$	**Description**
1	0	0	0	0	0	Trivial
r^2	2	0	2	$(k-1)r$	0	Biaxial tension
$\log r$	$1/r^2$	0	$-1/r^2$	$-1/r$	0	Center tension
$r^2 \log r$	$2\log r + 1$	0	$2\log r + 3$	$(k-1)r\log r - r$	$(k+1)r\theta$	Dislocation

where B and C are constants. From figure 5.3 we can take the stress conditions at the boundaries $r = L$ and $r = a$ to be $-\gamma$ and $-\tau$, respectively:

$$\sigma_{rr}|_{r=L} = -\gamma = 2B + \frac{C}{L^2} \tag{5.9a}$$

$$\sigma_{rr}|_{r=a} = -\tau = 2B + \frac{C}{a^2} \tag{5.9b}$$

By solving these two equations and two unknowns we can solve for σ_{rr} as:

$$\sigma_{rr}^w = \frac{a^2L^2(\tau-\gamma)}{r^2(a^2-L^2)} - \frac{a^2\tau - L^2\gamma}{a^2-L^2} \tag{5.10}$$

Similarly, from the stress function $\sigma_{\theta\theta}$ is given as:

$$\sigma_{\theta\theta} = 2B - \frac{C}{r^2} \tag{5.11}$$

therefore $\sigma_{\theta\theta}$ can be solved as:

$$\sigma_{\theta\theta}^w = \frac{a^2L^2(-\tau+\gamma)}{r^2(a^2-L^2)} - \frac{a^2\tau + L^2\gamma}{a^2-L^2} \tag{5.12}$$

For our experiment, $\tau \sim E(\delta/r)^2$ and $\gamma = \Gamma/h$, where Γ is the surface tension of water. By relating the scaling predictions from Cerda and Mahadevan [46] into a

radial geometry [39, 48, 74], the wavelength scales as:

$$\lambda \sim C_\lambda \left(\frac{\bar{E} h^2}{\sigma_{rr}} \right)^{1/4} r^{1/2} \tag{5.13}$$

Using equation 5.10, and considering a/L to be small, σ_{rr} becomes:

$$\sigma_{rr} \sim -\frac{\Gamma}{h} \left[1 - \left(\frac{a}{r} \right)^2 \left(1 - \frac{\tau h}{\Gamma} \right) \right] \tag{5.14}$$

Therefore, the total number of wrinkles, $N \equiv 2\pi r/\lambda$ will be approximately

$$N \sim C_N \left(\frac{L^2 \Gamma}{E} \right)^{1/4} h^{-3/4} \tag{5.15}$$

where C_N is a constant determined by the material properties of the elastic sheet. The wrinkle wavenumber for PS and PDMS films with thicknesses ranging from $h = 50nm$ to $h = 13.6\mu m$ were measured at $r = 3mm$ and $\delta = 1mm$. A plot of $N(E/L^2\Gamma)$ vs h from equation 5.15 is given in figure 5.4 where the dashed line represents a slope of $h^{-3/4}$ with an intercept of $C_N = 2$.

5.4.2 Wrinkle-to-Fold Transition

The number of wrinkles remains constant at low values of probe displacement (Figure 5.2), while the amplitude of the wrinkles increases with the increasing azimuthal strain, $\varepsilon_{\theta\theta} \sim (\delta/r)^2$. At a critical value of δ, the total energy of the deformed film is minimized through the collapse of several wrinkles into a fold, where strain is localized in a region of maximum curvature (Figure 5.2c). The decrease in total energy through the wrinkle-to-fold transition is recorded in the data of probe force, P, as a function of probe displacement, δ (Figure 5.5). P increases with δ as the film is deformed axisymmetrically until δ_c is reached. At $\delta = \delta_c$, an instantaneous decrease in P is recorded (Figure 5.5 inset), signifying a decrease in the total energy, which is proportional to $P\delta$.

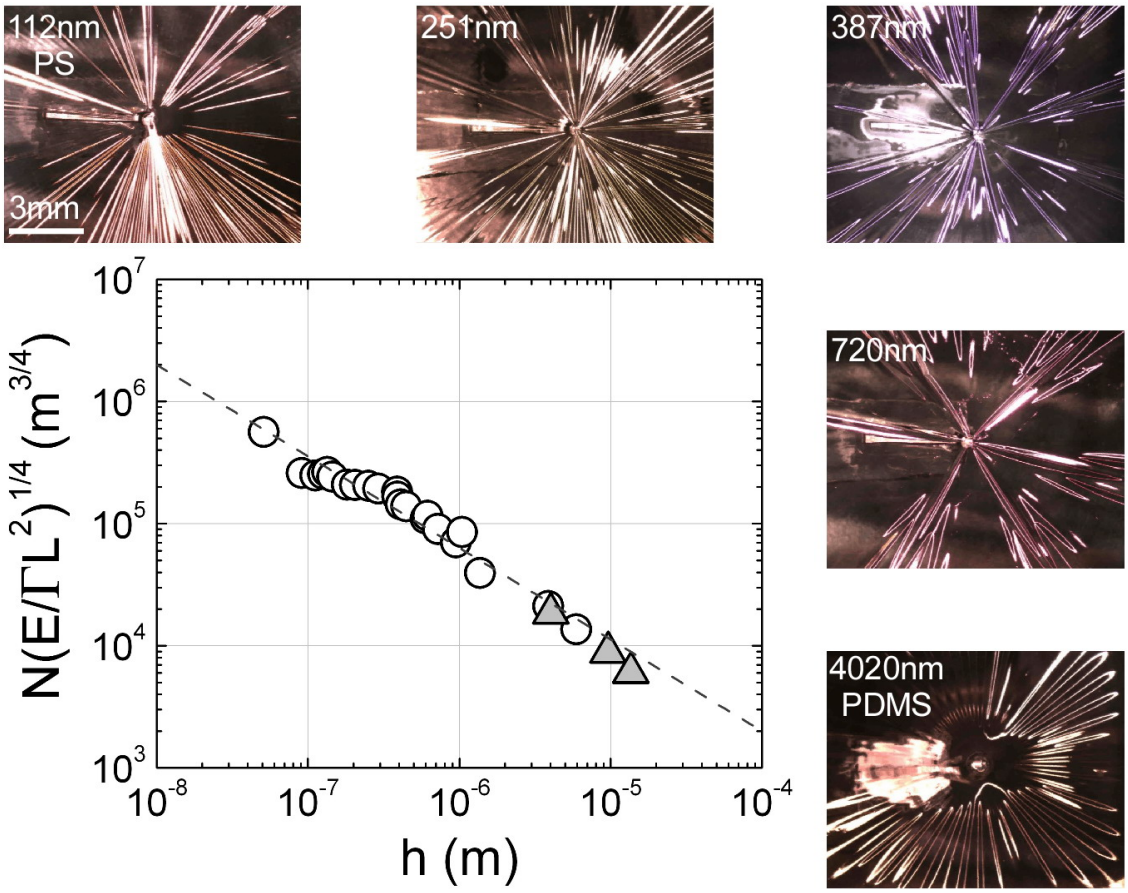

Figure 5.4: Wavenumber vs Thickness of a Draped Film. A plot of the wrinkle wavenumber, N, normalized by the film's material properties, $(E/L^2\Gamma)^{1/4}$ versus film thickness, h, at a fixed vertical displacement, $\delta = 1mm$ along with optical microscopy images of wrinkles. The dotted line represents a $h^{-3/4}$ scaling from equation 5.15.

Pocivavsek and Cerda [44] observed a wrinkle-to-fold transition at $\Delta/\lambda \sim 0.3$ for uniaxially compressed films. To compare to the axisymmetric case, we would expect the critical azimuthal strain at the wrinkle-to-fold transition to approximately equal:

$$\varepsilon_{\theta\theta} \sim \frac{\lambda}{3a} \tag{5.16}$$

This relation implies that the transition will be dictated by the state of compression at $r = a$, where the greatest stress and strain occurs at large values of δ. Therefore, the strain in the system will scale as [57]:

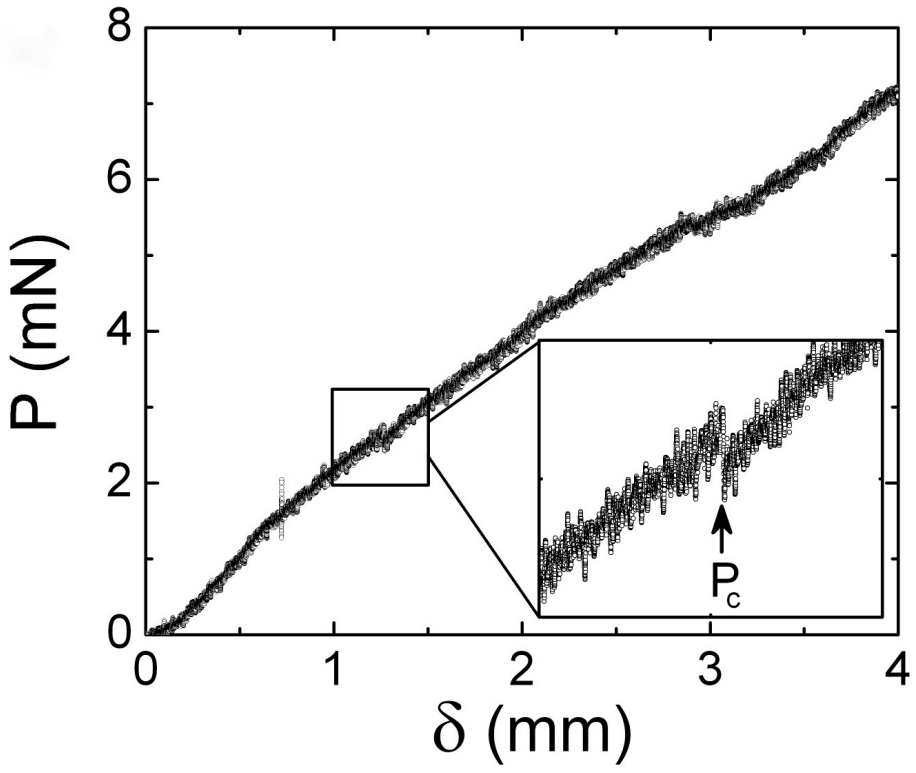

Figure 5.5: Force vs Displacement for Folding. a. A plot of force, P vs. displacement, δ for a 112nm thick PS film. The inset illustrates the critical stress for folding. b. A micrograph take at a displacement of 1.28mm, illustrating the fold formation at a critial load, P_c. c. A schematic of two opposing stresses coming from the biaxial strain imposed by the spherical probe, τ, and the surface tension, γ.

$$\varepsilon_{\theta\theta} \sim \left(\frac{\delta}{a}\right)^2 \tag{5.17}$$

At large displacements ($\delta \gg h$) we can assume that $\gamma/\tau \ll 1$ and $a/L \ll 1$, therefore σ_{rr} will scale as:

$$\sigma_{rr} \sim E\left(\frac{\delta}{a}\right)^2 \tag{5.18}$$

Accordingly, the critical δ for the wrinkle-to-fold transition should scale as:

$$\delta_c \sim \frac{2}{3} h^{3/10} a^{4/5} \tag{5.19}$$

From figure 5.5 we know that P scales linearly with δ, therefore we expect $P_c \sim h^{3/10}$ as well. These scalings are consistent with experiments (Figure 5.6).

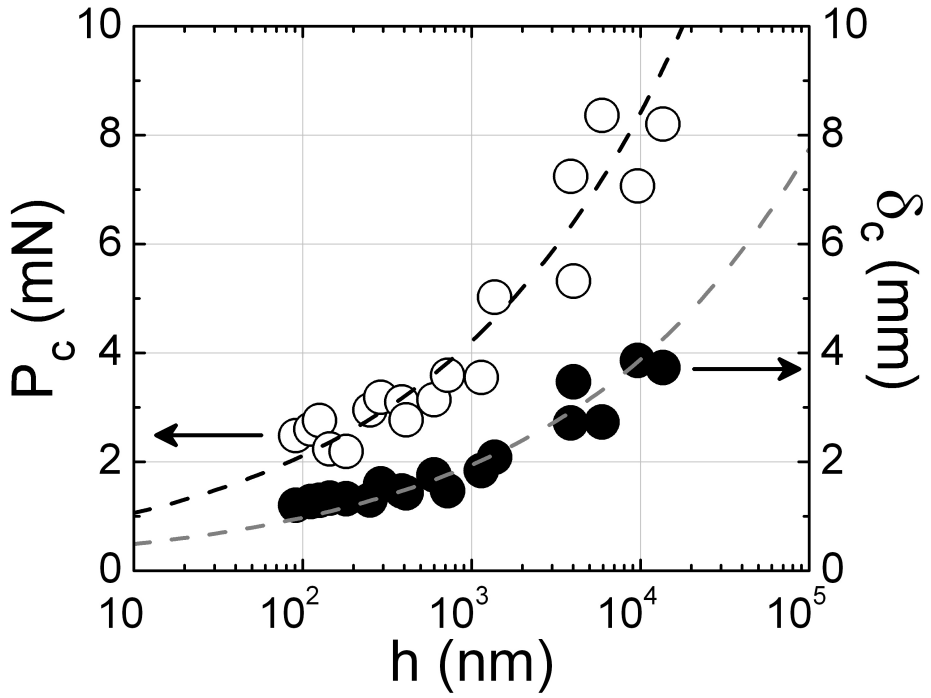

Figure 5.6: Critical load vs thickness. A plot of the critical force and critical displacement for the wrinkle to fold transition, P_c and δ_c versus the film thickness, h. The dashed lines represent a scaling of $h^{3/10}$.

5.4.3 Impact of a Fold on the Remaining Wrinkles

The strain localization from the onset of a fold changes the wrinkle wavelength of the remaining wrinkles on the film. Before folding, but after the initial onset of wrinkling, N remains at a constant value, independent of displacement, as predicted by equation 5.15. At δ_c, the onset of the wrinkle-to-fold transition, the wrinkle wavelength decreases. This decrease in the wrinkle wavelength is different than the wrinkle-to-fold transition under uniaxial deformations, where only the wrinkle amplitude decreases upon folding. Under axisymmetric conditions, the wrinkle wavelength decreases, thus implying that the radial stress increases in the surrounding material upon onset of strain localization. In many ways, this increase in stress is contrary to

conventional thought since strain localization is often associated with increasing the energy in only the folded region, and decreasing energy elsewhere. To understand this

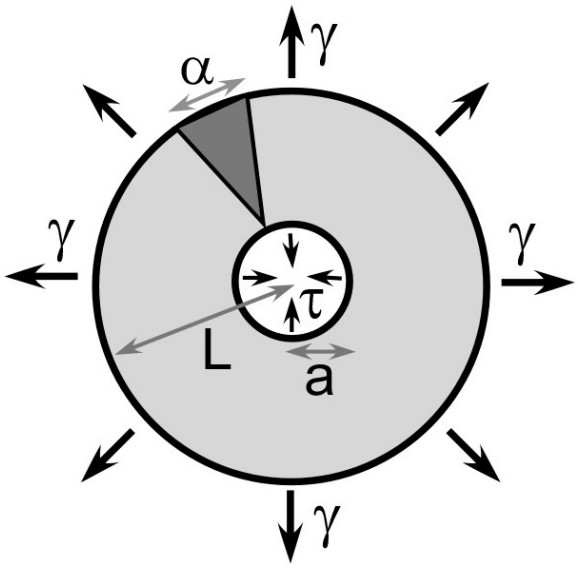

Figure 5.7: Airy's Stress Function - Disclination. A schematic of two opposing stresses coming from the biaxial strain imposed by the spherical probe, τ, and the surface tension, γ along with a disclination of length α.

decrease in wavelength, it is important to examine the impact of a fold on the stress field of the film. One way to do this is to treat the fold as a disclination of length α as depicted in figure 5.7. Considering a fold as a disclination within the elastic sheet adds an additional boundary condition of a discontinuity in displacement in the θ direction. Accounting for this condition, from table 5.1 we note that the stress function now becomes:

$$\mho = Ar^2 \log r + Br^2 + C \log r \tag{5.20}$$

therefore, the radial stress term becomes:

$$\sigma_{rr} = \frac{\partial^2 \mho}{\partial r^2} = A(2 \log r + 3) + 2B + \frac{C}{r^2} \tag{5.21}$$

Since the disclination appears in the θ direction, we can first solve for the constant A from:

$$\mho_\theta = \frac{A(\kappa+1)}{2\mu} r\theta \tag{5.22}$$

where $\kappa = 3 - 4\nu$ and $\mu = E/2(1+\nu)$. From figure 5.7, we can apply the boundary condition for when $\theta = 2\pi$:

$$\mho_\theta|_{\theta=2\pi} = \alpha r = \frac{A(\kappa+1)}{2\mu} r\theta \tag{5.23}$$

The remaining two boundary conditions for the radial stress are:

$$\sigma_{rr}|_{r=L} = -\gamma = \left[\frac{\mu\alpha}{(\kappa+1)\pi}(2\log L + 1) + 2B + \frac{C}{L^2}\right] \tag{5.24a}$$

$$\sigma_{rr}|_{r=a} = -\tau = \left[\frac{\mu\alpha}{(\kappa+1)\pi}(2\log a + 1) + 2B + \frac{C}{a^2}\right] \tag{5.24b}$$

Using these three boundary conditions, we can solve equation 5.21 for the radial stress of a film containing a fold as:

$$\sigma^f_{rr} = \sigma^w_{rr} + \bar{E}\alpha\left[\frac{L^2(r^2-a^2)}{r^2(a^2-L^2)}\log(L) + \frac{a^2(L^2+r^2)}{r^2(a^2-L^2)}\log(a) + \log(r)\right] \tag{5.25}$$

Similarly, the theta stresses can be determined by using the stress function:

$$\sigma_{rr} = \frac{\partial^2 \mho}{\partial r^2} = A(2\log r + 3) + 2B - \frac{C}{r^2} \tag{5.26}$$

Therefore, the theta stresses of the film are:

$$\sigma^f_{\theta\theta} = \sigma^w_{\theta\theta} + \bar{E}\alpha\left[\frac{L^2(r^2+a^2)}{r^2(a^2-L^2)}\log(L) - \frac{a^2(L^2+r^2)}{r^2(a^2-L^2)}\log(a) + \log(r) + 1\right] \tag{5.27}$$

Equation 5.25 dictates that σ^f_{rr} is always greater than σ^w_{rr}. Since the number of wrinkles, N scales as $N \sim (\sigma_{rr}/E)^{1/4}h^{-3/4}$, the presence of the fold, or the disclination in the previously axisymmetric film, will lead to a new number of wrinkles, N':

$$N' \sim N(\sigma^f_{rr}/\sigma^w_{rr})^{1/4} \tag{5.28}$$

such that $N' > N$ due to the increased stress in the region surrounding the fold. This increase in the number of wrinkles, demonstrated in figure 5.2, is an important consequence of axisymmetric boundary conditions. The process of strain localization, which lowers the global energy of a material system, can lead to regions of increased stress beyond the folded region itself. This impact on the surrounding stress field and associated deformation changes (i.e. λ decreases in the non-folded wrinkles) can impact the development of cells and the general morphology of the morphogenetic field.

5.4.4 Final Fold Formation

Further confinement in the film as the probe continues to rise after the wrinkle-to-fold transition eventually causes the remaining wrinkles to collapse into folds, as depicted in the optical microscopy images in figure 5.2. For a fixed probe size, the number of final folds appears independent of film thickness and material properties. A fixed number of folds, 5.5 ± 1.5, was observed for both PS and PDMS films across several orders of magnitude of film thickness (Figure 5.8)

5.5 Summary

In this chapter, we discussed the wrinkle-to-fold transition observed by lifting an elastic sheet from the surface of water. This confinement leads to stationary wrinkles with an a predictable scaling that collapse into folds above a critical load, dictated by the film thickness. Understanding the linear and nonlinear behavior of thin films confined to soft or fluid substrates provides critical insight towards their use in biological and synthetic soft material environments.

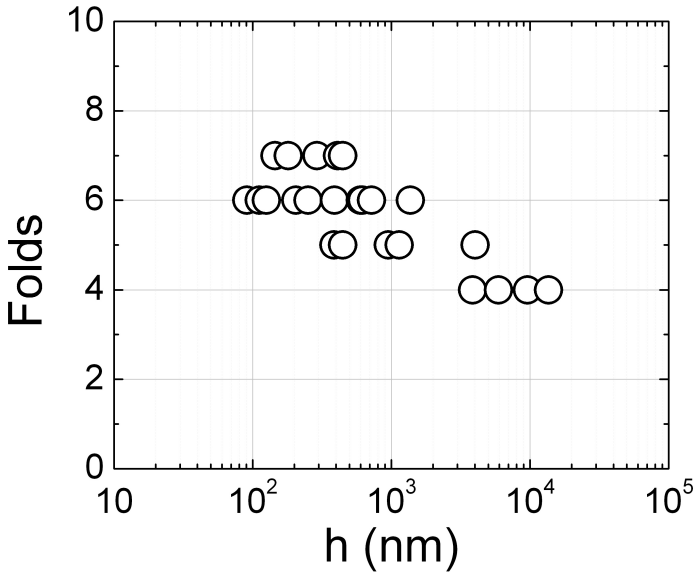

Figure 5.8: Folds vs Film Thickness. A plot of the final number of folds formed as a function of film thickness. The total number of folds using a fixed probe size appears to be approximately constant over several orders of magnitude.

5.6 Open Questions

Understanding the wrinkle-to-fold transition in thin membranes resting on soft or fluid substrates will have a broad impact within biomechanical systems. It is therefore necessary to study this transition under a variety of geometries and boundary conditions. In this chapter we focus on the wrinkling and folding of axisymmetric films. To analyze the experimental results we made several assumptions to require further confirmation. A more detailed understanding of these assumptions, and the limits of them, will be important for making generalized predictions across many material systems. The assumption of a fold acting as a disclination leads to interesting predictions regarding varying states of stress in the film as well as the radial location of the onset of folding. Testing these these predictions will give further credence to the assumptions made in this work. To gain this general understanding, it will be important to study the impact of the initial geometric and experimental conditions (e.g. film radius, probe size, probe velocity) on the wrinkle wavenumber and final fold

formation. With a better understanding of this wrinkle-to-fold transition it will be of great interest to explore the impact of more complex films (e.g. block copolymers, embedded nanoparticles, thickness gradients) and substrates (e.g. hydrogels, varied surface tensions) on this folding process.

5.7 Acknowledgements

We would like to thank the National Science Foundation for funding this project. We would also like to acknowledge fruitful discussions between the authors and Narayanan Menon on the work presented in this chapter.

CHAPTER 6

CONCLUSIONS

This work focused on understanding deformation mechanisms and responsiveness associated with the wrinkling, folding, and snapping of thin polymer films. By taking advantage of elastic instabilities and geometric strain localization we were able to develop new strategies for responsive surfaces that will have a broad impact on adhesive, optical, and patterning applications. This work opens the door for a wide range of future studies ranging from the strongly applied to the fundamental.

Using lessons from the Venus flytrap, we designed biomimetic surfaces that dynamically modify their topography by snapping between two geometries. The timescale for this osmotically driven process scales with the square of the film thickness. There will be much interest in making responsive devices that are smaller and faster, and pushing the film thickness into the nanometer length scale will address these applications. This length scale will also foster interesting fundamental questions regarding the limits of this instability in polymer films as the film thickness approaches the length scale of a polymer chain. Utilizing the bifurcation of hemispherical shells for pattern formation and responsiveness also provides a wealth of questions regarding how the structures on these surfaces interact. The inherent coupling of the structures makes it possible to design surfaces that have a domino-like trigger, where each structure impacts the geometry of its nearest neighbors in a predictable way. These type of active systems will have a broad impact on everything from drug-delivery to antimicrobial devices.

The use of crumpling and snapping films in responsive surfaces creates a strong impetus to scale down the films to sub-micron thicknesses. Therefore, it is important to understand how these films will behave and accomodate large elastic instabilities. The deformation and buckling of ultrathin polymer films provided an interesting look at how films can localize their strain towards the center of the film, creating a sharp fold. The folding of thin films has a great fundamental importance since it is difficult to understand how films normally so brittle can accommodate such high strains. This strain accommodation will be even more fascinating when the polymer chain architecture is considered, when films as thin as the radius of gyration of the polymer are deformed and sharply folded. Similarly, we studied the wrinkle-to-fold transition observed in thin polymer films. By simply lifting an axisymmetric film from the surface of water we made scaling arguments regarding wrinkle wavelength and fold formation. Testing the assumptions made in developing these arguments will allow the work to be applied to broad, general problems, including the biomechanical impacts of thin membranes resting on soft or fluid substrates.

Understanding how thin polymer films respond to stress is of great importance for a variety of fields. The wrinkling, folding, and snapping observed here present just the beginning of understanding and utilizing elastic instabilities to provide rich industrial applications and probe deeply fundamental questions.

APPENDIX A

RESPONSIVE SURFACES

A.1 Introduction

A responsive surface is a surface or interface that can dynamically change its properties or shape in response to a specific trigger, or stimulus. These surfaces have a great potential for impacting a wide range of applications as they allow for the creation of dynamic devices. These applications range from release-on-command coatings [6] and adhesives [3–5,75], on-command frictional changes [34,35], instant modification of optical properties at an interface [7, 8], rapid response drug delivery [9–11], chemical sensing [12–14], and antimicrobial devices [76].

A.2 Responsive Systems in Nature

From evolutionary biology to the camouflage of an animal in the wild, nature has been using responsive systems for millions of years. Scientists have focused a lot of attention over the years on plants and animals that are able to quickly respond to environmental changes. The cuttlefish are among the most sophisticated invertebrates in the animal kingdom because their neurally controlled chromatophores allow the animal to instantly change its body patterning and imagery to blend with the surroundings [77, 78]. Some chameleon species have the ability to change their skin color as an expression of the physical and psychological condition of the lizard, though not in response to their surroundings. While the biological implications of these responsive systems are vast, there are similar responses observed in the plant kingdom that are determined by the geometric and materials properties of the object.

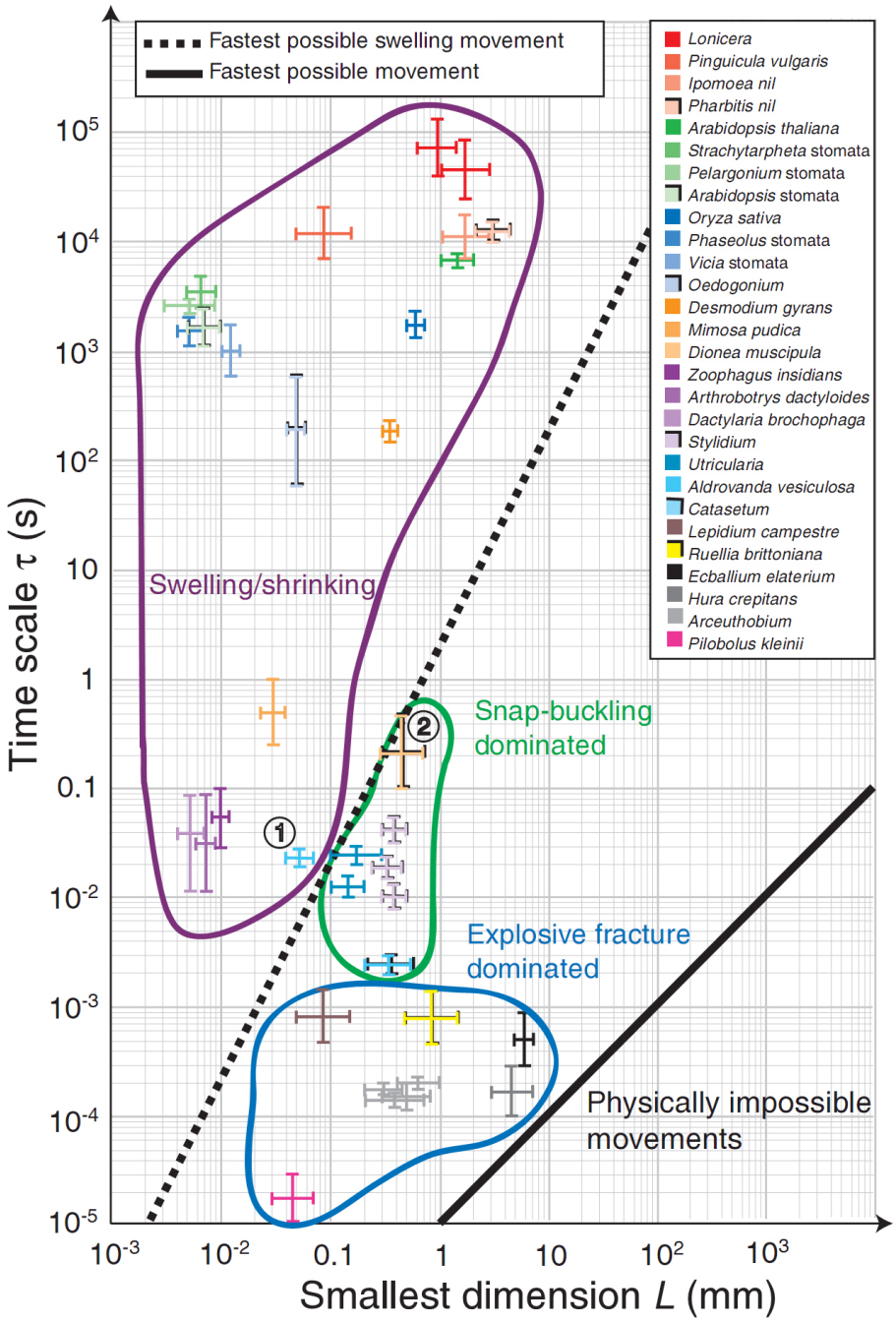

Figure A.1: Physical Limitations of Plant Movements. A Figure from Skotheim *et al.* illustrating the physical limitations of plant movements as a function of their smallest dimension [31]. The dashed line represents movements limited by the poroelastic timescale, while the solid line designates the speed of sound. The plant movements are broken up into three regions: swelling, snap-buckling, and explosive-fracture.

Plant movements are hardly thought of as rapid and responsive, but there are dozens of examples of plants' nastic, hydraulic movements for pollen emplacement, seed dispersal, nutrition, and defense. The carnivorous fungus *Dactylaria brochophaga* traps nematodes in less than $0.1s$ by swelling rapidly [79]. The flower stamens of the bunchberry dogwood use the storage and release of elastic energy to catapult pollen into the air as the flower explosively fractures [80]. The responsive mechanism of the Venus flytrap has captured the interest of scientists for centuries, and the closure of the Venus flytraps leaves has been attributed to a snap-through elastic instability [1]. These diverse, nonmuscular, hydraulic plant movements all use the storage or elastic energy as a way to respond to the environment around them. Skotheim et al. demonstrated the physical limitations of plant movements, breaking them into three categories: swelling, snap-through instability, and explosive fracture [2]. These movements scale with the materials properties and smallest length scale of the plant (Figure A.1). The swelling and shrinking of a plant occurs reversibly, but is limited by fluid transport, so it the slowest of these plant movements. Rapid plant movements that occur faster than the poroelastic time for swelling rely on elastic instabilities. While explosive fracture is the fastest possible movement of this type, it is not reversible. The rapid response of a snap-through elastic instability ($\Delta t < 0.1s$) and its reversibility make it a unique movement which will greatly impact the design of responsive materials.

A.3 Synthetic Responsive Systems

A.3.1 Bulk Property Change

Scientific advancements have consistently built upon inspirations from nature to create smart, responsive materials, [15,81–87], while not necessarily using mechanisms from the natural world. A smart material typically refers to a material with intrinsic sensing, actuating, and controlling capabilities in its microstructure [15]. Shape-memory materials are one of the major examples of smart composites because of

properties including the shape-memory effect, pseudo-elasticity, high damping capacity, and adaptive properties due to reversible phase transitions [15]. Shape-memory materials will exhibit a predetermined response after sensing a change in the environment around it, such as thermal, mechanical, magnetic, or electrical stimuli. This allows the tuning of materials properties like shape, adhesion, and friction in response to environmental changes. In one recent example, a polymer triple-shape material which changes between three equilibrium shapes based on the applied temperature can be seen in figure A.2 [16]. Although shape-memory materials offer unique advantages in a material's ability to change shape and property, the response time is typically on the order of several minutes to several hours.

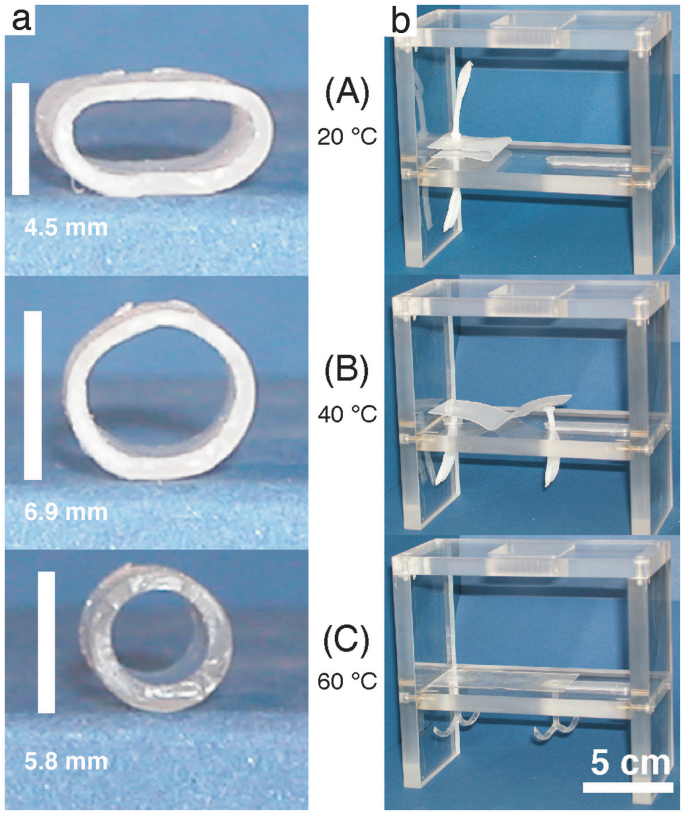

Figure A.2: Shape Memory Objects. A series of photographs illustrating the triple-shape effect of two different shape memory objects as the temperature of the system is varied. Figure was reproduced from Bellin *et al.* [16].

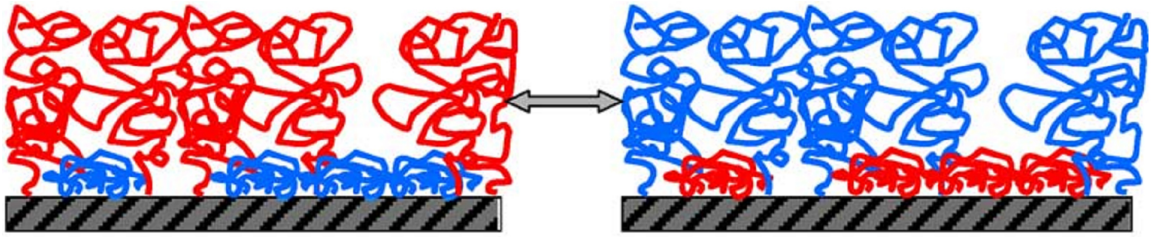

Figure A.3: Enviromentally Responsive Polymer Brushes. A schematic representation of grafted copolymers that can switch between two different surface morphologies. Figure was reproduced from Luzinov *et al.* [17].

A.3.2 Surface Property Change

A.3.2.1 Surface Functionalization

While much of the research for smart materials focuses on bulk material change, a great deal of work is currently being devoted to tuning the interface for specific applications, including wetting, adhesion, adsorption, and lubrication. This focus on the surface properties of a material has lead to the development of materials where the interfacial properties can be reversibly tuned in accordance with environmental stimuli [17]. Functionalization of the materials surface (e.g. polymer brushes) can lead to an environmentally responsive material where the interface responds to environmental changes, but the bulk remains unchanged. Environmentally responsive polymer brushes have been synthesized for applications such as permitting selective adhesion on a surface to allowing reversible switching of grafted chains to change optical properties (Figure A.3) [17]. This has been done at the surface-to-air interface [17], at an aqueous interface [88], and on colloidal particles [18]. The ability to graft optimal, responsive polymer chains on a surface for a particular application allows tunable, adaptable surface properties. A notable drawback of these environmentally responsive polymer brushes is their inability to change global surface properties over a fast time scale.

A.3.3 Geometry & Topography

Along with manipulating the surface chemistry of a material to achieve responsiveness, many research groups have worked on creating surface microstructures that can respond to stimuli. Microelectromechanical systems (MEMS) is one example of microstructures that can range from pressure sensors to optical switches [8, 89, 90]. Recent advances have been made in developing microlenses that can adapt to environmental conditions around them by changing focal length [7,8,83,91]. These responsive microlenses have found wide use in photonics, optical displays, and biomedical systems.

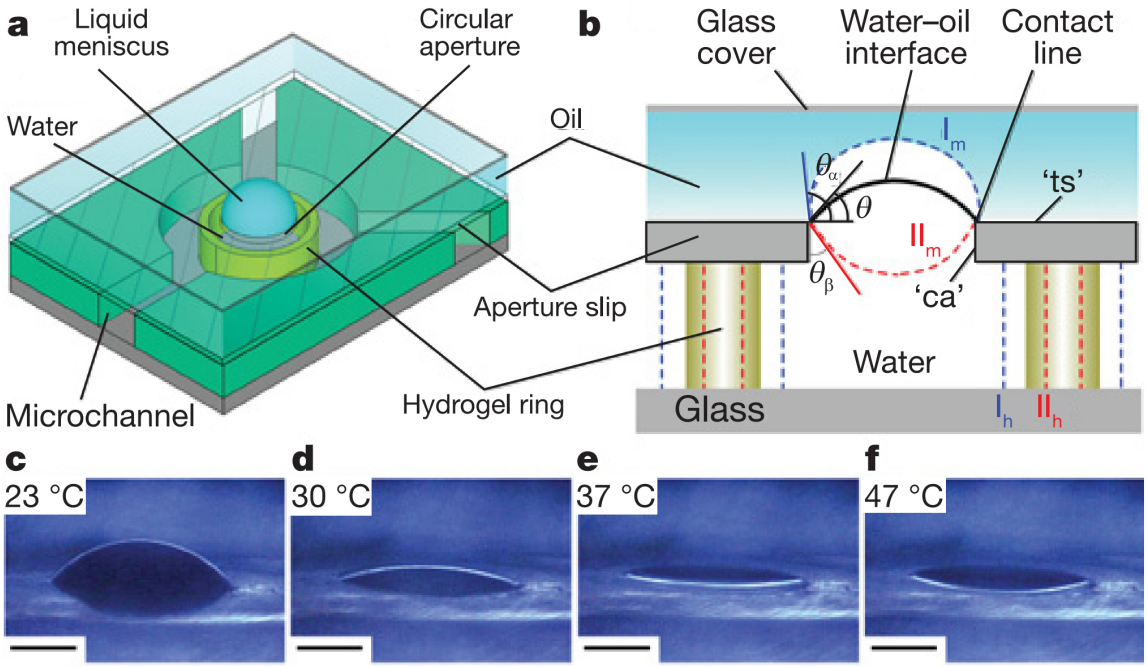

Figure A.4: MEMS Optical Switch. A schematic with photographs illustrating an adaptive microlens where the meniscus height and concavity at the water-oil interface can be varied via microfluidic channels. Figure was reproduced from Dong *et al.* [7].

Adaptable hydrogel microlenses have also been used in protein detection by monitoring the hydrogel swelling due to protein-ligand interactions [83]. This process is reversible and has been observed on small length scales (microlens radius: $2\mu m$), though the swelling process is not rapid. Microlenses with switchable concavity have been developed by working with the surface tension at a liquid-liquid pinned inter-

face [7]. In this example, the meniscus of an oil-water interface is used as an optical lens whose focal point can be changed from -8 to +8 (divergent and convergent) by changing the curvature of the meniscus (Figure A.4) with a stimuli-responsive hydrogel [7]. This process is reversible, but is limited in size (microlens radius: $1mm$), and timescale (tens of seconds).

APPENDIX B

ADHESION AND RELEASE MECHANISMS FOR NANOIMPRINT LITHOGRAPHY

B.1 Introduction

The ability to efficiently fabricate controlled geometric structures on material surfaces is important for numerous industries. Most directly, the development of this technology has been driven by the semiconductor industry for integrated-chip fabrication. Imprint lithography provides a simple and economical way to transfer nanoscale topographic features over large macroscopic areas via physical templating. Nanoimprint lithography (NIL) works to replicate patterns by mechanically deforming a polymer material using a hard mold with nanoscale features on it. This simple process has demonstrated the replication of features on the order of 10nm in a low cost and high throughput manner. The mechanical and surface properties unique to silicon-based polymers offer a material advantage in several aspects of imprint lithography, yet these same properties also challenge the use of these polymers for true nano-scale imprinting. One of the most common challenges with NIL is accurate pattern transfer from the template to the substrate. Defects generated during this pattern transfer process slow the replication process by requiring the template to be cleaned before imprinting can continue. Addressing this issue requires the development of optimized nanoimprinting materials. The objective of this project was to understand the effect of modulus on the release mechanism of various siloxanes provided by Dow-Corning by quantifying their modulus, their adhesion to an imprint material, and the effect of a pattern on the release mechanism. We investigated these issues using two custom-built instruments and our experience in adhesion characterization.

B.2 Experimental

B.2.1 Contact Adhesion

To determine the adhesion properties, we ran Johnson, Kendall, and Roberts-type (JKR) measurements on non-patterned surfaces. Specifically, we characterized cured, non-patterned surfaces of four siloxanes (Dow Corning formulations: AB, AC, W, and Z) and Sylgard 184 with an uncoated, fused silica probe. This experiment allowed us to determine the siloxane's cured modulus while also comparing the overall work of adhesion and interfacial energy release rate to an inorganic surface, similar to a surface used for templating imprinting "daughters". Each sample was cured at 70C for 18 hours at the crosslinker/prepolymer ratio recommended by Dow Corning. The crosshead displacement rate for all experiments was fixed at $0.86\mu m/s$, and each contact adhesion experiment was conducted three times for statistical confidence. The moduli data is presented in figure B.1

B.2.2 Smooth Nanoimprint Lithography

Using a custom built imprinter we performed *in situ* monitoring of the force and displacement history during the imprinting process (Figure B.2). To understand the basic release properties of each imprinted siloxane we first ran imprinting experiments on the five non-patterned siloxanes. With our current setup the siloxane template is connected to the inverted nanopositioner and load cell and the UV light source is located above the Norland optical lens to ensure that the volume of acrylate ($50nL$) and the intensity of light curing the acrylate sample during each experiment are kept constant (Figure B.4). Due to a tensile force that develops during the cure process (discussed below) it is important to keep the separation distance of the acrylate and the Norland lens fairly constant in order to prevent premature separation between the partially cured acrylate and the siloxane surface. We keep this distance constant by ensuring that our contact area and volume for each sample were kept constant. The force vs. time graphs for each imprinted, smooth siloxane surface are given in

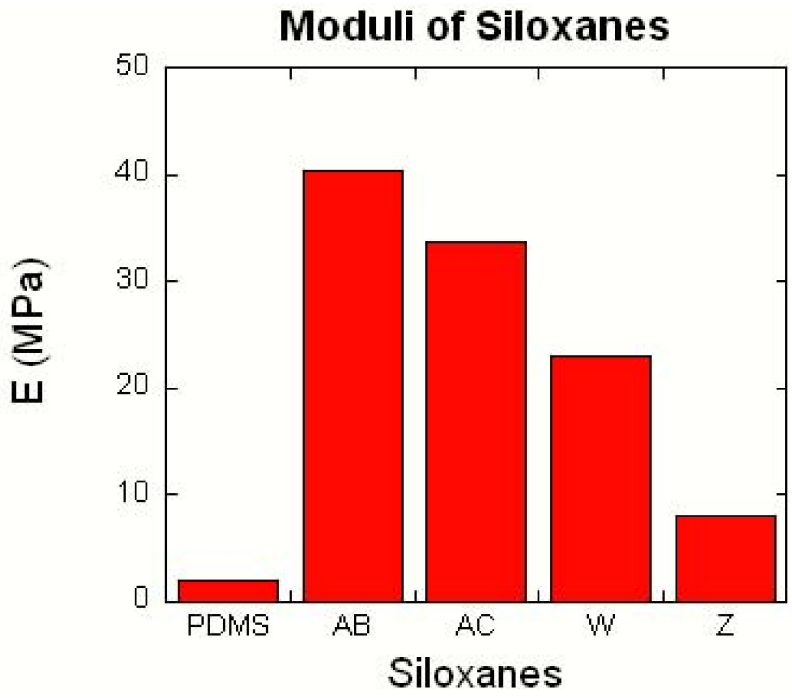

Figure B.1: Modulus of Siloxanes. A comparison of the siloxane moduli for samples of Sylgard 184^{TM} (PDMS), AB, AC, W, and Z measured via a contact adhesion test.

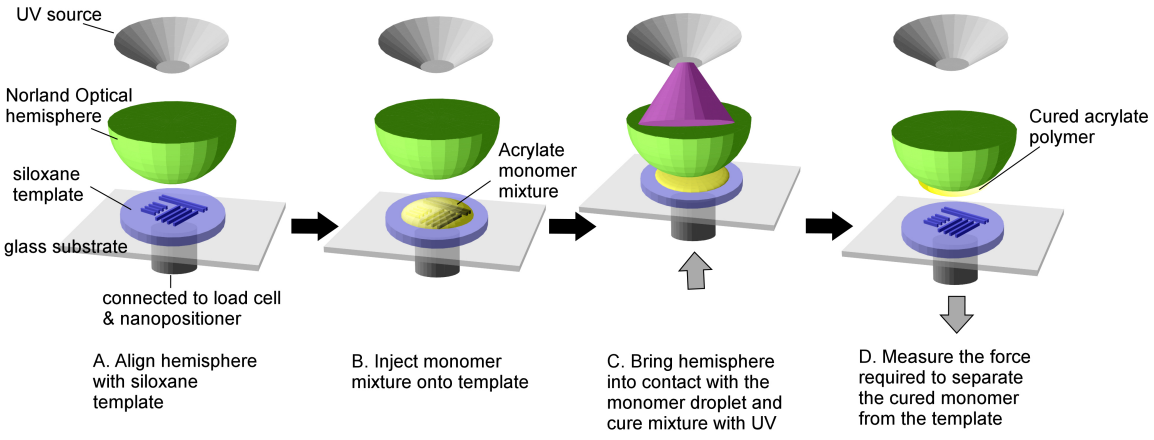

Figure B.2: Nanoimprint Lithography Schematic. A schematic of the experimental setup for running imprint lithography experiments. A droplet of a photocurable monomer is placed on the substrate and then brought into contact with the spherical probe. The monomer is crosslinked by UV light while a load cell measures the force during curing and separation.

figure B.3 with a comparison of the maximum force of separation (P_{max}) to the energy release rate (G_{sep}) for each siloxane given in figure B.6a and b, respectively.

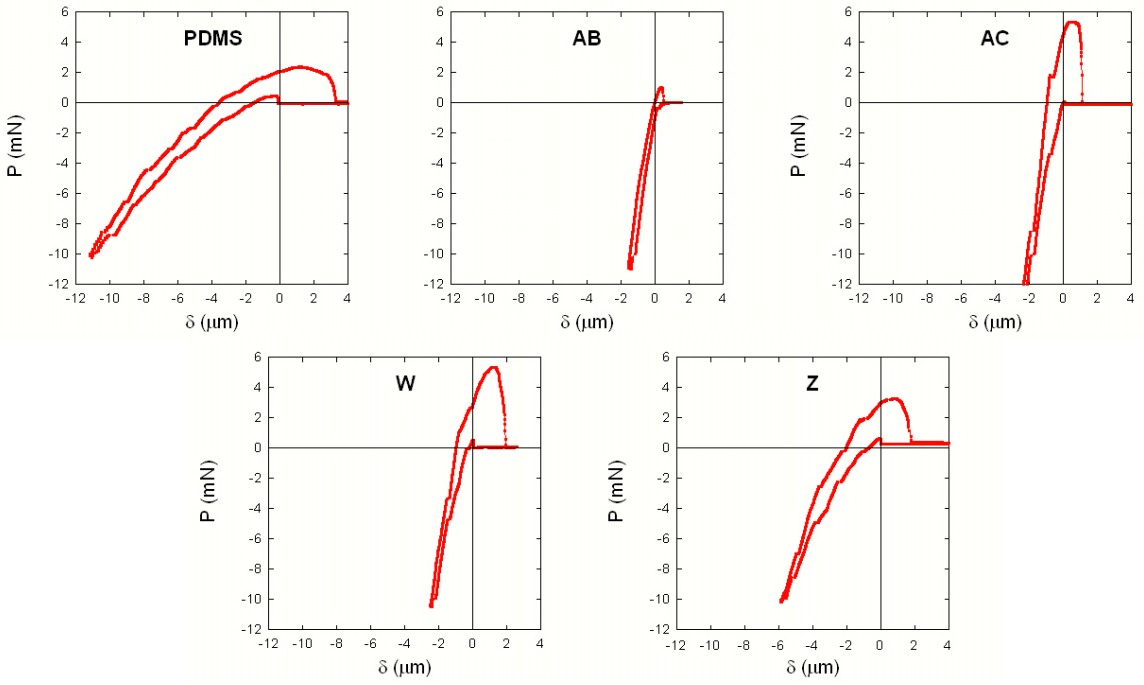

Figure B.3: Force vs Displacement Graphs for Dow-Corning Samples. The force P vs displacement δ graphs for the four Dow-Corning samples AB, AC, W, and Z as well as Sylgard 184^{TM}

B.3 Results & Discussion

B.3.1 Smooth Samples

The modulus, work of adhesion, and energy release rate for each non-patterned surface is given in table B.1, with the moduli values compared in figure B.1. It is clear from these plots that there is not a direct correlation between P_{max} and G_{sep}. While both descriptors for samples W, AB, and Sylgard 184 correspond well with each other, there is a significant discrepancy between P_{max} and G_{sep} for samples AC and Z, which have the lowest energy release rates. Typically, the maximum separation force is used to quantify a materials release properties for imprinting applications. Our results indicate that there is a significant disparity in energy release rate which is

Table B.1: Contact Adhesion of Flat Surfaces. Results from contact adhesion tests on unpatterned surfaces.

Sample	$E(MPa)$	$W_{adh}(Jm^{-2})$	$G_c(Jm^{-2})$
Sylgard 184	2.04	0.076	0.101
AB	40.23	0.164	0.071
AC	33.58	0.436	0.378
W	23.01	0.208	0.227
Z	8.06	0.079	0.140

Monomer	Crosslinker	UV sensitive Initiators	
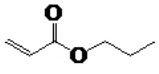	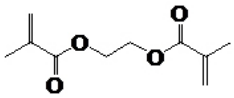	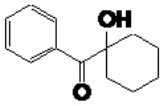	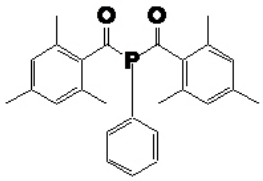
n-butyl acrylate (~75%)	ethylene glycol dimethacrylate (~25%)	Ciba® Irgacure® 184	Ciba® Irgacure® 819

Figure B.4: Imprint Materials. The acrylate formation used for imprint lithography.

not distinguishable by measuring P_{max} alone, and we believe the energy release rate is a better way to quantify a surfaces adhesive, or release, properties.

$$G_{sep} = \frac{3P_{sep}^2}{32\pi E a_{max}^3} \tag{B.1}$$

B.3.2 Tensile Force During Cure

In all the imprint experiments, a tensile force develops immediately upon UV illumination. This tensile stress is attributed to the volume shrinkage of the acrylate film as it photopolymerizes. Our imprinting system is mechanically equivalent to a set of springs connected in series with each of the four components (superstrate, polymer film, template and substrate) having a unique compliance C, which is inversely related

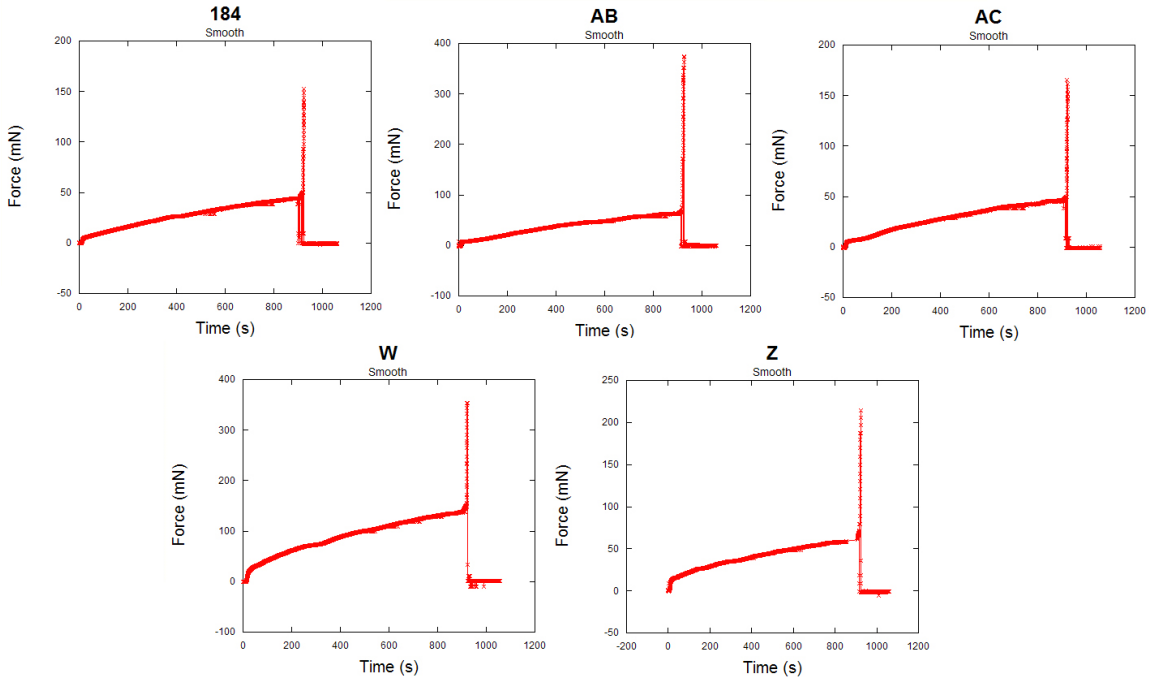

Figure B.5: Smooth Imprint Lithography Results. Force vs time graphs from the smooth imprint lithography experiments for nonpatterned siloxanes.

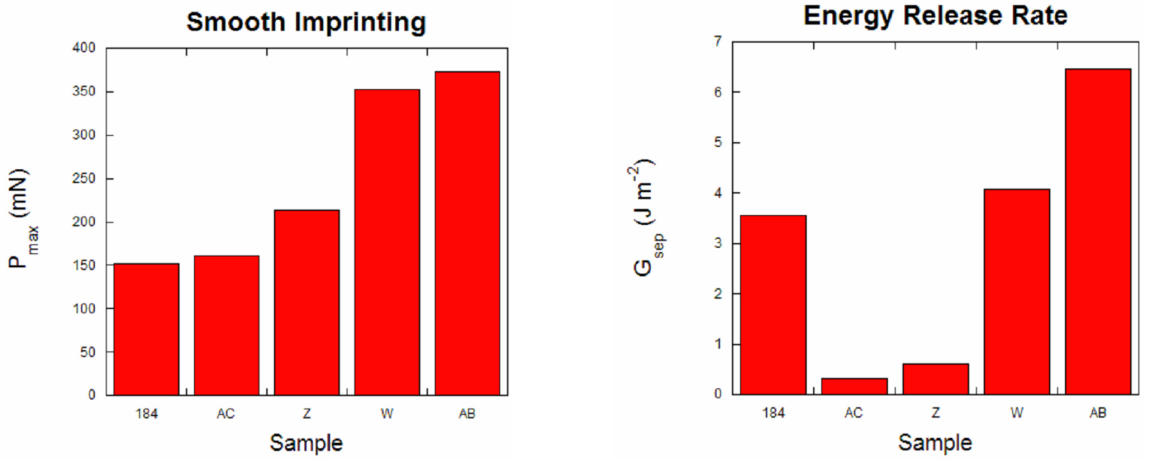

Figure B.6: Smooth Imprint Lithography Results - P_{max} & G_c. a. Maximum separation force of the non-patterned surfaces from figure B.5, b. and the corresponding energy release rates for each material calculated from equation B.1.

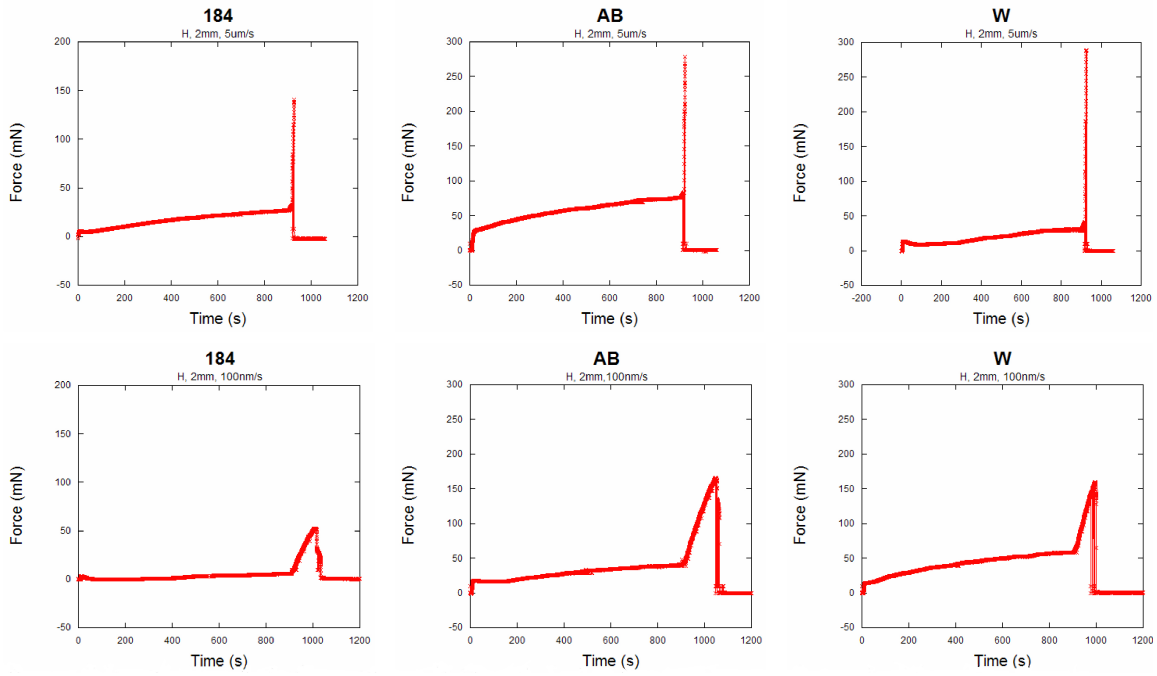

Figure B.7: Tensile Force During Cure. Imprinting data for a pattern with feature diameter and spacing of $10\mu m$ for two velocities: $5\mu m/s$ (Top) and $100nm/s$ (Bottom)

to the materials elastic modulus $\bar{E}$ and the cross-sectional radius a. Upon curing, the monomer solution polymerizes which results in a decrease in volume V_0, and a curing stress develops as a consequence. As the components are connected in series, they all experience the same curing force P_{cure}, but a different degree of deformation. The deformation due to the curing stress δ_{cure} is expressed as the sum total of the deformation experienced by the other three components.

$$\delta_{cure} = \delta_{substrate} + \delta_{template} + \delta_{substrate} \tag{B.2}$$

This deformation is a function of the load that developed during curing and the compliance of the system such that:

$$\delta_{cure} = P_{cure}(C_{superstrate} + C_{template} + C_{substrate}) \tag{B.3}$$

Due to the planar geometry, the volume shrinkage primarily causes a reduction in the original thickness of the polymer film $h_{monomer}$. The value of δ_{cure} is the product of the volumetric strain $\Delta V/V_0$ and $h_{monomer}$.

$$\delta_{cure} = \frac{\Delta V}{V_0} h_{polymer} = \varepsilon_{polymer} h_{polymer} \tag{B.4}$$

Substitution of equation B.3 into equation B.4 and solving for P_{cure} allows us to relate the curing force to the volumetric strain of the polymer film:

$$P_{cure} = \frac{2a(h_{polymer})(\varepsilon_{polymer})}{\frac{1}{\bar{E}_{superstrate}} \frac{1}{\bar{E}_{template}} \frac{1}{\bar{E}_{substrate}}} \tag{B.5}$$

In instances where a soft template is used, the compliance of the template $C_{template}$ is significantly greater than the other components, this simplifies equation B.5 by relating P_{cure} to the 3 adjustable parameters: 1) h_{poly} which is initial thickness of the monomer solution, 2) ε_{poly} which can be controlled through the chemical formulation used (i.e., type of crosslinker) and 3) $\bar{E}_{template}$:

$$P_{cure} \sim a(h_{poly})(\varepsilon_{polymer})(\bar{E}_{template}) \tag{B.6}$$

B.3.3 Patterned Imprinting

Our goal is to link material properties that inherently dictate the adhesion and release of the siloxane-based materials to their performance in the imprinting process by comparing the release properties of the acrylate from the smooth siloxane surface to the patterned siloxane surface. We have designed a mask for photolithography that varies feature size and spacing from $1\mu m$ to $10\mu m$. By using photolithography, we will replicate these features onto each polymer's surface and perform the same imprinting process that we performed on the non-patterned surfaces. Due to pattern

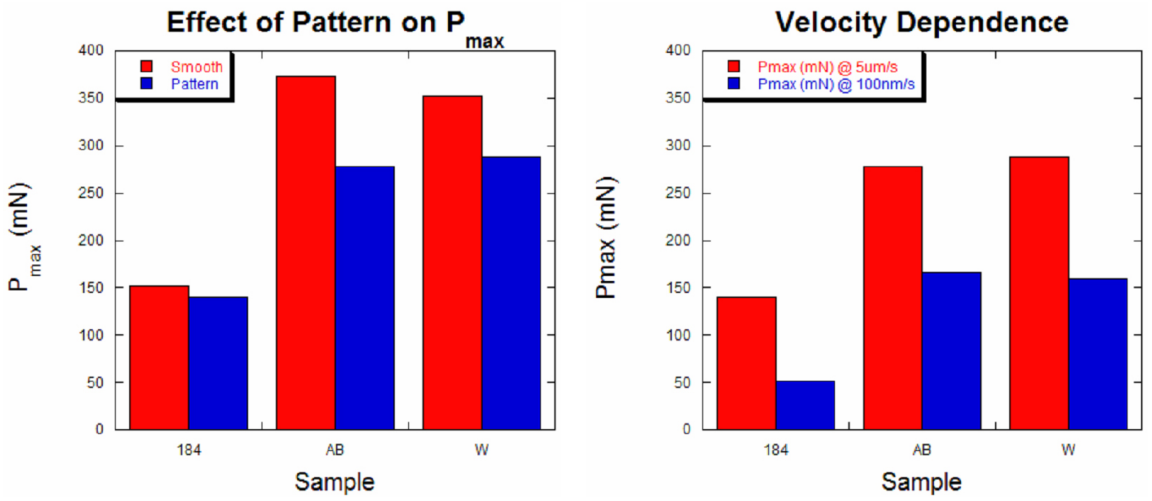

Figure B.8: Effect of Pattern and Velocity on P_{max}. *a*. Effect of a pattern on the maximum separation force P_{max} measured during monomer curing. The results from from the imprinting experiments suggest a small decrease in P_{max} for the patterned samples compared to smooth substrates. *b*. A similar trend in P_{max} is observed when comparing imprint experiments run at velocities of $5\mu m/s$ and $100nm/s$ on patterned substrates.

transfer difficulties, we tested the effect of a pattern with a feature diameter of $10\mu m$ and a feature spacing of $10\mu m$ on samples 184, AB, and W. The force vs. time graphs for these experiments are given in Figure B.7.

To determine the effects of the pattern on the release of the siloxane we first compared the maximum separation forces for the smooth and patterned surfaces (Figure B.8a). There is a slight decrease in maximum force for each patterned siloxane when compared to its smooth P_{max} value. Although there appears to be a correlation between the pattern and a decrease in the maximum separation force, it is not clear that these effects are not simply due to the edge effects that occur as the crack propagates across the interface between the smooth surface and the edge of the pattern. By being able to isolate the monomer droplet to the patterned region, either by a smaller droplet volume or a larger patterned region, we would be able to better determine whether or not this decrease in the maximum separation force is due to the pattern.

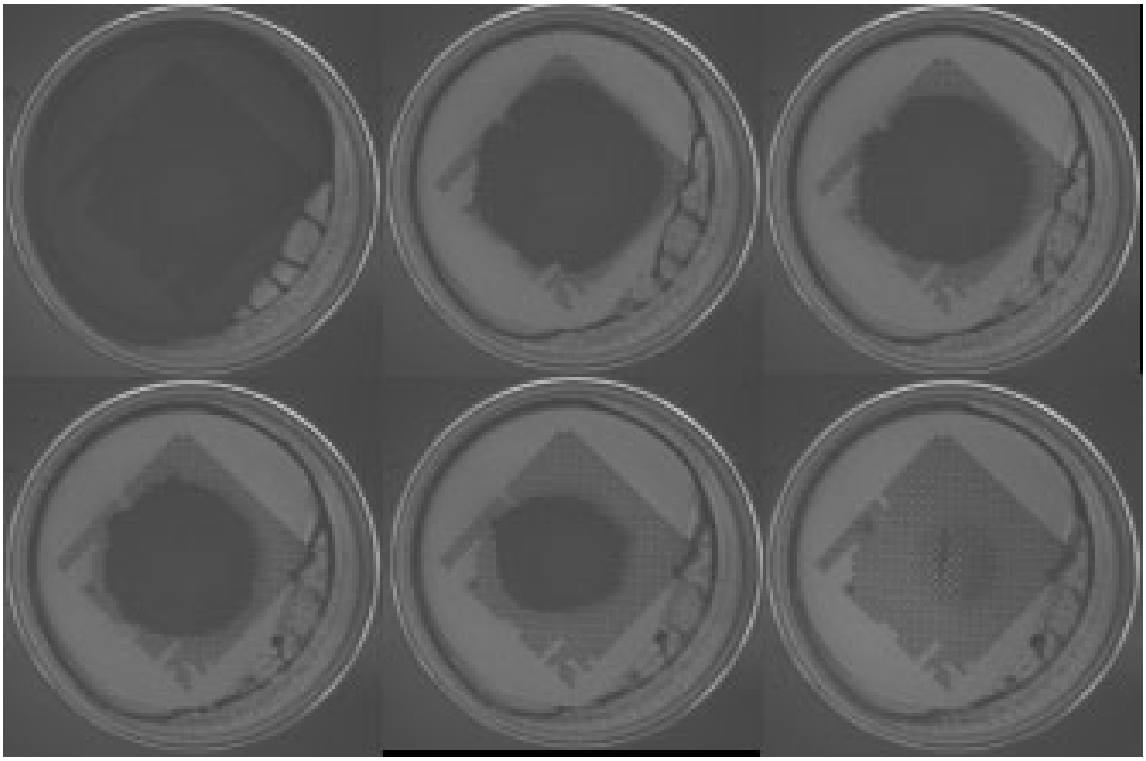

Figure B.9: Images of Imprint Lithography. Following the separation of the cured acrylate from the siloxane surface (from top left to bottom right) allows the observation of crack propagation across the patterned region.

Another way we studied the mechanism of separation of the cured acrylate from the patterned siloxane was by varying the rate of separation. As shown in figure B.8b, there is a clear dependence of the maximum separation force on the separation velocity. By varying this separation velocity we were able to capture the separation as the crack propagated across the patterned region (Figure B.9).

B.4 Summary

Over the course of this study we were able to demonstrate a unique characterization technique for the fundamental study of nanoimprinting release. We illustrated how measuring the maximum separation force alone is not a true indication of the material's release properties for imprinting applications; it is important to quantify the energy release rate for the material. We discussed the effect of the material's

modulus on the tensile stress that builds up during the cure process and how it is important to accurately control the separation distance between the template and the lens in order to prevent a premature separation of the acrylate and the siloxane while the acrylate is only partially cured.

The study of pattern effects revealed that patterns may cause the maximum separation to decrease from that of the non-patterned surface, though further studies in this area would need to be completed to confirm this. It is also important to note the dramatic separation velocity dependence we saw when separating from the patterned siloxane surfaces. Separating the acrylate from the siloxane at velocities as low as 100nm/s allowed us to capture the release as the crack propagated across the patterned surface.

B.5 Acknowledgements

We would like to thank the NSF-REU John Whang for important experimental contributions to this work. The authors also thank the Dow-Corning Corporation for funding for this project. We thank Ciba Specicialty Chemicals for providing the IRGACURE initiators.

BIBLIOGRAPHY

[1] Y. Forterre, J. M. Skotheim, J. Dumais, and L. Mahadevan. How the venus flytrap snaps. *Nature*, 433:421–425, 2005.

[2] J.M. Skotheim and L. Mahadevan. Physical limitations of plant movements. *Science*, 308:1308–1310, 2005.

[3] Alfred J. Crosby, Mark Hageman, and Andrew Duncan. Controlling polymer adhesion with pancakes. *Langmuir*, 99:11738–11743, 2005.

[4] K. Autumn and A.M. Peattie. Mechanisms of adhesion in geckos. *Integrative and Comparative Biology*, 42:1081–1090, 2002.

[5] B. Bhushan, A.G. Peressadko, and T.W. Kim. Adhesion analysis of two-level hierarchical morphology in natural attachment systems for 'smart adhesion'. *Journal of Adhesion Science and Technology*, 20:1475–1491, 2006.

[6] B. Bhushan and R.A. Sayer. No title. *Microsystem Technologies-Micro-and Nanosystems-Information Storage and Processing*, 13:71–78, 2007.

[7] L. Dong, A.K. Agarwal, D.J. Beebe, and H.R. Jiang. Adaptive liquid microlenses activated by stimuli-responsive hydrogels. *Nature*, 442:551–554, 2006.

[8] Armin Werber and Hans Zappe. Tunable microfluidic microlenses. *Applied Optics*, 44:3238–3245, 2005.

[9] K.E. Uhrich, S.M. Cannizzaro, R.S. Langer, and K.M. Shakesheff. Polymeric systems for controlled drug release. *Chemical Reviews*, 99:3181–3198, 1999.

[10] R.S. Langer. Drug delivery and targeting. *Nature*, 393:5–10, 1998.

[11] R.S. Langer. New methods of drug delivery. *Science*, 249:1527–1533, 1990.

[12] A.N. Shipway, E. Katz, and I. Willner. Nanoparticle arrays on surfaces for electronic, optical, and sensor applications. *ChemPhysChem*, 1:18–52, 2000.

[13] J. Kong, N.R. Franklin, C.W. Zhou, M.G. Chapline, S. Peng, K.J. Cho, and H.J. Dai. Nanotube molecular wires as chemical sensors. *Science*, 287:622–625, 2000.

[14] J.H. Holtz and S.A. Asher. Polymerized colloidal crystal hydrogel films as intelligent chemical sensing materials. *Nature*, 389:829–832, 1997.

[15] Z G Wei, R Sandstrom, and S Miyazaki. Shape-memory materials and hybrid composites for smart systems - part i shape-memory materials. *Journal of Materials Science*, 33:3743–3762, 1998.

[16] I Bellin, S Kelch, R Langer, and A Lendlein. Polymeric triple-shape materials. *Proceedings of the National Academy of Sciences of the United States of America*, 103:18043–18047, 2006.

[17] I Luzinov, S Minko, and V V Tsukruk. Adaptive and responsive surfaces through controlled reorganization of interfacial polymer layers. *Progress in Polymer Science*, 29:635–698, 2004.

[18] M M Zhang, L Liu, C L Wu, G Q Fu, H Y Zhao, and B L He. Synthesis, characterization and application of well-defined environmentally responsive polymer brushes on the surface of colloid particles. *Polymer*, 48:1989–1997, 2007.

[19] S.P. Timoshenko and J.M. Gere. *Theory of Elastic Stability*. McGraw-Hill, Inc., New York, 2nd ed. edition, 1961.

[20] D. Shilkrut. *Stability of Nonlinear Shells*. Elsevier, London, 2002.

[21] I.I. Vorovitch and N.I. Minakova. *The problem of stability and numerical methods in the theory of spherical shells*, pages 5–87. VINITI, Moscow, (in russia edition, 1973.

[22] T. A. Witten. Stress focusing in elastic sheets. *Reviews of Modern Physics*, 79:643–675, April 2007.

[23] M. Nelkin. In what sense is turbulence an unsolved problem? *Science*, 255:566–570, 1992.

[24] H. F. Robey, T. S. Perry, R. I. Klein, J. O. Kane, J. a. Greenough, and T. R. Boehly. Experimental investigation of the three-dimensional interaction of a strong shock with a spherical density inhomogeneity. *Physical Review Letters*, 89:1–4, August 2002.

[25] L. De Arcangelis, A. Hansen, H.J. Herrmann, and S. Roux. Scaling laws in fracture. *Physical Review B*, 40:877–880, 1989.

[26] J.P. Gollub and J.S. Langer. Pattern formation in nonequilibrium physics. *Reviews of Modern Physics*, 71:396–403, 1999.

[27] P.M. Reis, F. Corson, A. Boudaoud, and B. Roman. Localization through surface folding in solid foams under compression. *Physical Review Letters*, 103:1–4, July 2009.

[28] J. Bard. *Morphogenesis: The Cellular and Molecular Processes of Developmental Anatomy*. Cambridge University Press, New York, 1990.

[29] J.T. Koberstein. Surface and interface modification of polymers. *MRS Bulletin*, 21:19–23, 1996.

[30] M.A. Biot. General theory of three-dimensional consolidation. *Journal of Applied Physics*, 12:155–164, 1941.

[31] J. M. Skotheim and L. Mahadevan. Dynamics of poroelastic filaments. *Proceedings of the Royal Society A: Mathematical, Physical and Engineering Sciences*, 460:1995–2020, July 2004.

[32] J.E. Mark, editor. *Polymer Data Handbook*. Oxford University Press, Oxford, 1999.

[33] L C Gao and T J McCarthy. The "lotus effect" explained: Two reasons why two length scales of topography are important. *Langmuir*, 22:2966–2967, 2006.

[34] M.K. Chaudhury and M.J. Owen. Adhesion hysteresis and friction. *Langmuir*, 9:29–31, 1993.

[35] P.L. Menezes, Kishore, and S.V. Kailas. Studies on friction and transfer layer: role of surface texture. *Tribology Letters*, 24:265–273, 2006.

[36] R.J. Asaro and J.R. Rice. Strain localization in ductile single-crystals. *Journal of the Mechanics and Physics of Solids*, 25:309–338, 1977.

[37] M. Ortiz and G. Gioia. The morphology and folding patterns of buckling-driven thin-film blisters. *Journal of the Mechanics and Physics of Solids*, 42:531–559, 1994.

[38] Enrique Cerda and Francisco Melo. Conical dislocations in crumpling. *Nature*, 401, 1999.

[39] Enrique Cerda. Mechanics of scars. *Journal of Biomechanics*, 38:1598–1603, August 2005.

[40] M.A. Meyers, A. Mishra, and D.J. Benson. Mechanical properties of nanocrystalline materials. *Progress in Materials Science*, 51:427–556, 2006.

[41] Douglas P. Holmes, Michal Ursiny, and Alfred J. Crosby. Crumpled surface structures. *Soft Matter*, 4:82, 2008.

[42] Douglas P. Holmes and Alfred J. Crosby. Snapping surfaces. *Advanced Materials*, 19:3589–3593, November 2007.

[43] V. Trujillo, J. Kim, and R.C. Hayward. Creasing instability of surface attached hydrogels. *Soft Matter*, 4:564–569, 2008.

[44] L. Pocivavsek, R. Dellsy, A. Kern, S. Johnson, B. Lin, K. Y. C. Lee, and Enrique Cerda. Stress and fold localization in thin elastic membranes. *Science*, 320:912–916, May 2008.

[45] S.P. Timoshenko and J.N. Goodier. *Theory of Elasticity*. McGraw-Hill, Inc., New York, 3rd ed. edition, 1970.

[46] Enrique Cerda and L. Mahadevan. Geometry and physics of wrinkling. *Physical Review Letters*, 90:1–4, February 2003.

[47] Edwin P. Chan and Alfred J. Crosby. Spontaneous formation of stable aligned wrinkling patterns. *Soft Matter*, 2:324, 2006.

[48] J. Huang, M. Juszkiewicz, W. H. De Jeu, Enrique Cerda, T. Emrick, N. Menon, and T. P. Russell. Capillary wrinkling of floating thin polymer films. *Science*, 317:650–653, August 2007.

[49] Eran Sharon and Harry L. Swinney. Geometrically driven wrinkling observed in free plastic sheets and leaves. *Physical Review E*, 75:1–7, April 2007.

[50] Michael Marder, Robert D Deegan, and Eran Sharon. Crumpling, buckling, and cracking: Elasticity of thin sheets. *Physics Today*, pages 33–38, 2007.

[51] Victor Romero, Enrique Cerda, T a Witten, and Tao Liang. Force focusing in confined fibres and sheets. *Journal of Physics D: Applied Physics*, 41:132003, July 2008.

[52] Y. Klein, E. Efrati, and Eran Sharon. Shaping of elastic sheets by prescription of non-euclidean metrics. *Science*, 315:1116–1120, February 2007.

[53] K.O. Friedrichs and J.J. Stoker. Buckling of the circular plate beyond the critical thrust. *Journal of Applied Mechanics*, pages A7–A13, 1942.

[54] A.N. Sherbourne. Elastic, post-buckling behaviour of a simply supported circular plate. *Journal of Mechanical Engineering Science*, 3:133–141, 1961.

[55] P.S. Bulson. *The Stability of Flat Plates*. Chatto and Windus, London, 1970.

[56] L. Landau and E.M. Lifshitz. *Theory of Elasticity*. Pergamon, New York, 3rd ed. edition, 1986.

[57] S.P. Timoshenko and S. Woinowsky-Kreiger. *Theory of Plates and Shells*. McGraw-Hill, Inc., New York, 2nd edition, 1964.

[58] K. Tanizawa and K. Miura. Large displacement configurations of bi-axially compressed infinite plate. *Transactions of the Japan Society for Aeronautical and Space Sciences*, 20:175–187, 1978.

[59] Alex Lobkovsky, Sharon Gentges, Hao Li, David Morse, and T A Witten. Scaling properties of stretching ridges in a crumpled elastic sheet. *Science*, 270:1482–1485, 1995.

[60] R.F. Albuquerque and M.A.F. Gomes. Stress relaxation in crumpled surfaces. *Physica A - Statistical Mechanics and its Applications*, 310:377–383, 2002.

[61] A.E. Lobkovsky. Boundary layer analysis of the ridge singularity in a thin plate. *Physical Review E*, 53:3750–3759, 1996.

[62] D. Nelson. *Statistical Mechanics of Membranes and Surfaces*. World Scientific, Singapore, 1989.

[63] Y.L. Kergosien, H. Gotoda, and T.L. Kunii. Bending and creasing virtual paper. *IEEE Computer Graphics and Applications*, 14:40–48, 1994.

[64] L. Euler. Elastic curves. *Isis*, 20:72–160, 1744.

[65] R J M Smit, W A M Brekelmans, and H E H Meijer. Predictive modelling of the properties and toughness of polymeric materials. *Materials Technology*, 5:2855 – 2867, 2000.

[66] Gloria M. Gusler and Gregory B. McKenna. The craze initiation response of a polystyrene and a styrene-acrylonitrile copolymer during physical aging. *Polymer Engineering and Science*, 37:1442–1448, September 1997.

[67] L.B. Freund and S. Suresh. *Thin Film Materials: Stress, Defect Formation, and Surface Evolution*. Cambridge University Press, Cambridge, 1st edition, 2009.

[68] Wilhelm T S Huck, Ned Bowden, Patrick Onck, Thomas Pardoen, John W Hutchinson, and George M Whitesides. Ordering of spontaneously formed buckles on planar surfaces. *Langmuir*, 16:3497–3501, 2000.

[69] Kirill Efimenko, Mindaugas Rackaitis, Evangelos Manias, Ashkan Vaziri, L. Mahadevan, and Jan Genzer. Nested self-similar wrinkling patterns in skins. *Nature Materials*, 4:293–297, March 2005.

[70] Stephanie Perichon Lacour, Sigurd Wagner, Zhenyu Huang, and Z. Suo. Stretchable gold conductors on elastomeric substrates. *Applied Physics Letters*, 82:2404, 2003.

[71] E.P Chan, E.J. Smith, R.C. Hayward, and A.J. Crosby. Surface wrinkles for smart adhesion. *Advanced Materials*, 20:711–716, 2008.

[72] Enrique Cerda, L Mahadevan, J M Pasini, and Conical Folds. The elements of draping. *Proceedings of the National Academy of Sciences*, 101:1806–1810, 2004.

[73] Kittiwit Matan, Rachel B. Williams, Thomas a. Witten, and Sidney R. Nagel. Crumpling a thin sheet. *Physical Review Letters*, 88:7–10, February 2002.

[74] J-C Géminard, R Bernal, and F Melo. Wrinkle formations in axi-symmetrically stretched membranes. *The European physical journal. E, Soft matter*, 15:117–26, October 2004.

[75] T. Thomas and A.J. Crosby. Controlling adhesion with surface hole patterns. *Journal of Adhesion*, 82:311–329, 2006.

[76] K Lewis and A M Klibanov. Surpassing nature: rational design of sterile-surface materials. *Trends in Biotechnology*, 23:343–348, 2005.

[77] P K Brown and P S Brown. Visual pigments of the octopus and cuttlefish. *Nature*, 182:1288–1290, 1958.

[78] C C Chiao and R T Hanlon. Cuttlefish camouflage: Visual perception of size, contrast and number of white squares on artificial checkerboard substrata initiates disruptive coloration. *Journal of Experimental Biology*, 204:2119–2125, 2001.

[79] J Comandon and P De Fonbrune. Experimental research on predatory fungi of nematodes. the garrotte traps. *Comptes Rendus Des Seances De La Societe De Biologie Et De Ses Filiales*, 129:620–622, 1938.

[80] J Edwards, D Whitaker, S Klionsky, and M J Laskowski. Botany - a record-breaking pollen catapult. *Nature*, 435:164, 2005.

[81] K Otsuka and X B Ren. Recent developments in the research of shape memory alloys. *Intermetallics*, 7:511–528, 1999.

[82] A Lendlein and S Kelch. Shape-memory polymers. *Angewandte Chemie-International Edition*, 41:2034–2057, 2002.

[83] J Kim, S Nayak, and L A Lyon. Bioresponsive hydrogel microlenses. *Journal of the American Chemical Society*, 127:9588–9592, 2005.

[84] B Wang, T He, L L Liu, and C Y Gao. Poly(ethylene glycol) micro-patterns as environmentally sensitive tern plate for selective or non-selective adsorption. *Colloids and Surfaces B-Biointerfaces*, 46:169–174, 2005.

[85] H Y Jiang, S Kelch, and A Lendlein. Polymers move in response to light. *Advanced Materials*, 18:1471–1475, 2006.

[86] Z H Yang, J L Hu, Y Q Liu, and L Y Yeung. The study of crosslinked shape memory polyurethanes. *Materials Chemistry and Physics*, 98:368–372, 2006.

[87] A Sidorenko, T Krupenkin, A Taylor, P Fratzl, and J Aizenberg. Reversible switching of hydrogel-actuated nanostructures into complex micropatterns. *Science*, 315:487–490, 2007.

[88] J N Kizhakkedathu, R Norris-Jones, and D E Brooks. Synthesis of well-defined environmentally responsive polymer brushes by aqueous atrp. *Macromolecules*, 37:734–743, 2004.

[89] H Becker and L E Locascio. Polymer microfluidic devices. *Talanta*, 56:267–287, 2002.

[90] P Rai-Choudhury. *Handbook of Microlithography, Micromachinging, and Microfabrication*, volume 1. SPIE Opt. Engineer. Press, Bellingham, WA, 1997.

[91] J H Kim and S Kumar. Fast switchable and bistable microlens array using ferroelectric liquid crystals. *Japanese Journal of Applied Physics Part 1-Regular Papers Short Notes and Review Papers*, 43:7050–7053, 2004.